

POLITECNICO DI TORINO  
INSTITUT NATIONAL POLYTECHNIQUE DE GRENOBLE  
ÉCOLE POLYTECHNIQUE FÉDÉRALE DE LAUSANNE

---

Master of Science in Nanotechnologies for ICTs

Master Degree Thesis

# Simulation and Modelling of Interconnect Networks for CMOS Quantum Bit Systems



POLITECNICO  
DI TORINO



EPFL

**Supervisor**

Prof. Gianluca PICCININI

**Candidate**

André CHATEL

**Internship Supervisor**

Grenoble CEA-LETI

Dr. Hélène JACQUINOT



---

ACADEMIC YEAR 2019-2020

This thesis is licensed under a Creative Commons License, Attribution – Noncommercial – NoDerivative Works 4.0 International: see [www.creativecommons.org](http://www.creativecommons.org). The text may be reproduced for non-commercial purposes, provided that credit is given to the original author.

*”O frati”, dissi ”che per cento milia  
perigli siete giunti a l’occidente,  
a questa tanto picciola vigilia*

*d’i nostri sensi ch’è del rimanente,  
non vogliate negar l’esperienza,  
di retro al sol, del mondo senza gente.*

*Considerate la vostra semenza:  
fatti non foste a viver come bruti,  
ma per seguir virtute e canoscenza”.*

*Inferno, Canto XXVI*

# Acknowledgements

These last academic years have probably been the most exciting, but also challenging, period of my life. The exchange international master shared between PoliTO, PHELMA and EPFL actually allowed me to get in contact with many different mentalities and to enlarge my human experience, but it demanded me a considerable effort to reach such an important personal accomplishment. Moreover, because of the anomalous and, I hope, unrepeatable conditions in which this master thesis internship took place, concerning the health emergency that originated in the last months as a consequence of Covid-19 global pandemic, this section is dedicated to my most grateful acknowledgements for the people that supported me, in any possible way, during this last period.

First of all, I would like to thank all my beloved family, in particular, my father Roberto, my mother Sandra and my brother Marc, for always having encouraged me all along my academic years. A particular thought also goes to all my Nanotech friends, who shared with me such an incredible experience, supporting each others during the most tough moments of this international master.

On the other hand, a special thanks is certainly dedicated to H el ene Jacquinet, who followed and motivated me during such an extraordinary internship project, even during the difficult smart-working conditions, always showing remarkable professional and human qualities. Another special acknowledgement is reserved to the head of the LSM lab at LETI, Thierry Poiroux, who welcomed me in the group and provided me working conditions as good as possible concerning lock-down period and return in the lab.

I am very grateful also to Yannis Braux, from 3D Dassault Syst emes, for having helped me a lot with the use of CST software during my smart-working condition. A special thanks goes also to our IRIG colleagues Silvano De Franceschi, Xavier Jehl and Romain Maurand, for having been available to explain me the functioning of hardware silicon-based Quantum Computing. Moreover, I would thank also our colleagues from Grenoble CNRS, David Niegemann and Matias Urdampilleta, for having realized the design of the Nb superconducting inductor and having given me precious advices on the spin readout mechanisms. Last but not least, a special acknowledgement is reserved to all my lab colleagues and, especially, the LSM PhD students, Mohamed Aouad, Bledion Rustemi, Sung-Ho Lee, R emi Defrance and Ousmane Kane: thank you all for having welcomed in the group and shared with me some very joyful life moments.

# Work Environment

Quantum Silicon Grenoble is a dynamic research group located in the French city of Grenoble. The team takes benefit of a long-standing collaboration between Commissariat à l'Énergie Atomique and Centre National de la Recherche Scientifique, aiming at developing a scalable quantum processor, relying on current industrial silicon ICTs manufacturing. In this perspective, such a collaboration project is a unique European environment for spin CMOS Quantum Computing, strengthened by the fundamental and experimental physics expertise on quantum electronics from CNRS Institut Néel and CEA-IRIG (Institut de Recherche Interdisciplinaire de Grenoble), as well as the global-leading micro and nanoelectronics applied research from CEA-LETI (Laboratoire d'Électronique et de Technologie de l'Information).



<https://www.quantumsilicon-grenoble.eu>

In the framework of such a multidisciplinary collaboration project, this master thesis internship has been carried out at CEA-LETI, more precisely, at the Laboratoire de Simulation et Modélisation (LSM). In particular, since its first founding in 1967, LETI's pioneering research in micro and nanotechnologies has led to different technological innovations directly translated in state-of-the-art industrial standards, such as the development of SOI technology by SOITEC's Smart Cut<sup>TM</sup>. The goal of LETI is, therefore, to develop market-oriented revolutionary solutions for the development of information and communication technologies,

relying on an exotic ecosystem made up of long-term industrial partnerships. The major role of CEA-LETI in the Quantum Silicon Grenoble collaboration is the implementation and integration of spin Qubits by standard silicon manufacturing technologies, taking advantage of a fully equipped state-of-the-art industrial cleanroom with 200mm and 300mm platforms. In this perspective, the devices are simulated, fabricated and characterized, relying on the micro and nanoelectronics engineering expertise of such an industrial-driven environment.

# Summary

Because of its disruptive potential and the revolutionary innovations it could bring to the ICTs sector, nowadays Quantum Computing is being intensively investigated in all its possible and feasible implementations. In particular, silicon-based Quantum Computing solutions are more and more attracting the interest of industrial and scientific communities; thanks to well-established microelectronic technologies for Very Large Scale Integration (VLSI), Si-QC is believed to offer incomparable opportunities to increase the number of computational quantum bits, in order to rapidly achieve hardware systems that could naturally implement complex quantum algorithms. However, in this perspective, due to the exotic characteristics of such a research field, a reliable model of interconnect networks is necessary, in order to evaluate the performances of a quantum system in terms of Qubits control and readout.

This project aims, therefore, at providing a study of single metal layer interconnections for the realization of control and readout structures in silicon technologies. In particular, different Radio-Frequencies (RF) networks will be discussed and analysed, by means of dedicated simulation software (*i.e.* ANSYS<sup>®</sup> HFSS<sup>®</sup> and CST Studio Suite<sup>®</sup>), suggesting design opportunities for the efficient control and readout of microwave signals. In order to sum up the content of this work, Chapter 1 will first focus on a brief description of QC working principles and, then, it will present the main state-of-the-art for the current implementation of the most promising quantum systems. Chapter 2 will then consider the study case for On-Chip transmission lines and, notably, the simulation of Coplanar Waveguides (CPW), aiming at extracting the electromagnetic distributed parameters of such a structure. Later on, in Chapter 3 it will be reported the design and simulation of a control line enabling the coherent manipulation of Si Quantum Dots (QDs), focusing on an Electron Spin Resonance (ESR) nano-antenna able to provide a maximum magnetic field and a minimized electric field at spin Qubits location. On the other hand, Chapter 4 will discuss about the simulation of a superconducting inductor, necessary for providing a high-fidelity one-shot tool for the readout of Qubits state, assessing the validity of different RF superconductivity models and extracting the main lumped parameters of such an integrated component. In the end, a brief review of the main results will be reported in Chapter 5, dealing with the achievement of the aforementioned goals, and some guidelines for future researches in these topics will be envisaged.

# Contents

<b>List of Figures</b>	<b>x</b>
<b>List of Tables</b>	<b>xii</b>
<b>1 General Introduction</b>	<b>1</b>
1.1 Preliminary Concepts of Quantum Computing . . . . .	3
1.1.1 Physical Fundamentals . . . . .	4
1.1.2 Quantum and Classical Bits . . . . .	5
1.2 State of the Art for Many-Qubits Systems . . . . .	8
1.2.1 DiVincenzo’s Criteria . . . . .	9
1.2.2 Physical Implementations of Quantum Bits . . . . .	10
1.2.3 CMOS-Compatible Silicon Spin Qubits . . . . .	12
1.3 Objectives . . . . .	14
<b>2 Coplanar Waveguides Technology For On-Chip RF Routing</b>	<b>17</b>
2.1 Introduction . . . . .	17
2.2 Transmission Lines Theory . . . . .	18
2.2.1 Telegrapher’s Equations . . . . .	18
2.2.2 Scattering Matrix Description for 1 and 2-Ports Devices . . . . .	20
2.3 Simulation of Coplanar Waveguides . . . . .	21
2.3.1 Simulation Setup . . . . .	22
2.3.2 Simulation Results of an Al On-Si CPW . . . . .	26
2.3.3 Simulation Results of an Al On-Insulators CPW . . . . .	28
2.4 Conclusion . . . . .	32
2.4.1 Achievements . . . . .	33
2.4.2 Future Work . . . . .	33
<b>3 Electron-Spin Resonance for Coherent Si Spin Qubits Manipulation</b>	<b>35</b>
3.1 Introduction . . . . .	35
3.2 Spin Control by ESR Techniques . . . . .	36
3.2.1 Quantum Mechanics Background . . . . .	36
3.2.2 Spin Qubits Manipulation: Practical Implementations . . . . .	39

3.3	Simulation of a CPW Broadband ESR Line . . . . .	42
3.3.1	Physical Specifications . . . . .	42
3.3.2	CPW-based ESR Line Geometry . . . . .	43
3.3.3	Simulation Results of an Al CPW On-Si ESR Line . . . . .	45
3.3.4	Optimization Results of an Al On-Si ESR Line . . . . .	49
3.3.5	Simulation Results for an Al On-Insulators ESR Line . . . . .	54
3.4	Conclusion . . . . .	59
3.4.1	Achievements . . . . .	60
3.4.2	Future Work . . . . .	60
<b>4</b>	<b>Planar Superconducting Inductor for Spin Qubits Readout</b>	<b>61</b>
4.1	Introduction . . . . .	61
4.2	Electron Spin State Readout . . . . .	62
4.2.1	SET Current Disruptive Readout . . . . .	62
4.2.2	Gate Reflectometry Dispersive Readout . . . . .	66
4.2.3	Superconductivity Models for HF Components Design . . . . .	68
4.3	Electromagnetic Simulation of a Planar Superconducting Inductor . . . . .	71
4.3.1	Planar Inductor Design . . . . .	71
4.3.2	Simulation Results of a 2-Turns Benchmark Inductor . . . . .	75
4.3.3	Simulation Results of the 30-Turns Final Version Inductor . . . . .	80
4.4	Conclusion . . . . .	84
4.4.1	Achievements . . . . .	84
4.4.2	Future Work . . . . .	85
<b>5</b>	<b>General Conclusion</b>	<b>87</b>
5.1	Achievements . . . . .	87
5.2	Future Perspectives . . . . .	88
	<b>Appendices</b>	<b>XIII</b>
<b>A</b>	<b>Transmission Coplanar Waveguide Simulation</b>	<b>xv</b>
A.1	Port Sizing for Line Impedance Convergence . . . . .	xv
A.2	Quasi-TEM Field Distribution at CPW Port . . . . .	xvi
A.3	Conversion Relations for $S$ , $ABCD$ and $Z$ Matrices . . . . .	xvii
A.4	Linking Expressions Between $ABCD$ and Line Parameters . . . . .	xviii
<b>B</b>	<b>ESR Control Line Simulation</b>	<b>xxi</b>
B.1	Derivation of the Rabi Spin Precession Frequency . . . . .	xxi
B.2	Simulation Setup . . . . .	xxiii
B.2.1	Meshing Techniques and Aluminum Thick-Sheet Definition . . . . .	xxiii
B.2.2	Waveguide Port and Boundary Conditions . . . . .	xxiv
B.3	Wave Port Dimensions . . . . .	xxv
B.3.1	$Z_{port}$ Convergence for $W_{port}$ . . . . .	xxv



B.3.2	$Z_{port}$ Convergence for $H_{port}$ . . . . .	xxvi
<b>C</b>	<b>Readout Superconducting Inductor Simulation</b>	<b>xxix</b>
C.1	Planar Inductor Simulation Setup . . . . .	xxix
C.1.1	Mesh Generation . . . . .	xxix
C.1.2	Signal Excitation and Boundaries . . . . .	xxx
C.2	Lumped Port Dimensions . . . . .	xxxi
	<b>Bibliography</b>	<b>xxxiii</b>

# List of Figures

1.1	Expected future applications for QC and estimated value . . . . .	3
1.2	Graphical representation of a quantum bit . . . . .	6
1.3	Qualitative comparison between different QC technologies . . . . .	10
1.4	Representation of a CMOS based silicon spin Qubit . . . . .	12
1.5	3D interconnections array for CMOS quantum computing . . . . .	14
2.1	Distributed-circuit model of a microstrip line . . . . .	18
2.2	Differential lumped model of the transmission line . . . . .	19
2.3	Representation for the derivation of $S$ -matrix . . . . .	20
2.4	Different coplanar transmission lines cross-sections . . . . .	22
2.5	Cross-section and top view of the Al On-Si CPW . . . . .	23
2.6	3D CPW simulated in Ansys <sup>®</sup> HFSS <sup>®</sup> . . . . .	24
2.7	Excitation ports and boundaries for the simulated CPW line . . . . .	25
2.8	$w_g$ optimization for $52 \Omega$ impedance matching . . . . .	26
2.9	$S$ -parameters for the Al On-Si CPW line . . . . .	27
2.10	Real and imaginary parts of the CPW line impedance $Z_C$ . . . . .	28
2.11	Cross-section showing the Al On-Insulators CPW structure . . . . .	29
2.12	$S$ -parameters for the Al On-Insulators CPW . . . . .	29
2.13	Characteristic impedance for the Al On-Insulators CPW . . . . .	30
2.14	CPW distributed $RLC$ parameters . . . . .	31
3.1	Graphical description of ESR spin manipulation mechanisms . . . . .	39
3.2	SEM picture of spin control shorted ESR line . . . . .	41
3.3	Geometry of the simulated CPW-based ESR control line . . . . .	44
3.4	Zoomed top view of the ESR nano-antenna . . . . .	45
3.5	ESR line Quasi-TEM electric field port cross-section . . . . .	46
3.6	ESR line port information over the simulated frequency range . . . . .	47
3.7	2D top view of $E$ and $B$ -fields over the ESR line . . . . .	48
3.8	$B$ and $E$ -fields all along the frequency range for each probe . . . . .	49
3.9	Influence of the transmission line length on power dissipation . . . . .	50
3.10	Zoom on the shorted microwave antenna for field optimization . . . . .	51
3.11	Sweep analysis on $l$ , for $B$ and $E$ -fields . . . . .	52
3.12	Sweep analysis on $L_1$ , for $B$ and $E$ -fields . . . . .	52
3.13	Sweep analysis on $L_2$ , for $B$ and $E$ -fields . . . . .	53

3.14	Sweep analysis on $r$ , for $B$ and $E$ -fields . . . . .	53
3.15	Geometry of the optimized Al On-Insulators structure . . . . .	54
3.16	$S$ -parameter of the optimized Al On-Insulators structure . . . . .	55
3.17	Field distributions at the optimized Al On-Insulators nano-antenna . . . . .	56
3.18	Electric and magnetic fields running parallel to the short line . . . . .	57
3.19	Simplified $RLC$ model of the ESR line . . . . .	57
3.20	$RLC$ parameters for the optimized Al On-Insulators ESR line . . . . .	58
4.1	Graphical representation of a CMOS silicon spin Qubit . . . . .	63
4.2	Two spins QDs energy levels with respect to detuning . . . . .	64
4.3	Schematic description of possible SET current dynamics . . . . .	65
4.4	Inter-dots $C_Q$ dependence on the energy levels bending . . . . .	67
4.5	Schematic showing CMOS spin Qubits control and readout circuits . . . . .	67
4.6	planar superconducting Nb spiral inductor geometry . . . . .	72
4.7	Proposed equivalent lumped model of a superconducting inductor . . . . .	75
4.8	2-turns benchmark Nb inductor . . . . .	75
4.9	2D top view of the propagating fields of the 2-turns Nb inductor . . . . .	76
4.10	2-turns inductor 1D fields for the 4 material models . . . . .	77
4.11	Lumped series inductance and resistance of the 2-turns Nb inductor . . . . .	78
4.12	Quality factor of the 2-turns Nb inductor . . . . .	79
4.13	30-turns final Nb inductor . . . . .	80
4.14	2D field views for the 30-turns Nb inductor . . . . .	81
4.15	Lumped series inductance and resistance of the 30-turns Nb inductor . . . . .	82
4.16	Quality factor of the 30-turns Nb inductor . . . . .	83
A.1	Wave port dimensions on 3D CPW structure . . . . .	xv
A.2	Waveport dimensions optimization . . . . .	xvi
A.3	$E$ and $H$ fields at the excitation port . . . . .	xvii
B.1	Mesh generation for the whole ESR structure . . . . .	xxiv
B.2	3D view of the ESR line, comprising waveguide port and boundaries . . . . .	xxv
B.3	3D view of the ESR line, showing the port sweep dimensions . . . . .	xxvi
B.4	Sweep analysis for calculating optimal port dimensions . . . . .	xxvi
C.1	HFSS <sup>®</sup> 3D view of the planar Nb superconducting inductor . . . . .	xxix
C.2	HFSS <sup>®</sup> 3D view, showing excitation and boundaries . . . . .	xxx
C.3	Zoom on the lumped port excitation for the 2-turns inductor . . . . .	xxxix
C.4	Convergence criteria on $h_L$ sweep for inductor $Q$ . . . . .	xxxix

# List of Tables

2.1	Geometrical dimensions for the Al On-Si CPW . . . . .	24
3.1	Field specifications for the design of an On-SI ESR antenna . . . . .	43
3.2	Geometrical dimensions for the overall CPW-based ESR line . . . . .	45
3.3	Geometrical dimensions for the ESR nano-antenna . . . . .	46
3.4	Maximum $B$ -field VS antenna width $r$ . . . . .	53
3.5	Optimized geometrical dimensions for the Al On-Insulators ESR line .	55
3.6	$RLC$ parameters values of the ESR line . . . . .	59
4.1	Geometrical dimensions for the Nb planar inductor . . . . .	73
4.2	Superconductivity parameters for two-fluids and $Z_S$ models . . . . .	74
4.3	$L_S$ , $R_S$ and $Q$ of the 30-turns inductor at 100 $MHz$ . . . . .	83
4.4	Inductor parameters at 100 $MHz$ for the $Z_S$ model . . . . .	84

# Chapter 1

## General Introduction

The "short twentieth century", as it was named by the British historian Eric J. E. Hobsbawm in [1], has been certainly one of the most upsetting periods in the history of mankind: without even considering the social and political events that took place in those years, the last century also distinguished itself for an extraordinary amount of scientific discoveries, which contributed to ferry humanity to the contemporary age. Only to mention some of them, in 1905 and 1915, a young Albert Einstein presented, respectively, its theories of Special and General Relativity, opening the doors to modern astrophysics; around 1926, the Copenhagen interpretation of Quantum Mechanics first unified the various pillars describing this new revolutionary theory for nanoscale physics, while in 1928, a Scottish scientist, named Alexander Fleming, discovered penicillin, reporting the first example of antibiotic in modern medicine.

However, no discovery had such a technological, economical and social impact as the one of the transistor effect, which led to the invention of the first working transistor device in 1947 by John Bardeen, Walter H. Brattain, and William B. Shockley.<sup>1</sup> Such a scientific milestone, physically and electrically implementing the model of a boolean switch, paved the way to the modern information age, allowing human kind to exploit powerful, fast and highly integrated electronic systems for solving computational problems. Moreover, in the last 70 years, mainly after the invention of the first Metal-Oxide-Semiconductor field effect transistor (MOSFET) and integrated circuit, respectively in 1956 and 1958, the high scalability properties of this technology have been largely exploited for increasing the density of On-Chip devices for higher and higher performance circuits. In this sense, the well-known Moore's law (see [2]), dating 1965, has been able to predict a reliable empirical evolution for the increasing computational power over many decades.

Unfortunately, during these last years, such a scaling trend, that has been able to push the limits of integration up to several billions of transistors per single chip, seems to have

---

<sup>1</sup>Even if Shockley was not directly involved in the definitive patent of the point-contact germanium transistor, he should be adequately mentioned for his important contribution to the realization of the first pnp Bipolar-Junction Transistor (BJT) the following year, in 1948.

attained its sunset. As a matter of fact, with atomic dimensions approaching, current technologies are becoming more and more challenging to be developed under  $7\text{ nm}$  nodes and quantum mechanics properties are gradually emerging in the behaviour of these devices. In the future, it is foreseen that the run for improving electronic performances could probably adopt new computational paradigms, following a new More-Than-Moore roadmap. In this dynamic perspective, nowadays, Quantum Computing (QC) is gradually emerging for becoming a valid and much more powerful alternative to classical approaches.

### Quantum Computing through the Years

The first proposal for the implementation of a quantum computer came in 1982, by the American physicist Richard Feynman (see [3]), who foresaw the possibility to project a device able to work with the theoretical principles of quantum mechanics. In so doing, such a machine would have been absolutely effective for simulation tasks, in particular, for dealing with complex quantum systems. Such an idea immediately caught the attention of scientific community, which started to wonder about the way in which this new paradigm could have been harnessed for exploiting its peculiar properties. So, some years later, in 1985, David Deutsch first theorized the model of a universal quantum machine able to satisfy Church-Turing principles for the implementation of computational tasks: his seminar works [4] became a milestone for the following development of quantum information theory.

In the following decades, many scientists started to consider the potentialities of Quantum Computing over Classical Computing and, in so doing, many algorithms were developed, exploiting the innovative properties of such a new approach. As a matter of fact, by means of the natural parallelism quantum mechanics possesses, many "classically intractable" problems have been solved in the QC model: among these, in 1997, Peter Shor developed a well-known algorithm for prime factorization, as reported in [5], showing that this famous classical problem could have been solved in a polynomial time, if exploiting a quantum computer. After the proposal of many other solutions to computational problems, it became clear that an important effort would have been spent during the next years to find the way to physically realize such a machine. In these conditions, David DiVincenzo finally developed a set of 5 rules, synthesised in [6], indicating the necessary specifications for a hardware quantum system to respect in order to be a successful candidate for the implementation of a quantum computer.

Nowadays, in the so-called Noisy Intermediate-Scale Quantum (NISQ) era, many different architectures have been proposed and are currently under investigation by major international companies, like IBM, Google, Microsoft, Intel and many others: such a research field is attracting more and more competitors and, in the next years, it is predicted an extraordinary increase in the generated social and economical impact (see Figure 1.1). Even if many complex challenges still need to be addressed for realising an

effectively working quantum computer,<sup>2</sup> there is currently an exciting race for getting to this new 21<sup>st</sup> century "man-on-the-moon" task, whose achievement could probably lead to a second new revolution, similar to the one related to the invention of the first transistor.

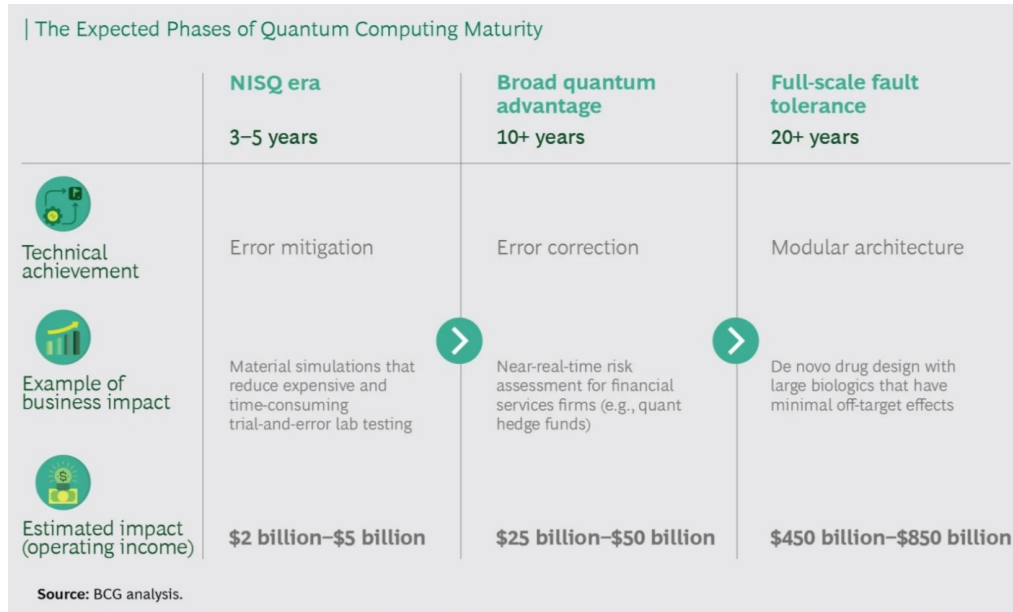


Figure 1.1: Expected future applications for QC and estimated value [8]

## 1.1 Preliminary Concepts of Quantum Computing

Before proceeding with the core of this work, it is appropriate to spend some words about the main principles that make QC such an innovative and powerful computational approach. A quantum computer can be, actually, seen as a classical Turing machine, able to read some input data, perform different intermediate operations on them and, finally, generate new information as output data: in this perspective, a quantum computer absolutely represents the same concept as a normal calculator.

However, the main and most important difference resides in the fact that a quantum computer exploits the exotic laws of quantum mechanics for performing its calculation, differently from a traditional one, relying on the laws of classical physics. This particular aspect is the key factor making QC such a powerful computational tool, but it is also the origin of the many challenges to overcome for realizing an effective and functional machine.

<sup>2</sup>For more information about the current opportunities and challenges QC is facing (in particular for silicon spin-based quantum systems), the reader is invited to refer to [7].

### 1.1.1 Physical Fundamentals

The world of quantum mechanics is a fascinating and still largely unexplored frontier of modern physics: during the last century, it has been able to correctly explain and well predict phenomena that were far beyond the understanding of classical physics (*i.e.* photoelectric effect, atomic theory, superconductivity and so far and so on).

Even if such a physical theory is based on a considerable amount of principles and theorems, whose interpretation is sometimes hard even for the most brilliant physicist,<sup>3</sup> quantum information basically stands only on 3 fundamental principles.

#### Superposition Principle

If a physical system can be described by the wavefunctions  $\psi_1, \psi_2, \psi_3, \dots, \psi_n$ , then, it can also be described by any linear combination  $\Psi = \sum_{i=1}^n c_i \psi_i$  satisfying the normalization relation

$$\sum_{i=1}^n |c_i|^2 = 1$$

In particular, such a principle basically argues that a quantum system can be simultaneously described by a superposition of all its possible states, each one having probability  $|c_i|^2$  to describe the whole system. In this perspective, the normalization relation is necessary to guarantee the existence of the system over the space of possibilities.

#### Wavefunction Collapse Principle

Considering a physical system described by the wavefunction  $\Psi = \sum_{i=1}^n c_i \psi_i$ , when any of its physical observables  $M$  is measured, with the resulting  $m_j$  quantity, then, the system collapses in the  $\psi_j$  state, corresponding to the obtained  $j$ -eigenvalue. A quantum system can be, therefore, described by a superposition state only when not perturbed by any measurement, which has the effect to make it decaying in a single state among the whole possibilities.

#### Entanglement Principle

Having a physical system made up of several different sub-systems, the quantum states describing the single sub-systems are said to be *entangled* when the whole state of the main system cannot be factorized in the tensor product of these latter. Such a principle will be discussed in a more accurate way in §1.1.2: for the moment, the reader should simply understand that two states are entangled when the measurement of one of them gives instantaneously a precise information also on the state of the other one.

---

<sup>3</sup>One should simply consider that Richard Feynman himself, during a series of lectures hold in 1964 at Cornell University, precisely stated: *"If you think you understand quantum mechanics, you don't understand quantum mechanics"*.



### 1.1.2 Quantum and Classical Bits

As it has been already mentioned, the fundamental computational unit defined in quantum information is the so called Quantum Bit, or, simply, Qubit. A Qubit basically describes a quantum physical system that is characterized by two well-energetically-distinguishable levels, namely,  $|0\rangle$  and  $|1\rangle$ . However, differently from the traditional 0-off and 1-on states, a general Qubit  $|\psi\rangle$  can also occupy any superposition state between the previous orthonormal states, in the form of

$$|\psi\rangle = \alpha |0\rangle + \beta |1\rangle = \alpha \begin{pmatrix} 1 \\ 0 \end{pmatrix} + \beta \begin{pmatrix} 0 \\ 1 \end{pmatrix} = \begin{pmatrix} \alpha \\ \beta \end{pmatrix} \quad (1.1.2.1)$$

where the complex coefficients  $\alpha$  and  $\beta$  must satisfy the orthonormal relation  $|\alpha|^2 + |\beta|^2 = 1$ , for the existence of the state. Moreover, such coefficients express, in modulus-square, the probability to find the Qubit, once measured, in the ground or in the excited state. In particular, in Equation 1.1.2.1, it has been used the Dirac notation for the definition of the Qubit as a unitary vector in the complex space  $\mathbb{C}^2$ : such a notation, as explained in [9], is a powerful tool for the description of quantum bits, defining each possible Qubit in terms of the standard computational basis vectors:

$$|0\rangle = \begin{pmatrix} 1 \\ 0 \end{pmatrix} \quad |1\rangle = \begin{pmatrix} 0 \\ 1 \end{pmatrix}$$

#### Bloch Sphere Representation

Geometrically, the state of a Qubit can be easily associated to a point over the surface of a unitary-radius sphere, whose North-pole corresponds to the  $|0\rangle$  state and the South-pole corresponds to the  $|1\rangle$  state: such a sphere is called Bloch sphere and provides an intuitive visualization of the state of quantum bits.

As a matter of fact, having a general Qubit  $|\psi\rangle = \alpha |0\rangle + \beta |1\rangle$ , it is possible to rewrite its complex coefficients by means of Euler's formula, being  $j$  the imaginary unit:

$$|\psi\rangle = \alpha |0\rangle + \beta |1\rangle = r_0 e^{j\phi_0} |0\rangle + r_1 e^{j\phi_1} |1\rangle \quad (1.1.2.2)$$

where  $|\alpha|^2 + |\beta|^2 = r_0^2 + r_1^2 = 1$ . Such last expression allows to express radii in terms of trigonometric relations, as  $r_0 = \cos(\vartheta/2)$  and  $r_1 = \sin(\vartheta/2)$  for  $0 \leq \vartheta \leq \pi$ .

Introducing, now, the so-called relative-phase term  $\varphi = \phi_1 - \phi_0$ , for  $0 \leq \phi \leq 2\pi$ , it is possible to rewrite Equation 1.1.2.2 as:

$$|\psi\rangle = r_0 e^{j\phi_0} |0\rangle + r_1 e^{j\phi_1} |1\rangle = \cos(\vartheta/2) |0\rangle + e^{j\varphi} \sin(\vartheta/2) |1\rangle$$

where a common term  $e^{j\phi_0}$ , called global-phase, has been eliminated, being physically irrelevant for distinguishing the two basis states (see [9]).

In this perspective, the reader should now have understood that, differently from classical bits, a quantum bit is expressed as a *continuum* of states, built up in terms of

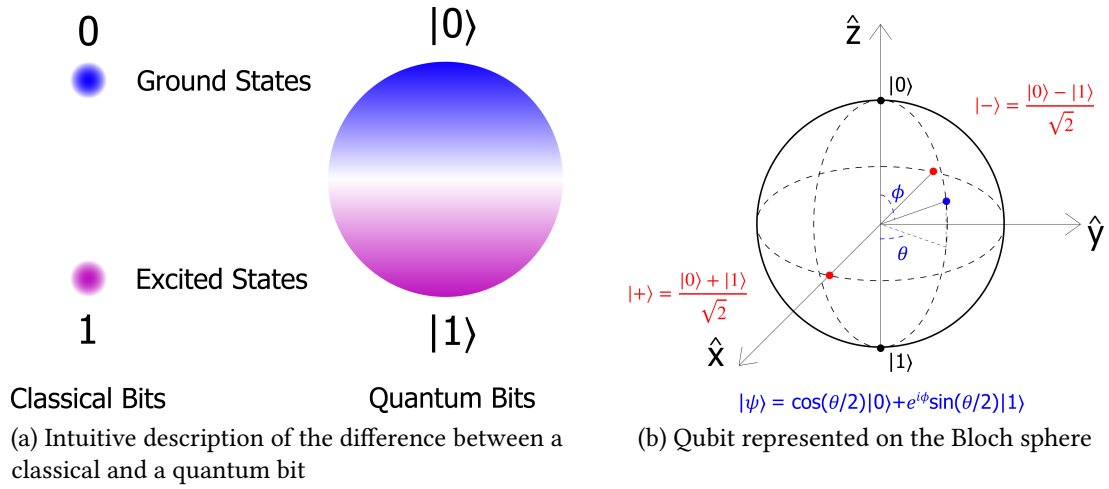


Figure 1.2: Graphical representation of a quantum bit

the computational basis.<sup>4</sup> In particular, Figure 1.2(a) presents an intuitive description of such a difference, while in Figure 1.2(b) is reported the graphical representation of a Qubit on the Bloch sphere.

### Many Qubits: Registers and Entanglement

It is also possible to extend the previous discussion to  $n$  different Qubits by recurring to the concept of *register*. To make things simpler, in the previous section, it has been shown that, differently from a classical bit, a quantum bit can exist in 2 different quantum states, namely  $|0\rangle$  and  $|1\rangle$ . If considering a system composed of 2 Qubits, its state can be described in terms of 4 different states, precisely  $|0\rangle|0\rangle$ ,  $|0\rangle|1\rangle$ ,  $|1\rangle|0\rangle$  and  $|1\rangle|1\rangle$ ; such a superposition depends on the state of each one of the 2 Qubits and, in Dirac notation, it originates the following general 2-Qubits system, called register:

$$|\psi\rangle = \alpha|00\rangle + \beta|01\rangle + \gamma|10\rangle + \delta|11\rangle = \alpha \begin{pmatrix} 1 \\ 0 \\ 0 \\ 0 \end{pmatrix} + \beta \begin{pmatrix} 0 \\ 1 \\ 0 \\ 0 \end{pmatrix} + \gamma \begin{pmatrix} 0 \\ 0 \\ 1 \\ 0 \end{pmatrix} + \delta \begin{pmatrix} 0 \\ 0 \\ 0 \\ 1 \end{pmatrix} = \begin{pmatrix} \alpha \\ \beta \\ \gamma \\ \delta \end{pmatrix}$$

where  $|\alpha|^2 + |\beta|^2 + |\gamma|^2 + |\delta|^2 = 1$ , with  $|00\rangle$ ,  $|01\rangle$ ,  $|10\rangle$  and  $|11\rangle$  defining the  $\mathbb{C}^{2^2}$  standard computational basis.

<sup>4</sup>For the reader having some knowledge of Latin language, the difference between classical and quantum bits is similar to the one subsisting between the two conjunctions *aut* and *vel*. This means that a classical bit can be *aut* 0 *aut* 1, with no other possibility, while a Qubit can be  $|0\rangle$  *vel*  $|1\rangle$ , with the possible out-of-measure case to be both at the same time.

It is possible to demonstrate, as reported in [9], that such a description can be generalized to the case of  $n$  Qubits, resulting in a register defined by  $2^n$  basis states in  $\mathbb{C}^{2^n}$ : it means that a collection of  $n$  Qubits, *i.e.* a register, can assume  $2^n$  possible states, drastically improving the computational power with respect to traditional approaches. In particular, such an extension of the complex space is mathematically performed by recurring to the tensor product operation  $\otimes$ .

However, because of special constraints on the quantum system, sometimes it is not possible to factorize the related register in terms of its standard basis. Such a situation describes the entanglement between the constitutive Qubits of the system. Considering, for instance, the register defined by  $|\psi\rangle = \frac{1}{\sqrt{2}}|00\rangle + \frac{1}{\sqrt{2}}|11\rangle$ , it is possible to notice that the 2 Qubits that define it are linked in the way in which a measurement of one of the two will make the system to collapse at 50% either in  $|00\rangle$  or  $|11\rangle$ : if the measured Qubit is found to be  $|0\rangle$ , then also the other one, even without measuring it, will be for sure described by the  $|0\rangle$  state.

### 1-Qubit Gates

Additionally to the measurement operation, which basically performs a collapse of a 2 energy-levels system on a ground or on an excited state, it is possible to define many other operations to perform on a Qubit: in this sense, such operations can be modelled as it is done in classical computational theory, by means of logic gates. This last abstraction for modelling quantum algorithms is known as quantum circuit theory.

However, differently from traditional circuits, in which only a single 1-bit gate can be defined (*i.e.* the NOT operation), because of the matrix description of Qubits, many quantum gates can be introduced.<sup>5</sup> The most important quantum gates that can be defined over a single Qubit  $|\psi\rangle = \alpha|0\rangle + \beta|1\rangle$  are, therefore, the following ones:

$$\begin{aligned}
 X &= \begin{pmatrix} 0 & 1 \\ 1 & 0 \end{pmatrix} & \Big| & X|\psi\rangle = \beta|0\rangle + \alpha|1\rangle \\
 Y &= \begin{pmatrix} 0 & -j \\ j & 0 \end{pmatrix} & \Big| & Y|\psi\rangle = -j\beta|0\rangle + j\alpha|1\rangle \\
 Z &= \begin{pmatrix} 1 & 0 \\ 0 & -1 \end{pmatrix} & \Big| & Z|\psi\rangle = \alpha|0\rangle - \beta|1\rangle \\
 H &= \frac{1}{\sqrt{2}} \begin{pmatrix} 1 & 1 \\ 1 & -1 \end{pmatrix} & \Big| & H|\psi\rangle = \alpha \frac{|0\rangle + |1\rangle}{\sqrt{2}} + \beta \frac{|0\rangle - |1\rangle}{\sqrt{2}}
 \end{aligned}$$

$X$ ,  $Y$  and  $Z$  are the well-known Pauli matrices defined in quantum mechanics, describing the spatial components of the 1/2-spin momentum operator (in this computational

---

<sup>5</sup>In particular, in order to preserve the correct normalization of quantum states, a quantum gate will be defined as a unitary matrix  $A$  on  $\mathbb{C}^{2^n \times 2^n}$ . Such matrices are able to transform a Qubit into another Qubit if only if they respect the condition for which  $A^\dagger = (A^T)^* = A^{-1}$  (see [9]).

model,  $X$  plays the role of the NOT gate, basically inverting the state probabilities of the Qubit). On the other hand,  $H$  is the so-called Hadamard gate and it has the peculiar property to transform whatever Qubit in a superposition that can be either  $|0\rangle$  or  $|1\rangle$  with equal probabilities: reasoning on the Bloch sphere, it rewrites the Qubit state, defined in the canonical base, in terms of the on-plane  $x$ -basis (see Figure 1.2(b)).

## 2-Qubits Gates

Dealing with many-Qubits gates, several interesting matrices have been proposed along the last decades, in order to implement more and more sophisticated quantum algorithms and optimize the ones already elaborated. However, one of the most relevant gates defined on 2-Qubits registers is the so-called CNOT (or, better, controlled-NOT); such an operator basically implements the classical XOR function on two Qubits, negating the *controlled* Qubit  $b$  if only if the *control* Qubit  $a$  is  $|1\rangle$ . In the Dirac matrix notation, the CNOT can be defined as following:

$$CNOT = \begin{pmatrix} 1 & 0 & 0 & 0 \\ 0 & 1 & 0 & 0 \\ 0 & 0 & 0 & 1 \\ 0 & 0 & 1 & 0 \end{pmatrix} \quad \Bigg| \quad CNOT|a, b\rangle = |a, a \oplus b\rangle$$

As reported in [9], it is possible to demonstrate that the set formed by the  $X$ ,  $Y$ ,  $Z$  and  $H$  1-Qubit gates, plus the  $CNOT$  2-Qubits gate, is a universal set; this means that it is able to define each possible register-based  $U$  function as a controlled- $U$  quantum gate, being applied to the register when a control Qubit is  $|1\rangle$  and leaving the register unchanged when the control Qubit itself is  $|0\rangle$ . A deeper explanation of quantum information, and how quantum circuits allow to implement very exotic and beyond-classical-limits phenomena, lies outside the scope of this work: the reader is encouraged to refer to Mermin's book [9] for more information about such topics, as, for example, entangled Bell's states, quantum teleportation and superdense coding.

## 1.2 State of the Art for Many-Qubits Systems

As it has been possible to perceive from the previous general introduction to quantum information, QC really possesses revolutionary potentialities for surpassing classical computation: relying on quantum mechanics laws, it, actually, allows to exploit their intrinsic parallelism for simultaneously take into account a  $2^n$  space of possibilities, drastically boosting current computational power. Moreover, QC also enables the possibility to exploit physical phenomena completely beyond the limits of classical physics (*i.e.* entanglement) in order to overcome intractable problems for today's information schemes.

However, even if such wonderful opportunities have been deeply studied and understood in quantum information theory, quantum processors are still on the way to be effectively

implemented in working machines. As a matter of fact, in the last decades, a huge effort has been spent in order to provide many possible solutions for such an implementation; nowadays, many challenges still need to be addressed for realizing that new 21<sup>th</sup> century information revolution.

### 1.2.1 DiVincenzo's Criteria

Since the fundamental unit in QC is the Qubit, from quantum circuits theory, the reader could be erroneously induced in thinking about a quantum computer as a simple fistful of Qubits and quantum gates, connected together for performing calculation. Unfortunately, exactly like a classical computer is not merely a collection of bits, an effective quantum computer can not be described in this way, but it must also satisfy many physical constraints, in order to address Qubits in a correct way, perform a universal set of quantum operations and provide a reliable readout mechanism.

In this perspective, in 2000 the American physicist David P. DiVincenzo introduced a set of 5 requirements, known as *DiVincenzo's criteria*, which provide the most essential specifications that a new experimental proposal has to respect in order to be eligible as an effective solution for building up a working quantum computer. Such criteria, reported for the first time in [6], basically state that an effective solution for QC should necessarily provide:

1. **"A scalable physical system with well characterized Qubits"**

As previously explained in §1.1.2, a Qubit is nothing more than a quantum system with 2 possible states, sufficiently separated in energy to make them clearly distinguishable. In this sense, a quantum computer should rely on a fundamental Qubit unit whose Hamiltonian is well characterised, including, therefore, the definition of its energy eigenstates, namely,  $|0\rangle$  and  $|1\rangle$ .

2. **"The ability to initialize the state of the Qubits to a simple fiducial state"**

In quantum circuits model, it is fundamental to have the possibility to initialize the state of registers: actually, before starting any computation, initial states must be known with high accuracy, in order to properly apply the right set of operations and obtain the correct results. Moreover, many well-known Qubits are necessary also for quantum error correction algorithms, which largely use ancillary Qubits in order to recover the correct state for computing registers.

3. **"Long relevant decoherence times, much longer than the gate operation time"**

Because of the extremely fragile nature of quantum systems, which can be simply perturbed by interactions with the external environment and measurement apparatuses, computations must be performed quickly, for Qubits not to lose quantum properties. In this perspective, each physical Qubit is characterised by a

decoherence time, after which quantum information is irretrievably lost: a quantum computer should, therefore, be designed for allowing a significant amount of operations to take place before the information is definitely corrupted.

4. "A universal set of quantum gates"

In order to implement effective quantum algorithms, which are essentially a sequence of unitary matrices, a QC solution should provide a specific *universal* set of quantum gates able to produce each possible quantum function, realizing also all traditional functions in the limit of classical computation. In this sense, *CNOT*-based gates are really important building blocks, since they allow to set up *controlled* functions, applying or not an Hamiltonian transformation depending on the state of a control Qubit.

5. "A Qubit-specific measurement capability"

Even if, thanks to the collapse principle, measurements allow a quantum system to assume only a single state over the  $2^n$  space of possibilities, it is not trivial to really understand if such a measure is the effective result of the computation, another possible result with a non-negligible probability, or, even worse, a completely wrong result due to quantum interference. So, a quantum computer should be designed in order to provide a sufficient accuracy in the measurement apparatus, as well as the possibility to perform different measurements in the same conditions, in order to get a statistics of the possible computation results.

### 1.2.2 Physical Implementations of Quantum Bits

All along the very last decades, many different typologies of Qubits have been studied, designed and implemented, in order to build up a quantum computer effectively satisfying DiVincenzo's criteria. In the following, a brief description of some of the most promising candidate technologies will be presented, highlighting the respective advantages and drawbacks for each of them; in particular, Figure 1.3 reports a comparison between some of the most important candidate technologies for Qubits implementation.




	Superconductor	Si spin	Trapped ions	Photons
 Size	(100µm) <sup>2</sup>	(100nm) <sup>2</sup>	(1mm) <sup>2</sup>	~(100µm) <sup>2</sup>
 Fidelity	~99,3%	>98%	99,9%	50% (mesure) 98% (portes)
 Speed	250 ns	~5 µs	100 µs	1 ms
Manufacturing				
Variability	3%	0.1%-0.5%	0.01%	0.5%
Operation T°	50mK	1K	300K	4K
Entangled qubits	20	2	20	18

Figure 1.3: Qualitative comparison between different QC technologies [10]

### Superconducting Qubits

Such a technology is the one that is currently adopted by major companies like IBM, Google and Intel. In practice, as reported in [11], it relies on the implementation of a quantum harmonic  $LC$ -oscillator, in which a non-linearity factor is introduced by means of a Josephson's junction inductor. In this way, two different energy states can be addressed by two different microwave signals. Moreover, the readout is performed by recurring to a superconducting inductance coupled to the quantum circuit, originating a resonance condition whose frequency is depending on the state of the Qubit.

The main advantages of superconducting Qubits are the possibility to entangle the state of many quantum bits, thanks to the inductive coupling, the high readout fidelity and the very fast operation speed that it is possible to achieve. However, their manufacturing processes are not trivial to implement and the dimensions that such devices can get, for many Qubits processors, place a limit for scalability.

### Trapped Ions Qubits

Another important implementation of quantum bits is the one based on trapped ions. As explained in [12], such a technology basically relies on the possibility to isolate single ions on a linear chain by means of strong oscillating electric fields and address them individually by laser excitations. In so doing, the electronic levels of each ion are excited at characteristic frequencies, by means of electric quadrupole transitions, while readout is achieved by the emissions of photons, under on-resonance light excitation.

As for superconducting Qubits, also trapped ions can be easily entangled in many-units groups on linear chains and the fidelity readout can reach levels well beyond 98%: furthermore, in this case, coherence time is much longer, even up to tens of seconds, thanks to the intrinsic electromagnetic isolation necessary to build up two-levels systems. Unfortunately, the main drawbacks of these devices lay on the big dimensions that even a small processor can get and the very slow Qubit operations, implemented by recurring to laser exposure.

### Photonic Qubits

Linear Optical Quantum Computing (LOQC), is one of the first proposal for the implementation of a QC architecture. Such an approach is based on the use of light, in particular single photons, for encoding quantum information and perform computation over it. As a matter of fact, the polarization of a photon naturally results in the translation into a single Qubit (see [13]): quantum gates are, consequently, implemented by recurring to linear optical systems based on mirrors, beam splitters and interferometers, while readout operations are performed by means of photodetectors.

LOQC allows to easily entangle together many different Qubits and, differently from any other approach, it provides a concrete way to implement both quantum information and quantum communication in the same system, relying on photonic energy transfer.

However, the main drawbacks affecting such a technology are the relatively poor scalability, due to the remarkable dimensions of the apparatuses, and the still quite small readout fidelity, influenced by external electromagnetic interferences.

### 1.2.3 CMOS-Compatible Silicon Spin Qubits

Electron spin is probably one of the most well-known two levels quantum systems: in particular, the possibility to clearly distinguish electrons in spin-up and spin-down populations could, in principle, suggest its trivial implementation as a quantum bit. Unfortunately, even if spin-based QC was first proposed already in 1998 (see [14]), its practical implementation has become effective only in the very last years (see [15] and [16]), with the recent improvements in technological processes for isotopically purifying silicon from  $^{29}\text{Si}$  non-zero nuclear spin atoms. In so doing, the interaction between electron spin Qubits and the surrounding spin population has become weaker and weaker, which allowed to increase decoherence time up to milliseconds, as reported in [17], making spin based QC a valid alternative to the aforementioned technologies.

#### Working Principle

The basic idea for the implementation of a silicon spin Qubit is to encode quantum information inside electronic spins: to do so, electrons must be individually addressable and, nowadays, two possible approaches have been proposed to isolate single spins, relying on donor impurity atoms in the Si substrate or on double Quantum Dots (QDs) (see, respectively, [15] and [16]). For what it concerns QDs-based Qubits, a Single-Electron Transistor (SET) is realized by means of a silicon nanowire on which two control gates are placed, electrostatically isolating single electrons into two separated quantum islands (see Figure 1.4(a)).

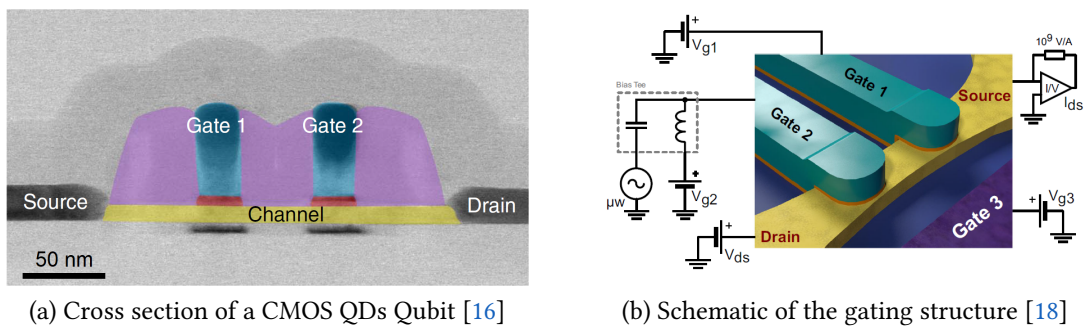


Figure 1.4: Representation of a CMOS based silicon spin Qubit

By controlling the gate voltages on the QDs, it is, therefore, possible to exploit electron tunneling and Coulomb's blockade phenomena, as reported in [19], to make a measurable single electron (or, alternatively, hole) current circulating from the drain



to the source reservoirs. In particular, in Figure 1.4(b) is reported a schematic clearly showing the source, drain and gates connections for such a double QDs SET device.

### Readout and Control of Spin Qubits

As explained in [19], by applying an external static magnetic field  $\mathbf{B}_0$ , it is possible to separate the discrete energy levels inside the two quantum dots by means of the well-known Zeeman splitting phenomenon. In such a way, a fine control of the energy difference between the two gate voltages, usually referred to as *detuning*, allows to properly align or misalign the electrons QDs energies, in order to make inter-dots tunneling possible basing on the spin state of the two electrons. As a matter of fact, if one of the two electrons (looking at Figure 1.4(b), the one associated to gate 1), having a known spin value, is kept in its respective QD as a spin filter, the other one, controlled by gate 2, will tunnel to the second dot, originating a measuring current, only if it has an opposite spin value. Such a phenomenon, known as Pauli's blockade, is actually exploited to perform the measurement of the electron spin state, implementing the so called spin-to-charge conversion readout.

On the other hand, coherent spin control can be realized by recurring either to Electron Spin Resonance (ESR) or to Electric-Dipole Spin Resonance (EDSR), as reported, respectively, in [15] and in [18]: a microwave magnetic (or electric) field is applied to the Qubit electron spin under gate 2, enabling spin-up to spin-down conversion on the Bloch sphere and making possible to design single Qubit gates. Such a control mechanism will be explained more in details in §3.2.2, where it will be compared to ESR and EDSR techniques will be compared.

To sum up, in order to fully understand the functioning of such a device, the reader should keep in mind that the double QDs structure is essentially implementing a single Qubit, in which the first confined electron is the one effectively storing quantum information, while the second one is crucial for sensing operations.

### Silicon CMOS Technology Scalability

Because of the mature technological processes, which have been implemented and optimized all along the last decades, silicon spin QC relies on a well-established and highly scalable CMOS compatible manufacturing. The main advantage over the aforementioned competitor solutions is, therefore, the great scalability that such an approach can offer, allowing, in principle, to design a quantum processor with many interconnected Qubits. In so doing, a silicon based quantum computer could easily manage complex quantum algorithms and implement error-correction protocols, which are essential to perform accurate calculation in the current technology, still suffering from relevant noise-induced

decoherence phenomena.<sup>6</sup>

In order to exploit such a powerful integration feature, many different and innovative architectures have been reported: for example, in [21], a multi-level stack with integrated CMOS transistors has been developed for addressing donor spin Qubits, while [22] has proposed a particular crossbar network for controlling and reading quantum dots Qubits, in a way similar to the one currently used in solid state memories. In particular, as presented in Figure 1.5, CEA is currently investigating 2D and 3D architecture relying on the recently improved vertical implementation of silicon nanowires, which allows to design an array of QDs, having separated bottom-up interconnecting stacks, respectively performing readout and control operations.

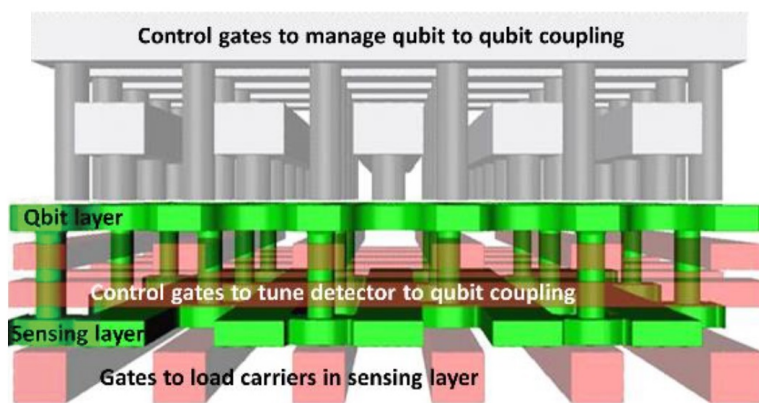


Figure 1.5: 3D interconnections array for CMOS quantum computing [23]

### 1.3 Objectives

In the framework of CEA’s effort to develop architectures for a silicon CMOS-compatible quantum processor,<sup>7</sup> this internship project is devoted to the study of RF control and readout interconnects integrated on the same quantum chip containing the spin Qubits. In this sense, 1-metal layers RF interconnections will be analysed, dealing, first, with the transmission of RF signals, using Coplanar Waveguides, then focusing to integrated solutions of Electron Spin Resonance and Gate Reflectometry techniques, respectively oriented to the control and the readout of spin Qubits.

<sup>6</sup>Unfortunately, the most important drawback of silicon spin Quantum Computing is the limited number of entangled Qubits that has been reached so far: nowadays, a great effort is spent by research groups to overcome such a limitation, which is still fixed to only 2 entangled Qubits, as reported in [20].

<sup>7</sup>Visit <https://www.quantumsilicon-grenoble.eu/> for more information about the collaboration project between Grenoble CEA-LETI, CEA-IRIG and CNRS Institut Néel.

Some industrial dedicated softwares will be, therefore, exploited for simulating such structures, allowing to accurately evaluate RF performances of some of the aforementioned interconnect networks for CMOS quantum bit systems. For instance, in this work only 1-metal layer structures will be considered and simulated, dealing with the On-Chip integration of spin Qubits control and readout structures. In particular, such softwares, like ANSYS® HFSS® and CST Studio Suite®, recur to full 3D electromagnetic solvers based on Maxwell's equations resolution, here reported for the sake of completeness:

$$\left\{ \begin{array}{l} \nabla \cdot \mathbf{D}(\mathbf{r}, t) = \rho(\mathbf{r}, t) \\ \nabla \cdot \mathbf{B}(\mathbf{r}, t) = 0 \\ \nabla \times \mathbf{E}(\mathbf{r}, t) = -\frac{\partial \mathbf{B}(\mathbf{r}, t)}{\partial t} \\ \nabla \times \mathbf{H}(\mathbf{r}, t) = \mathbf{J}(\mathbf{r}, t) + \frac{\partial \mathbf{D}(\mathbf{r}, t)}{\partial t} \end{array} \right.$$

In this case,  $\mathbf{E}$  and  $\mathbf{D}$  respectively define the electric field and the electric displacement field, while  $\mathbf{H}$  and  $\mathbf{B}$  are the magnetic field strength and the magnetic flux density;<sup>8</sup> moreover,  $\rho$  represents the electric charge density inside the system (not handled for this kind of softwares) and  $\mathbf{J}$  is the electric current density circulating through the system.

---

<sup>8</sup>In this work, no material with particular or anisotropic dielectric and magnetic properties is analysed: the relations between the aforementioned fields are, therefore, simply  $\mathbf{D} = \epsilon_0 \epsilon_r \mathbf{E}$  and  $\mathbf{B} = \mu_0 \mu_r \mathbf{H}$ , being  $\epsilon_0 \simeq 8,854 \times 10^{-12} \text{ F/m}$  and  $\mu_0 \simeq 1,257 \times 10^{-12} \text{ H/m}$  the vacuum permittivity and permeability, while  $\epsilon_r$  and  $\mu_r$  define the material relative permittivity and permeability. In particular, since no magnetic material will be considered,  $\mu_r = 1$  and it will be indifferently used the term "magnetic field" for indicating both  $\mathbf{B}$  and  $\mathbf{H}$ -fields, keeping in mind that  $\mathbf{B} = \mu_0 \mathbf{H}$ .



## Chapter 2

# Coplanar Waveguides Technology For On-Chip RF Routing

### 2.1 Introduction

Because of the physical nature of Si spin-based Qubits and the decoherence time limited to milliseconds, control and readout circuitries for CMOS-compatible quantum systems must work at RF, in particular in ultra-high-frequency (UHF) and super-high-frequency (SHF) ranges: in other words, electronic circuits must be able to easily address signals for frequencies ranging from  $300\text{ MHz}$  to  $30\text{ GHz}$ . Moreover, in order to build up an effective quantum chip able to address many Qubits systems, well-established Si microelectronic VLSI techniques offer a unique tool for easily design and project ideal quantum processors at micro and nano-scales.

Unfortunately, when such an On-Chip scaling technology is exploited, at those frequency ranges, electric wavelengths  $\lambda$  and circuit characteristic lengths  $L$  start to become comparable, in the order of millimetres, making impossible to still neglect the propagating wave-like behaviour of electric signals. In so doing, in this electromagnetic conditions, classical lumped-parameters theory does not hold any more and it is necessary to recur to distributed-parameters theory when designing Monolithic Microwave Integrated Circuits (MMIC). In particular, in the last decades, as reported in [24] and [25], many different technologies for implementing RF electrical routing in microelectronics have been proposed, such as, for example, microstrips, coplanar striplines (CPS) and coplanar waveguides (CPW).

The aim of this chapter is to globally study the main performances of On-Si CPW technology for the implementation of microwave transmission lines. To do so, it will

first introduce the most important concepts of distributed-parameters circuits theory.<sup>1</sup> In a second time, the main results concerning the simulation of an Al On-Si and On-Insulators CPW will be reported, extracting the most relevant distributed parameters for the modelling of the transmission lines.

## 2.2 Transmission Lines Theory

Considering a metallic rectangular interconnection, like the one depicted in Figure 2.1(a), in which the transversal dimensions  $a$  and  $b$  are far smaller than the wavelength of the propagating electric signal  $\lambda$ , but the longitudinal dimension is  $L \sim \lambda$ , then the classical electric quantities, namely voltage and current, can not be considered constant all along the interconnection length. In a time instant  $t_0$ , actually,  $V$  and  $I$  will be a function of the position along the line: in the most basic case for a loading connection (see Figure 2.1(b)), such a situation can be no more modelled like a lumped-component, but it should be also defined in terms of the line length. To do so, a different circuit theory, defined for the first time in the last years of the 18<sup>th</sup> century, known as transmission lines theory, must be adopted.

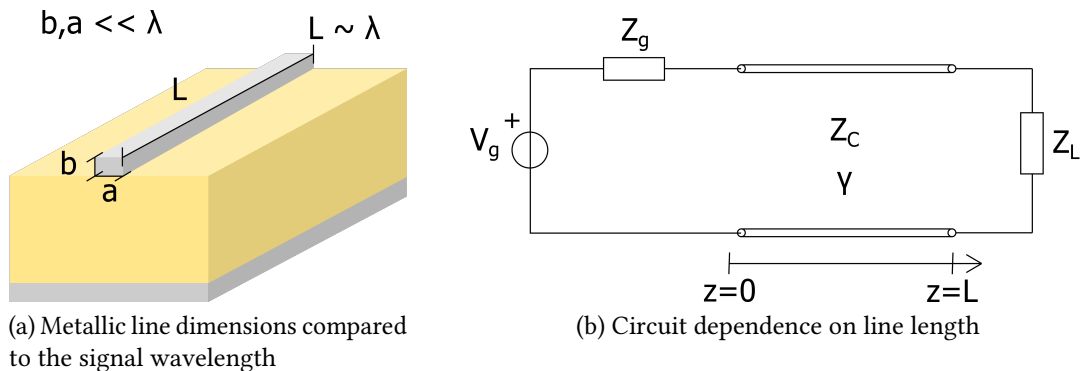


Figure 2.1: Distributed-circuit model of a microstrip line

### 2.2.1 Telegrapher's Equations

In the general case of the previous example, it has been shown that voltages and currents are not constant along the line, but they are functions of the longitudinal position  $z$  and time  $t$ , as  $v(z, t)$  and  $i(z, t)$ . Even if lumped-circuits theory is no more valid, it is still possible to apply it to an infinitesimally  $\Delta z$ -long section of the line, as reported

<sup>1</sup>Such aspects will be fundamental not only for the description of CPW transmission lines, but they will be also largely exploited when dealing with the ESR line and the readout inductance in the following parts of this work.

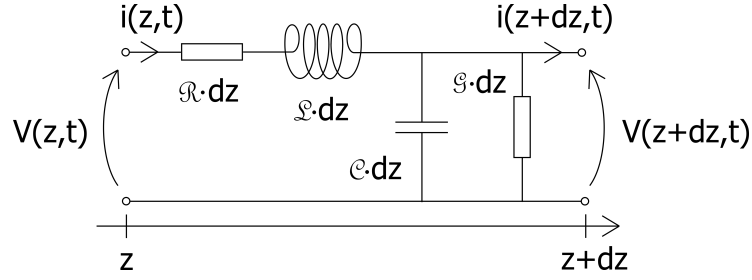


Figure 2.2: Differential lumped model of the transmission line

in Figure 2.2. By applying Kirchoff's laws, one can easily get the so-called differential Telegrapher's equations, first derived by Oliver Heaviside in 1876:

$$\begin{cases} -\frac{\partial}{\partial z} v(z, t) = \mathcal{R} i(z, t) + \mathcal{L} \frac{\partial}{\partial t} i(z, t) \\ -\frac{\partial}{\partial z} i(z, t) = \mathcal{G} v(z, t) + \mathcal{C} \frac{\partial}{\partial t} v(z, t) \end{cases} \quad (2.2.1.1)$$

where  $\mathcal{R}$  [ $\Omega/m$ ],  $\mathcal{L}$  [ $H/m$ ],  $\mathcal{G}$  [ $S/m$ ] and  $\mathcal{C}$  [ $F/m$ ] are, respectively, the distributed resistance, inductance, conductance and capacitance of the transmission line.

### Helmholtz Formulation

By redefining  $v(z, t)$  and  $i(z, t)$  in the  $\omega$  frequency domain as phasors  $V(z, \omega)$  and  $I(z, \omega)$ , it is possible to demonstrate (see [24]) that Equations 2.2.1.1 can be reformulated as

$$\begin{cases} -\frac{d}{dz} V(z, \omega) = j\omega \mathcal{L}_C I(z, \omega) \\ -\frac{d}{dz} I(z, \omega) = j\omega \mathcal{C}_C V(z, \omega) \end{cases} \quad (2.2.1.2)$$

being  $\mathcal{L}_C = \mathcal{L} + \frac{\mathcal{R}}{j\omega}$  and  $\mathcal{C}_C = \mathcal{C} + \frac{\mathcal{G}}{j\omega}$ .

In particular, by further differentiating in space, it is possible to combine together Equations 2.2.1.2, in order to get:

$$\begin{cases} -\frac{d^2}{dz^2} V(z) + \gamma^2 V(z) = 0 \\ -\frac{d^2}{dz^2} I(z) + \gamma^2 I(z) = 0 \end{cases} \quad (2.2.1.3)$$

Such expressions are essentially a form of Helmholtz equations, which can describe the propagation of travelling waves along the line in the frequency domain; in particular,  $\gamma = j\omega \sqrt{\mathcal{L}_C \mathcal{C}_C} = \sqrt{(\mathcal{R} + j\omega \mathcal{L}) \cdot (\mathcal{G} + j\omega \mathcal{C})}$  is one of the two complex parameters describing the transmission line, called propagation constant.

## Travelling Waves

As previously suggested, Equations 2.2.1.3 define a wave-like propagation of voltages and currents along the line. As a matter of fact, the solutions for Helmholtz equations can be written in terms of a combination of a forward-propagating wave and a backward-propagating wave, resulting in

$$V(z) = V(z)^+ + V(z)^- = V(0)^+ e^{-\gamma z} + V(0)^- e^{+\gamma z}$$

$$I(z) = I(z)^+ + I(z)^- = I(0)^+ e^{-\gamma z} + I(0)^- e^{+\gamma z} = Y_C \cdot ((V(0)^+ e^{-\gamma z} - V(0)^- e^{+\gamma z}))$$

having introduced  $Y_C = Z_C^{-1}$  for the relations  $V(z)^+ = Z_C I(z)^+$  and  $V(z)^- = -Z_C I(z)^-$ . In particular,  $Z_C$  and  $Y_C$  define, respectively, the characteristic line impedance and admittance, which basically determine the second complex parameter describing, together with  $\gamma$ , the transmission line. As reported in [24], the line impedance is essentially defined as:

$$Z_C = \sqrt{\frac{\mathcal{R} + j\omega\mathcal{L}}{\mathcal{G} + j\omega\mathcal{C}}} \quad (2.2.1.4)$$

## 2.2.2 Scattering Matrix Description for 1 and 2-Ports Devices

Another important concept to introduce in such a description is the one of scattering matrix  $\mathbf{S}$ . As a matter of fact, when dealing with electromagnetic fields,  $\mathbf{Z}$ ,  $\mathbf{Y}$  and  $\mathbf{ABCD}$  matrices, largely used in lumped-circuits theory, are not that much exploited, mainly because the definition of short and open conditions, necessary for the calculation of the related parameters, is not trivial to be set up with RF components.

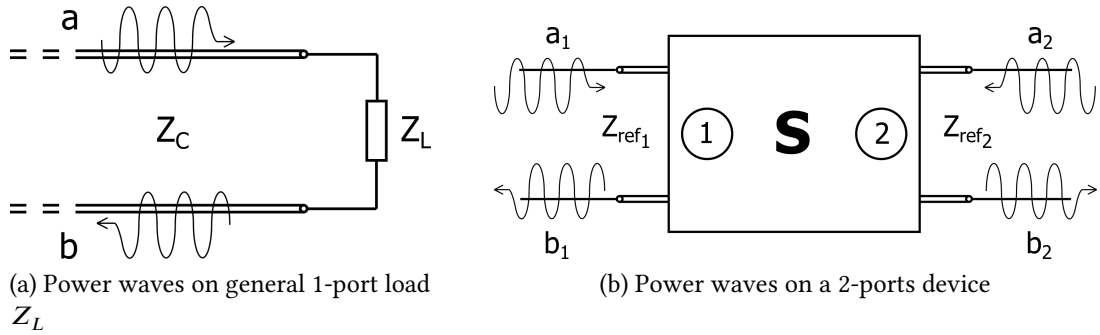


Figure 2.3: Representation for the derivation of  $\mathbf{S}$ -matrix

As explained in [24], considering an RF line delivering a certain power  $P_L$  to a general 1-port load  $Z_L$  (see Figure 2.3(a)), it is possible to define such a power by means of forward and backward propagating signals as

$$P_L = \frac{1}{2} \left( \frac{|V^+|^2}{Z_C} - \frac{|V^-|^2}{Z_C} \right) = \frac{1}{2} (|a|^2 - |b|^2)$$



where  $a = \frac{V^+}{\sqrt{Z_C}} = \frac{V(0)^+}{\sqrt{Z_C}} e^{-\gamma z}$  and  $b = \frac{V^-}{\sqrt{Z_C}} = \frac{V(0)^-}{\sqrt{Z_C}} e^{+\gamma z}$  are the generalized power waves.

Extending the same argument to whatever 2-ports device, whose ports have respectively  $Z_{ref_1}$  and  $Z_{ref_2}$  reference impedances, its electrical behaviour could be described in terms of the aforementioned quantities, as presented in Figure 2.3(b), by defining the scattering  $\mathcal{S}$ -matrix in the following way:

$$\begin{cases} b_1 = S_{11}a_1 + S_{12}a_2 \\ b_2 = S_{21}a_1 + S_{22}a_2 \end{cases} \Rightarrow S_{ii} = \left. \frac{b_i}{a_i} \right|_{a_j=0} \quad S_{ij} = \left. \frac{b_i}{a_j} \right|_{a_i=0}$$

In particular,  $S_{11}$  and  $S_{22}$  parameters define the amount of signal which is reflected by port  $i$  when excited by  $a_i$ , while  $S_{21}$  and  $S_{12}$  parameters define the amount of signal which is transmitted to port  $i$  when excited by  $a_j$ .<sup>2</sup>

## 2.3 Simulation of Coplanar Waveguides

In this section it will be discussed the simulation of a Coplanar Waveguide (CPW) transmission line, in order to evaluate its performances for On-Chip RF electrical routing. In particular, such an analysis will be carried out by means of High-Frequency Structure Simulator (HFSS<sup>®</sup>) software by ANSYS<sup>®</sup>; as many other HF-simulation softwares, HFSS<sup>®</sup> basically allows to address 3D RF structures by solving Maxwell's equations for Finite-Element-Methods (FEMs) applied all over the system.<sup>3</sup>

Considering, for example, CPW transmission lines using a single metallization layer, such a geometry, reported in Figure 2.4(a), is essentially described by three conducting metallic stripes running in parallel over a dielectric material (in most cases, silicon, silicon dioxide or an insulating material layer for front-end or back-end stack passivation); the two outermost lines are ground lines, collecting the electromagnetic field generated by the central line, carrying the microwave signal.<sup>4</sup>

With respect to other coplanar lines typologies, such as microstrips and striplines (see, respectively, Figure 2.4(c)-(d)), CPWs allow both to confine the fields close to the

<sup>2</sup>The no-reflection condition at port  $j$  when exciting port  $i$  is achieved by loading the first one exactly on a  $Z_{ref_j}$  impedance: this condition, called impedance matching, offers a unique termination which is, differently from shorts and opens, insensitive to RF component lengths.

<sup>3</sup>For more information about Ansys HFSS<sup>®</sup> software, visit <https://www.ansys.com/products/electronics/ansys-hfss>.

<sup>4</sup>An alternative version of CPW exists, presenting a bottom referencing ground plane for the collection of the signal (see Figure 2.4(b)): such a geometry is not suitable for silicon QC applications since a considerable amount of field is propagating through the underlying layers, possibly perturbing QDs spin readout mechanisms.

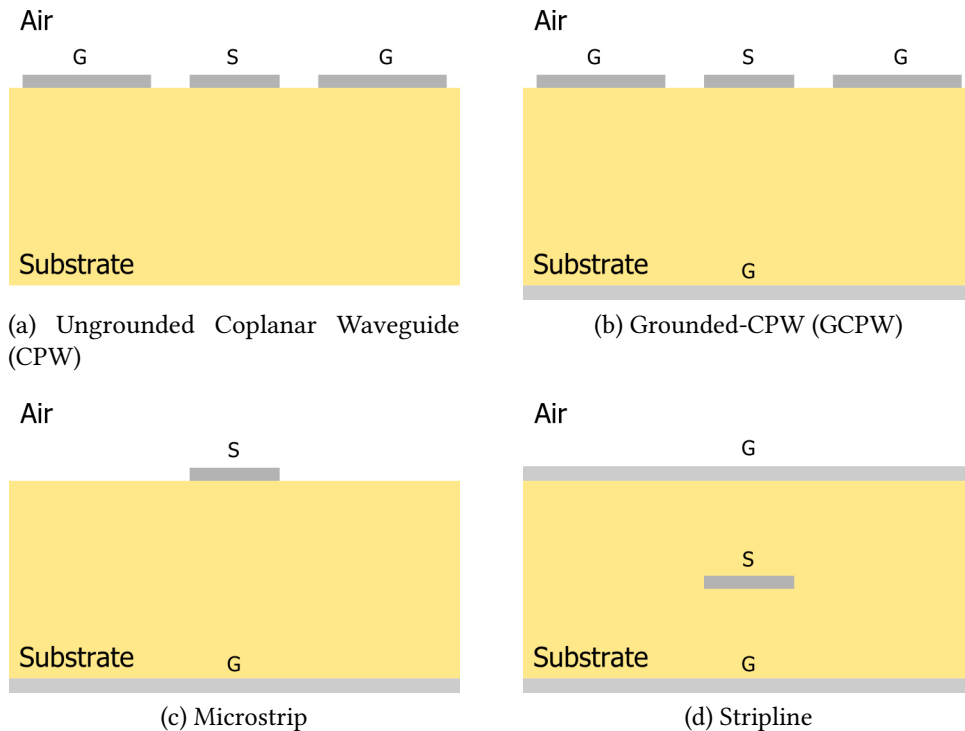


Figure 2.4: Different 1-metal layer coplanar transmission lines cross-sections

substrate outer surface, reducing parasitic losses and electric field intensity at the front-end QDs location (see §3.3.1), and give the possibility to connect to surface-mounted RF components. However, their design is trickier with respect to the alternative solutions, as reported in [25]. Moreover, unlike striplines, the substrate/air discontinuity causes CPWs mode to be hybrid instead of pure Transverse-Electric-Magnetic (TEM): fortunately, the characteristic line impedance has a quite constant broadband frequency behaviour, allowing a symmetric even Quasi-TEM mode to propagate along the line (see [25]).

### 2.3.1 Simulation Setup

Before proceeding with the presentation of the simulation results, a brief discussion about the simulation setup and methodology should be properly carried out. As a matter of fact, two main CPW structures will be analysed, consisting of a traditional Al line over a silicon substrate and another configuration involving an Al waveguide deposited on the top of two dielectric layers.

Moreover, it is essential to stress the procedure adopted to analyse the electromagnetic properties of such structures: when simulating electronic structures in the microwaves frequency domain, many aspects have to be preliminarily considered in order to obtain accurate results. In the following, it will be first presented the CPW geometry and, then,

some considerations about electromagnetic excitations and boundary conditions will be reported.

### CPW Geometry and Mesh Generation

The main coplanar waveguide configuration that is analysed all along this work is the one of an ungrounded-CPW: the basic structure of such a transmission line is reported, for the Al On-Si case, in Figure 2.5, in which are also highlighted its geometrical parameters.

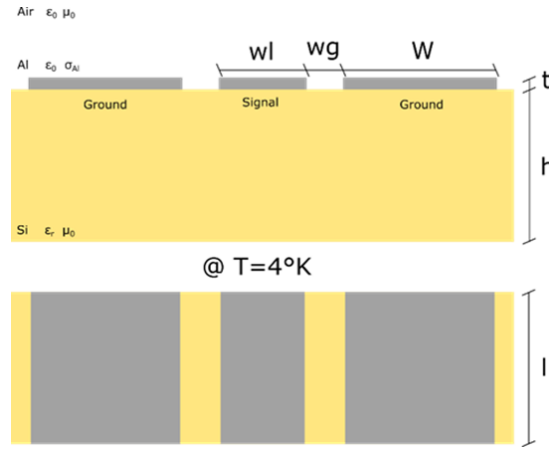


Figure 2.5: Cross-section and top view of the Al On-Si CPW

In particular, such a geometry is dimensioned as described in Table 2.1 in order to obtain a  $52 \Omega$  impedance matching at its extremities.<sup>5</sup> It is important to emphasize the fact that  $w_g = 180 \mu m$  is approximately chosen for the impedance matching condition: a more precise value for this parameter will be given in §2.3.2. Moreover, the silicon substrate relative permittivity is set to the default value of  $\epsilon_r \simeq 11,9$ , while a small finite conductivity is considered for accounting silicon loss effects at  $T = 4 K$ , so that  $\sigma_{Si} \simeq 10^{-5} S/m$ . On the other hand, Al conductivity is set to the room temperature value of  $\sigma_{Al} \simeq 3,8 \times 10^7 S/m$ : this quantity has been, actually, measured at cryogenic temperature and, for CEA technological processes, such a material has been found to not undergo a resistivity decrease: the room temperature value is, therefore, considered for a worst-case situation.

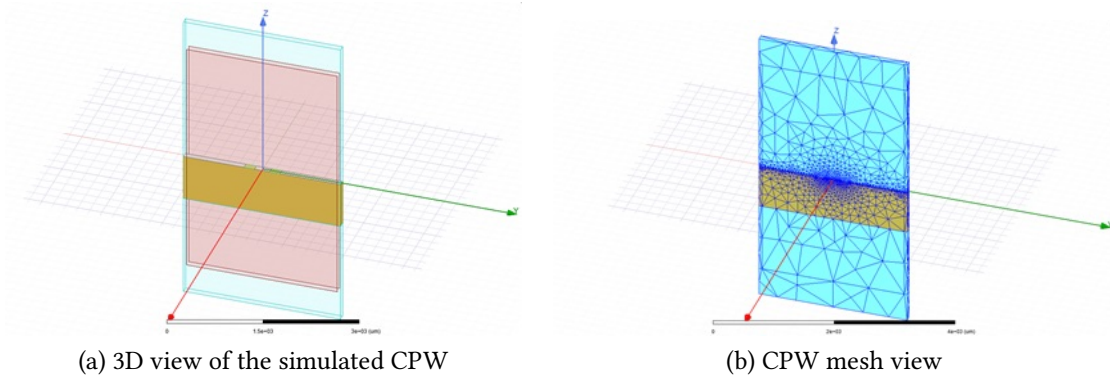
<sup>5</sup>In reality, a standard  $50 \Omega$  should be envisaged; however, because of parasitic capacitance effects (adding in parallel to the distributed capacitance  $\mathcal{C}$ , as described in Equation 2.2.1.4), which are related to the connection with other electronic components, the geometry is designed for a slightly higher impedance matching. Such parasitic capacitances are detrimental effects for the performances of the CPW line, contributing to mismatch losses if not taken into account during the design phase.

Dimension	Value	Geometrical Meaning
$w_l$	$250 \mu m$	Signal Line Width
$w_g$	$180 \mu m$	Gap Width
$W$	$1 mm$	Ground Lines Width
$t$	$200 nm$	CPW Thickness
$h$	$775 \mu m$	Substrate Thickness
$l$	$1 mm$	Whole CPW Length
$d$	$100 \mu m$	Simulated CPW Length

Table 2.1: Geometrical dimensions for the Al On-Si CPW

It is crucial to also notice that these geometrical values are established in order to provide one single propagating mode all over the simulated frequency range. According to [25], when a CPW is surrounded by a metallic enclosure,<sup>6</sup> the propagation of cavity modes is drastically limited if the CPW is designed so that:

$$\begin{cases} \frac{w_l+2w_g+2W}{w_l+2w_g} \simeq 4,29 > 1,75 \\ w_l + 2w_g = 610 \mu m < h = 775 \mu m \end{cases}$$


 Figure 2.6: 3D CPW simulated in Ansys<sup>®</sup> HFSS<sup>®</sup>

In so doing, only a single Quasi-TEM mode should propagate along the line for the whole simulated frequency range (*i.e.* between  $100 MHz$  and  $20 GHz$ ). The 3D geometry implemented by means of Ansys<sup>®</sup> HFSS<sup>®</sup> software is, therefore, reported in Figure 2.6(a): the reader should notice that only a small portion of the line is represented, instead of a  $l = 1 mm$  long CPW. As a matter of fact, only a  $d = 100 \mu m$  long CPW is

<sup>6</sup>Such a situation is usually set up, in order to shield the quantum chip against thermal gradients and electromagnetic radiations.

simulated, thanks to the possibility offered by HFSS<sup>®</sup> to de-embed the two ports, reducing simulation time, in order to virtually simulate a longer constant structure.

For what it concerns the meshing procedure of the structure, since the most of the electromagnetic field is concentrated in the region between the signal and ground line (see [26]), it is important to provide a sufficiently fine mesh all along the aluminium location. To do so, two limiting mesh element lengths of  $10\ \mu\text{m}$  and  $20\ \mu\text{m}$  are applied respectively to the signal and ground lines: the obtained mesh is reported in Figure 2.6(b), where it is possible to see the larger mesh density region for high accuracy fields calculation.

### Excitation Signals and Boundary Conditions

Considering the excitation signals, the CPW is electrically driven by its both sides by means of two waveguide ports: in so doing, a 2-ports simulation is performed for the structure under analysis. In Figure 2.7(a), in red, are shown the two port excitations: the HFSS<sup>®</sup> simulation is carried out in the *driven terminal* mode, meaning that the structure is controlled by means of a terminal voltage (for an injected power  $P_{in} = 0\ \text{dBm}$ ). To do so, the outermost sides of the ports have to touch the two ground lines, so that the software could recognize the reference ground metal lines for the central signal line. For the sake of completeness, the two blue arrows represent the  $450\ \mu\text{m}$  de-embedding for each section of the CPW, allowing the complete simulation of a  $1\ \text{mm}$  long transmission line.

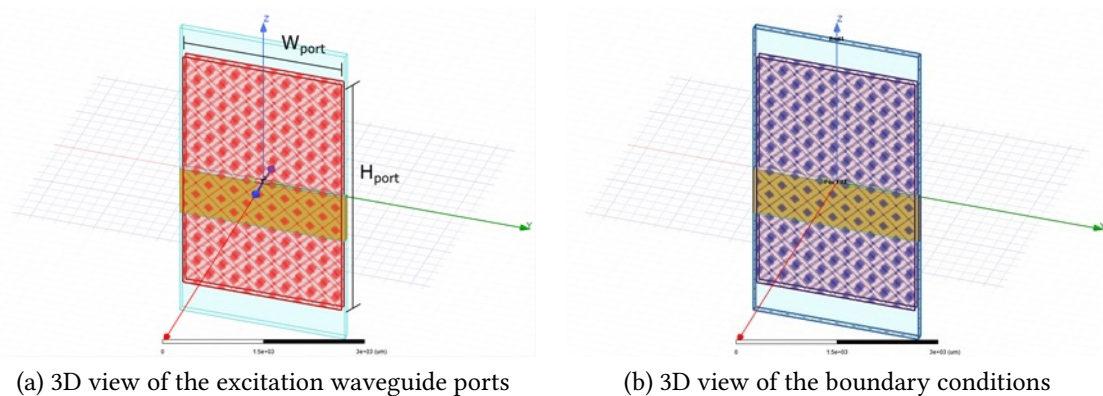


Figure 2.7: Excitation ports and boundaries for the simulated CPW line

On the other hand, in order to find the correct electromagnetic configuration for the injected signals, the solver needs also the definition of proper boundary conditions. In Figure 2.7(b) it is possible to notice the presence of two distinct kinds of boundaries. First, the blue surfaces surrounding the lateral sides of the system are *radiation* conditions, which allow the electromagnetic field to propagate indefinitely over the structure, without fixing any coupling or conducting wall. The two front and backside purple

surfaces stand, instead, for two *perfect-H* boundaries, meaning that the magnetic field at the waveguide ports has no longitudinal component, exactly like in a TEM mode.

### 2.3.2 Simulation Results of an Al On-Si CPW

Once having fully explained the simulation setup used for carrying out the analysis of such a CPW structure, it is now possible to proceed with the discussion of the obtained results. In particular, in this section there will be first reported the convergence criteria for correctly setting up the dimensions of the excitation ports; then, the port information for the Al On-Si line, such as *S*-parameters and fields distribution, will be presented and commented, checking the validity of the performed simulation and the correct matching conditions at the port locations.

#### Gap Dimensioning for an Optimal 52 Ω Matching

Before proceeding with the definition of the signal to ground gap  $w_g$ , it is important to correctly set up a sufficient  $W_{port}$  and  $H_{port}$  port sizing. Actually, the excitation ports must be adequately dimensioned in order to take into account enough field lines for the correct calculation of the initial field configuration; such a preliminary procedure, reported in appendix §A.1, is basically carried out by a sweep on the two port sizes, so that it is possible to finally find a convergence condition on the line impedance<sup>7</sup> for both values.

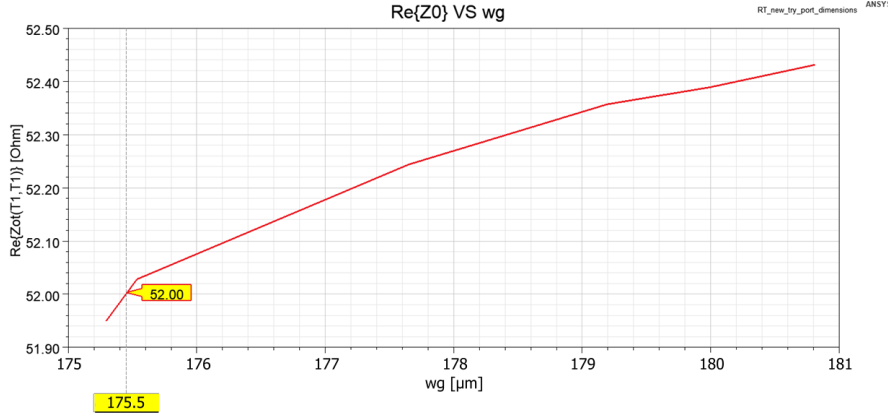


Figure 2.8:  $w_g$  optimization for 52 Ω impedance matching at 10 GHz

Once having fixed the correct waveguide port sizes, it is possible to perform an optimization analysis on  $w_g$ , in order to find a precise value for having the requested

<sup>7</sup>In particular, *Z<sub>0</sub>* quantity is the line impedance extracted by HFSS® at the waveguide port, basing on the calculation of the field distribution at the port location and depending on the geometry and materials characterizing the structure.

impedance matching condition. In so doing, by running such a sweep study between  $175 \mu m$  and  $185 \mu m$ , the most precise value for having a  $52 \Omega$  matching at  $10 GHz$  is found to be  $w_g \simeq 175,5 \mu m$ . Such an optimization analysis is displayed in Figure 2.8; in particular, the line impedance is found to increase for an increase in the gap: this behaviour is theoretically explained by the reduction of the distributed line capacitance,<sup>8</sup> which, according to Equation 2.2.1.4, contributes to the increase of the  $Z_C$  value.

### Ports Information

Under the previous conditions, the simulation of the aforementioned CPW line is carried out over a  $[100 MHz; 20 GHz]$  range; all along this whole frequency sweep, a single Quasi-TEM mode is propagating, validating the guidelines followed for the CPW design (see appendix §A.2).

$S$ -parameters are derived from the  $Z$  matrix extracted by the software: to do so, some conversion relations are exploited (see appendix §A.3). In Figure 2.9 are reported the frequency behaviours of the two ports  $S$ -parameters; since the line is a passive component, as reported in [24], the matrix is symmetric, implying that  $S_{12} = S_{21}$ . Furthermore, the structure is symmetric also along the longitudinal direction, meaning that the response to the excitation is the same on both port 1 and port 2 (*i.e.*  $S_{11} = S_{12}$ ).

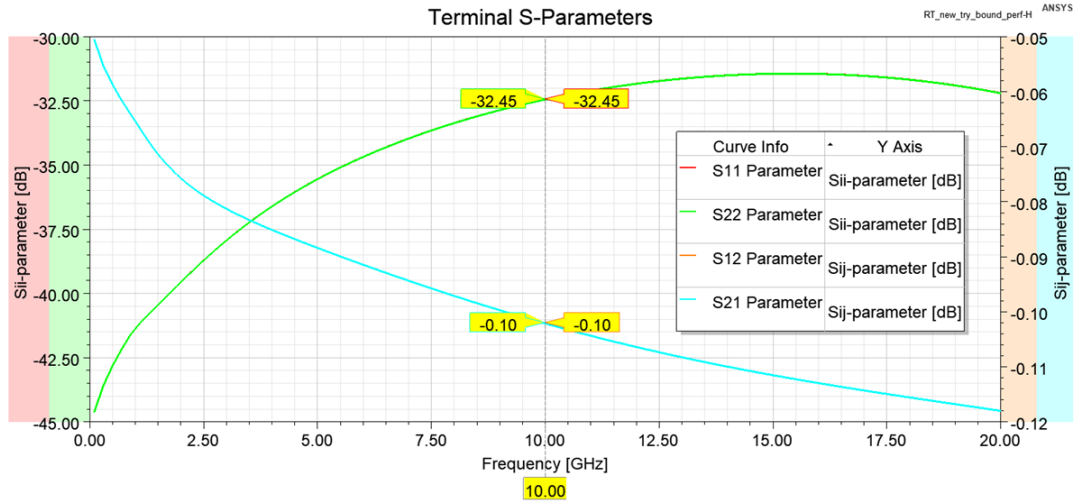


Figure 2.9:  $S$ -parameters for the Al On-Si CPW line

In particular, at  $10 GHz$ , the reflection coefficients  $S_{ii}$  result to be nearly  $-32,45 dB$ ,

<sup>8</sup>As a matter of fact, the capacitance between signal and ground lines can be seen made up of two components (one in the air region and the other one in the substrate) basically turning out to be two parallel plates, if operating a conformal mapping as explained in [27].

meaning that the reflection of the signal for mismatch conditions accounts for less than the 3%, providing a good confirmation for the correctness of the  $52\ \Omega$  matching procedure. For what it concerns the transmission coefficients,  $S_{ij} \simeq -0,10\ dB$ : such a value gives an idea about the losses inside the structure, which result to be low, as almost 98,85% of the signal is transmitted from port  $i$  to port  $j$ .

Finally, the line impedance is theoretically calculated by means of the expressions reported in appendix §A.3. In so doing, it is possible to compare the theoretical value of  $Z_C$ , coming from transmission line theory, to the geometrical  $Z_{ot}$  extracted by HFSS<sup>®</sup> at the two port locations. In Figure 2.10 it is actually possible to notice that the  $Z_C$  value behaves exactly as the simulated one, reaching an almost stable Quasi-TEM  $52\ \Omega$  real value at  $10\ GHz$  and converging to  $0\ \Omega$  on its imaginary part. Such a behaviour is exactly the one reported in literature (see [28]) and provides a positive check for the correctness of the results.

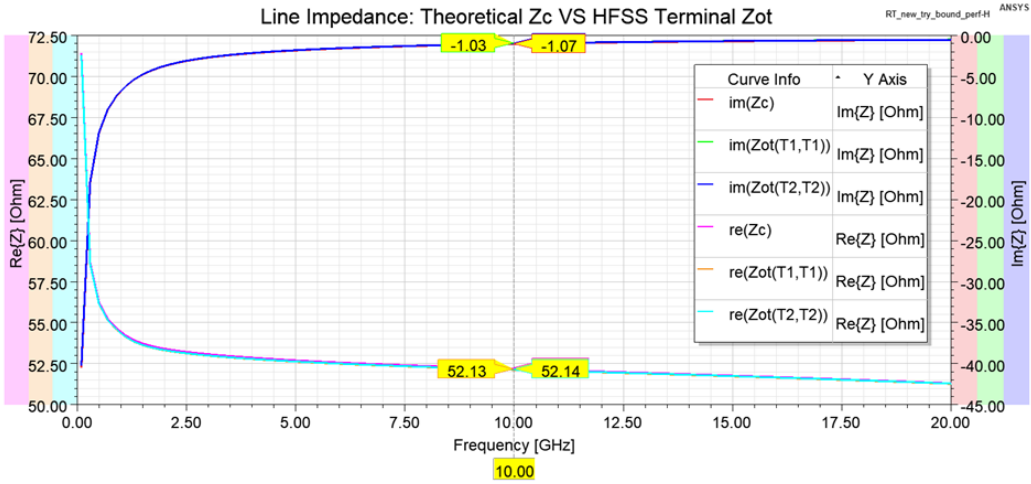


Figure 2.10: Real and imaginary parts of the CPW line impedance  $Z_C$

### 2.3.3 Simulation Results of an Al On-Insulators CPW

The second coplanar configuration under analysis is the one of an Al CPW line on a passivation dielectric layer, necessary for the isolation of the front-end Silicon-On-Insulator (SOI) stack from the back-end interconnections. Such a geometry recurs to a Buried Oxide (BOX)  $SiO_2$  region in order to decrease dielectric losses for the buried Qubits active circuitry, while the passivation insulating stack, made up of series of dielectric layers, is essential for the isolation of of microwave lines with respect to the underlying electronics. In Figure 2.11 is reported the cross-section of such a CPW: in particular, all the geometrical dimensions are kept exactly the same as the previous line, discussed in §2.3.1. However, in this case, two insulating layers are present, comprising an equivalent dielectric region,  $h_1 = 170\ nm$  thick, and a BOX, whose thickness is



$h_2 = 145 \text{ nm}$ , respectively having the dielectric constant equal to  $\epsilon_{r_{eq}} = 5$  and  $\epsilon_{r_{ox}} = 3,9$ .

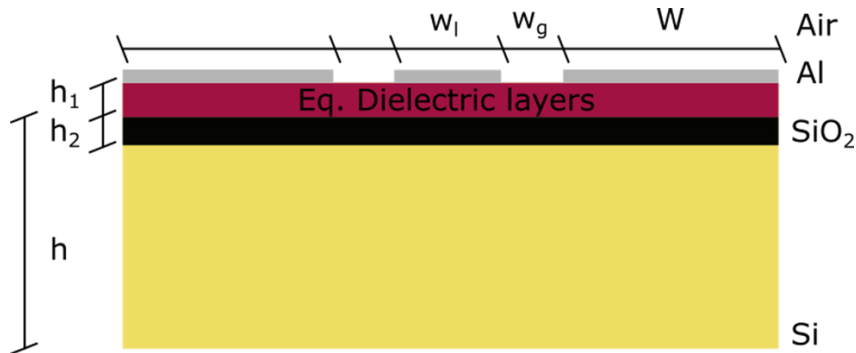


Figure 2.11: Cross-section showing the Al On-Insulators CPW structure

### Ports Information

As it has been already done for the Al On-Si CPW, also for this new geometry, an electromagnetic simulation between  $100 \text{ MHz}$  and  $20 \text{ GHz}$  is carried out by recurring to Ansys<sup>®</sup> HFSS<sup>®</sup> software. In particular, the setup necessary to run a correct analysis is exactly the one fully explained in §2.3.1: such a discussion will be, therefore, omitted, focusing with more attention on the obtained results.<sup>9</sup>

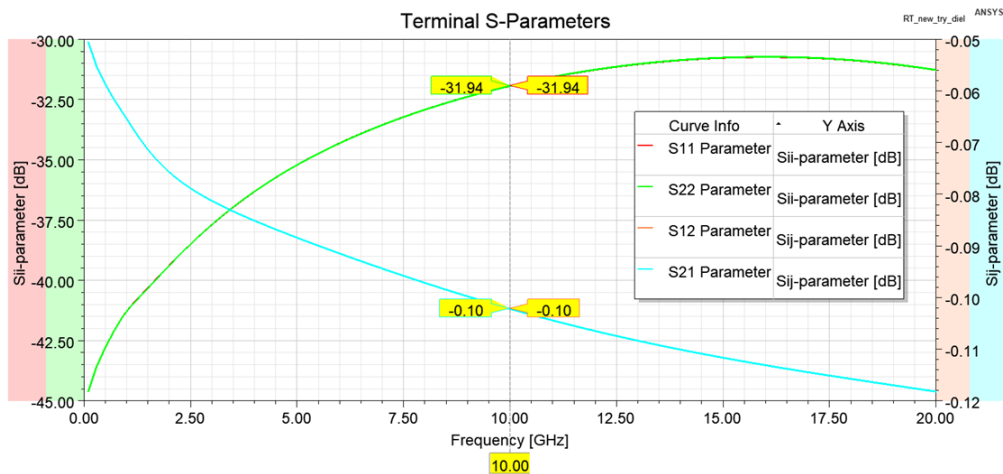


Figure 2.12: S-parameters for the Al On-Insulators CPW

<sup>9</sup>It is important only to mention that, because of the presence of the two thin insulating layers, a meshing length limitation to  $20 \mu\text{m}$  is applied not only to the metallic lines, but also to the dielectric regions.

First of all, the 2-ports  $S$ -parameters (see Figure 2.12), extracted by means of the formula reported in appendix §A.3, are equal to the Al On-Si structure, with a small difference for the reflection coefficients  $S_{ii}$ , meaning that the characteristic impedance matching of the line is a bit higher with respect to the previous case. As a matter of fact, such a possible explanation is confirmed by the frequency behaviour of the line impedance, reported in Figure 2.13, in which it is possible to see that  $Z_C \simeq 52,32 \Omega$  instead of the previous  $52,19 \Omega$  value: such a small increase, due to the presence of lower- $\epsilon_r$ , decreasing the line capacitance, is absolutely negligible, if considering the fact that the line impedance is still quite stable to an higher-than- $50 \Omega$  value all along the frequency range.

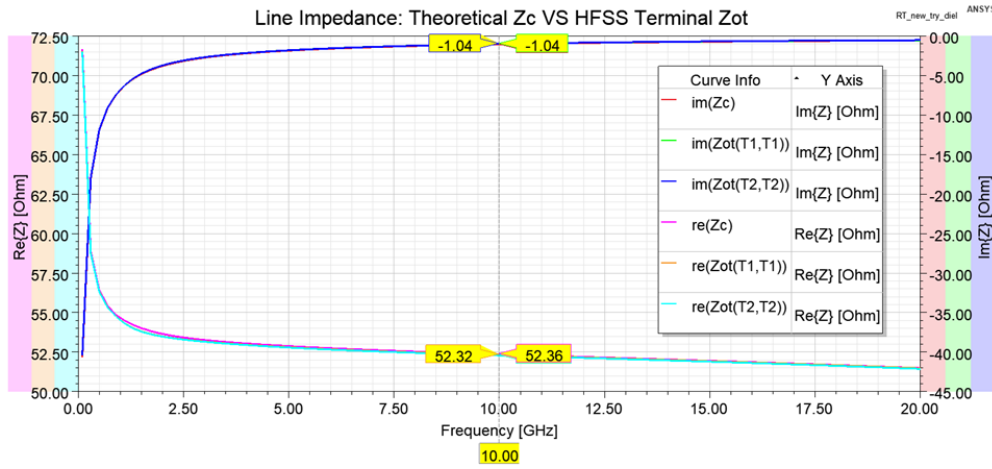


Figure 2.13: Characteristic impedance for the Al On-Insulators CPW

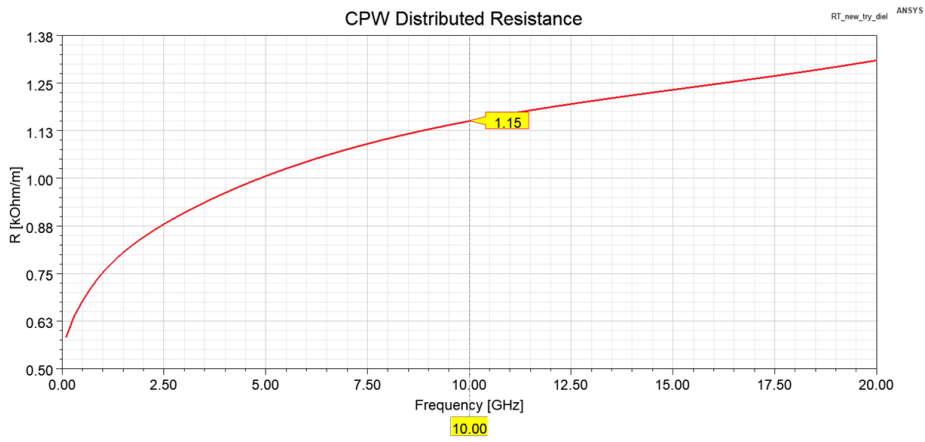
### Extraction of $RLC$ Line Parameters

This particular section will be reserved to the discussion of the extracted distributed line  $RLC$  parameters<sup>10</sup> defined in the framework of transmission line theory (see §2.2). As a matter of fact, by exploiting the  $S$ - $ABCD$  matrices conversion relations reported in appendix §A.4, it is possible to easily find out the values of the characteristic impedance and the propagation constant of the 2 CPW cases. Moreover, recalling from §2.2.1 the mathematical definition of such quantities

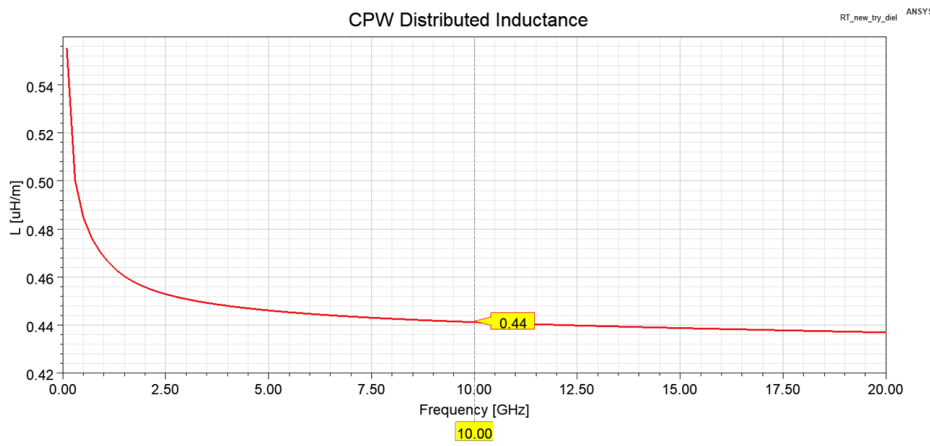
$$\gamma = \sqrt{(\mathcal{R} + j\omega\mathcal{L}) \cdot (\mathcal{G} + j\omega\mathcal{C})}$$

$$Z_C = \sqrt{\frac{\mathcal{R} + j\omega\mathcal{L}}{\mathcal{G} + j\omega\mathcal{C}}}$$

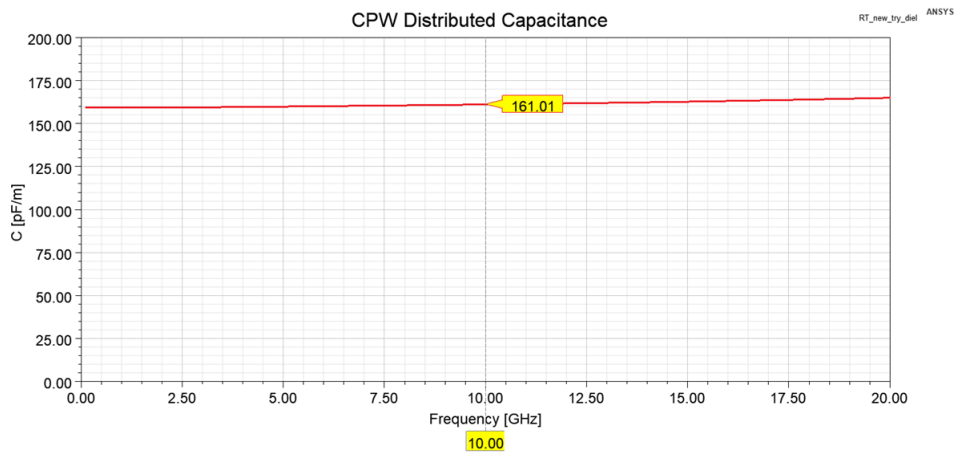
<sup>10</sup>The distributed conductance  $\mathcal{C}$  is not considered since, as explained in [29], its value is expected to be very small over the whole frequency range, making its effect negligible.



(a) Distributed CPWs resistance



(b) Distributed CPWs inductance



(c) Distributed CPWs capacitance

Figure 2.14: CPW distributed *RLC* parameters

as explained in [29], it is possible to extract the values of the *RLC* parameters in the following way:

$$\begin{cases} \mathcal{R} = \Re\{\gamma Z_C\} \\ \mathcal{L} = \Im\{\gamma Z_C\} \\ \mathcal{C} = \Im\{\gamma/Z_C\} \end{cases} \quad (2.3.3.1)$$

In so doing, in Figure 2.14 are reported the behaviours of the distributed parameters for the Al On-Insulators geometry. In particular, it is possible to notice an increase for the resistance with higher and higher frequencies. Such a trend is explained by the well-known skin-effect phenomenon, for which, in AC, the field only propagates through a thin outermost shell of the conducting material. As the frequency increases, such a  $\delta$  layer becomes thinner and thinner, following the relation:

$$\delta_{Al} = \sqrt{\frac{1}{\sigma_{Al}\mu_0\pi f}}$$

In this way, the transversal cross-section in which the current circulates is decreasing, making the line resistance to increase. Even if the Al thickness  $t = 200 \text{ nm}$  is still smaller than the worst case skin depth  $\delta_{Al}(20 \text{ GHz}) \simeq 517,32 \text{ nm}$ , the current distribution inside the line starts to change, accumulating at the outermost edges and acting as a transition phenomenon for the resistance skin-effect-based increase (see [26] and [29]).

On the other hand, as also reported in [28] the inductance is found to reach a stable trend at high frequencies, because of the vanishing of the internal inductance component, due to the current flowing homogeneously inside the conductor, and the predominance of the external inductance component, linked to skin-effect phenomenon. Moreover, since both the distributed resistance and the inductance depend only on the Al line properties, such quantities does not change with respect to the two CPW structures, for which the only difference is represented by the presence of dielectric layers.

According to [29], the capacitance mainly depends only on geometrical CPW parameters and on the dielectric properties of the material surrounding the line: no remarkable variation is therefore, expected along the frequency range. In Figure 2.14(c) it is possible to notice that the capacitance is quite stable all over the frequency range, increasing by an almost 4%, probably due to numerical computation issues.

## 2.4 Conclusion

By means of the previous study, it has been possible to provide a practical example of how transmission line theory can be applied to microwave engineering in order to evaluate the performances of RF components. In particular, such CPW structures are of great interest for silicon CMOS-compatible quantum computing, providing an efficient way to route high-frequency electric signals directly On-Chip, dealing with integrated 1-metal layer interconnects.

### 2.4.1 Achievements

In this chapter it has been possible to apply HF circuit theory to a practical case, by analysing the electromagnetic properties of a coplanar waveguide geometry. Such a study also allowed to evaluate the potentialities that Ansys® HFSS® software can provide for the simulation and modelling of MMIC components.

Without entering the details, a first basic simulation of an Al On-Si CPW has been carried out, understanding how the software works for the correct calculation of electromagnetic properties of the system and allowing to perform an optimization analysis for impedance matching conditions. Later on, the case for an Al On-Insulators line has been studied, applying the acquired knowledges to such a bit trickier configuration, in order to validate the methodology adopted during the previous simulation and analyse a more realistic RF On-Chip routing case. In the end, the obtained results have been processed in order to extract the *RLC* distributed parameters defining the transmission line model of the second CPW geometry: by means of such quantities, it has been possible to estimate the performances of such a structure and provide a simplified electric model.

### 2.4.2 Future Work

Some very few words should be spent, as a last discussion, about the future research activities that have to be set up, starting from such a simulation work. As a matter of fact, many different aspects regarding CPW technology still need to be addressed; for instance, a Spice-compatible model could be implemented, in order to study the system in more abstracted levels and considering its performances in a whole circuit netlist. Moreover, dealing with technological processes, the impact of metallic dummies (for back-end interconnects planarization) on the electromagnetic performances of CPW lines should be seriously investigated, basing on the results obtained in [30]. Finally, such a structure should be fabricated and tested, in order to compare the predictive simulation and modelling results with the real case behaviour of the transmission line.



## Chapter 3

# Electron-Spin Resonance for Coherent Si Spin Qubits Manipulation

### 3.1 Introduction

Since its first discovery in 1944 by the Soviet physicist Yevgeny Zavoisky, Electron Spin Resonance (ESR), usually also named Electron Paramagnetic Resonance, has shown to be an extremely versatile phenomenon, allowing scientists to investigate the properties of materials with unpaired electrons.

Basically, its working principle is identical to Nuclear Magnetic Resonance (NMR),<sup>1</sup> in which the nuclear spin of atoms is generating an electromagnetic signal, when the material is under the exposition of a strong static magnetic field and perturbed by the application of a weaker dynamic field in a near-resonance regime; the only difference between the two phenomena is that the spin to be excited by ESR is the one of electrons. In so doing, ESR has found a huge number of applications in paramagnetic spectroscopy, where it is successfully used to measure the properties of metals and organic free radicals. Nevertheless, in the last decades, with the more and more emerging interest on Quantum Computing technologies, ESR has attained an increasing attention by current research, being finally engineered to provide an accurate and high-fidelity tool for the control and manipulation of systems based on electron spin Qubits (*i.e.* CMOS QDs [31], P-dopants [15] and NV diamond centers [32]).

This chapter will be, therefore, dedicated to the discussion about ESR technologies

---

<sup>1</sup>NMR has found an extraordinary success in medical applications, in particular for diagnosis advanced techniques such as Magnetic Resonance Imaging (MRI) and Magnetic Resonance Microscopy (MRM).

for controlling Si-spin Qubits. In particular, very few words will be first spent about the physical explanation of ESR in terms of quantum information and how it is exploited nowadays for building up spin-controlling systems. Then, the main work about an ESR CPW line design and electromagnetic simulation will be presented, providing a detailed explanation of the procedure to correctly simulate the structure and describing the most relevant results obtained during the first design and the subsequent optimization phases.

## 3.2 Spin Control by ESR Techniques

As it has been already mentioned, thanks to the coupling between electron spin and electromagnetic fields, ESR can be a useful tool for controlling the state of spin-based Qubits. In this section, it will be first reported the origin of this phenomenon in terms of quantum mechanics formalism. Then, a brief review of how ESR-based Qubits control is physically implemented in current technology will be presented.

### 3.2.1 Quantum Mechanics Background

One of the most diffused physical principles for quantum information control and manipulation of Si-spin QDs is Electron Spin Resonance (ESR).<sup>2</sup> Such a phenomenon mainly arises from the presence of an electron (and consequently, its spin) inside a space region in which a static and a dynamic magnetic fields are applied perpendicularly to each others.

The presence of both a static magnetic field, allowing the spin states to be divided into two energetically distinguishable levels (*i.e.* up and down states), and a dynamic one, set in resonance with the precessing frequency of the electron spin, is a key factor for reaching the possibility to coherently convert  $|0\rangle$  and  $|1\rangle$  states each others.

#### Behaviour of Electron Spin under Static $B$ -Fields

First of all, the application of a static  $\mathbf{B}_0(\mathbf{r}) = B_0\hat{\mathbf{z}}$  field, which is crucial for Qubit readout by means of Zeeman energy splitting, also allows the electron spin to precess around the direction of the static field. As a matter of fact, considering a single electron, its spin magnetic moment can be defined as

$$\boldsymbol{\mu} = -\frac{1}{2}g\mu_B\boldsymbol{\sigma}$$

---

<sup>2</sup>Or alternatively, Electric Dipole Spin Resonance (EDSR): in this case, a dynamic electric field is used to manipulate electron spin, basing on spin-orbit coupling for electrons in crystal lattices.



where  $g$  is the dimensionless Dirac relativistic  $g$ -factor (almost equal to 2, for electrons in Si)<sup>3</sup>,  $\mu_B = \frac{e\hbar}{2m_e}$  is the Bohr magneton (being  $e = -1,602 \times 10^{-19} \text{ C}$  and  $m_e = 9,109 \times 10^{-31} \text{ kg}$ , respectively, the electron fundamental charge and free-space mass, while  $\hbar = h/2\pi = 1,054 \times 10^{-34} \text{ J s}$  expresses the reduced Planck constant) and  $\sigma$  defines a dimensionless operator linked to the spin angular moment of the electron:

$$\mathbf{S} = \frac{\hbar}{2}\boldsymbol{\sigma}$$

Moreover, the spatial components of the operator  $\sigma$  are the well-known Pauli matrices, defined as the following quantities:

$$\sigma_x = \begin{pmatrix} 0 & 1 \\ 1 & 0 \end{pmatrix} \quad \sigma_y = \begin{pmatrix} 0 & -j \\ j & 0 \end{pmatrix} \quad \sigma_z = \begin{pmatrix} 1 & 0 \\ 0 & -1 \end{pmatrix} \quad (3.2.1.1)$$

According to [35], the Hamiltonian of the electron can be consequently expressed like

$$H = -\boldsymbol{\mu} \cdot \mathbf{B}_0 = \frac{1}{2}g\mu_B\boldsymbol{\sigma} \cdot \mathbf{B}_0 = \frac{1}{2}\hbar\gamma\boldsymbol{\sigma} \cdot \mathbf{B}_0 = \frac{1}{2}\hbar\gamma\sigma_z B_0 \quad (3.2.1.2)$$

being  $\gamma = \frac{g\mu_B}{\hbar} \simeq 1,761 \times 10^{11} \frac{\text{rad}}{\text{T s}}$  the electron gyromagnetic ratio.

At this point, taking into account a time-dependent quantum state  $|\psi(t)\rangle$ , whose initial state is described by  $|\psi(0)\rangle = \alpha|0\rangle + \beta|1\rangle$  for general  $\alpha$  and  $\beta$  coefficients respecting the normalization relation  $|\alpha|^2 + |\beta|^2 = 1$ , its time evolution can be theoretically calculated by solving the Schrödinger equation:

$$j\hbar \frac{d}{dt} |\psi(t)\rangle = H |\psi(t)\rangle$$

Since the Hamiltonian has no dependency on time, by recalling the propagator formula for the time evolution operator  $U(t)$ , the evolution of the state over a certain elapsing time  $t$  can be solved exactly for

$$|\psi(t)\rangle = U(t) |\psi(0)\rangle = e^{-jHt/\hbar} |\psi(0)\rangle \quad (3.2.1.3)$$

By substituting Equation 3.2.1.2 and the definition of the initial condition state inside Equation 3.2.1.3, it is possible to obtain the following result:

$$\begin{aligned} |\psi(t)\rangle &= e^{-j\gamma B_0 \sigma_z t/2} (\alpha|0\rangle + \beta|1\rangle) \\ &= e^{-j\gamma B_0 t/2} \alpha|0\rangle + e^{j\gamma B_0 t/2} \beta|1\rangle \\ &= \alpha|0\rangle + e^{j\gamma B_0 t} \beta|1\rangle \end{aligned}$$

---

<sup>3</sup>For more information about the Pauli-Dirac relativistic formulation of quantum mechanics, the reader is encouraged to look at [33] and [34].

in which the last equality has been obtained by multiplying the wavefunction by a global phase  $\exp(-j\gamma B_0 t/2)$ , whose effect has no influence on the definition of the quantum state (as explained in §1.1.2). Furthermore, it has been also exploited the property of the matrix  $\sigma_z$ , as reported in [36],<sup>4</sup> for which

$$e^{j\alpha\sigma_z} = I \cos \alpha + j\sigma_z \sin \alpha = \begin{pmatrix} e^{j\alpha} & 0 \\ 0 & e^{-j\alpha} \end{pmatrix} \quad (3.2.1.4)$$

Remembering now that a Qubit state can be represented on the Bloch sphere as  $|\psi\rangle = \cos \theta/2 |0\rangle + \exp(j\phi) \sin \theta/2 |1\rangle$ , where the local phase is evolving like  $\phi(t) = \gamma B_0 t$ , it means that the electron spin is rotating around the static field direction with a frequency  $\omega_L = \gamma B_0$ , known as Larmor frequency.

### Behaviour of Electron Spin under Dynamic B-Fields

Following the same strategy as the one presented in §3.2.1, but having the ruse to apply some mathematical simplifications to the more tedious calculation, it is possible to study the case in which an oscillating magnetic field  $\mathbf{B}_1(\mathbf{r}, t) = B_1 \cos(\omega t)\hat{\mathbf{x}}$  is applied perpendicularly to the direction of the static field  $\mathbf{B}_0(\mathbf{r}) = B_0\hat{\mathbf{z}}$ .

In so doing, the Hamiltonian of this new system can be derived to be:

$$H(\mathbf{r}, t) = \frac{1}{2}\hbar\gamma(\sigma_z B_0 + \sigma_x B_1 \cos(\omega t))$$

The full procedure for getting the final result is reported in appendix §B.1.

It is important to highlight the fact that, if the dynamic field is set to oscillate at the precise Larmor frequency (inducing, therefore, a resonance condition), then, in the z-rotating framework, the Hamiltonian of the electron can be found to be

$$H'(t) = H' = \frac{1}{2}\hbar\gamma\sigma_x B_1$$

which is essentially time-independent. By means of the same argument explained in §3.2.1, this result implies that the application of the dynamic magnetic field induces a further precession of the spin around the x-axis at a frequency  $\omega_R = \gamma B_1/2$ , known as Rabi frequency.

In the end, this brief quantum mechanical explanation of ESR allows to understand how the combined application of a static  $\mathbf{B}_0(\mathbf{r})$  and a dynamic  $\mathbf{B}_1(\mathbf{r}, t)$  magnetic fields results in a whole spin flip. As described in Figure 3.1, the simultaneous precession of the spin around two normal axes is actually able to perform a spin-up/spin-down conversion: by controlling the finite duration of the Rabi-oscillating microwave burst

---

<sup>4</sup>In particular, the exponential of Pauli matrix for a generic  $\hat{\mathbf{n}}$  dimension vector can be generally expressed as  $e^{j\alpha(\hat{\mathbf{n}}\cdot\hat{\boldsymbol{\sigma}})} = I \cos \alpha + j(\hat{\mathbf{n}}\cdot\hat{\boldsymbol{\sigma}}) \sin \alpha$ , being  $I$  the 2x2 identity matrix.

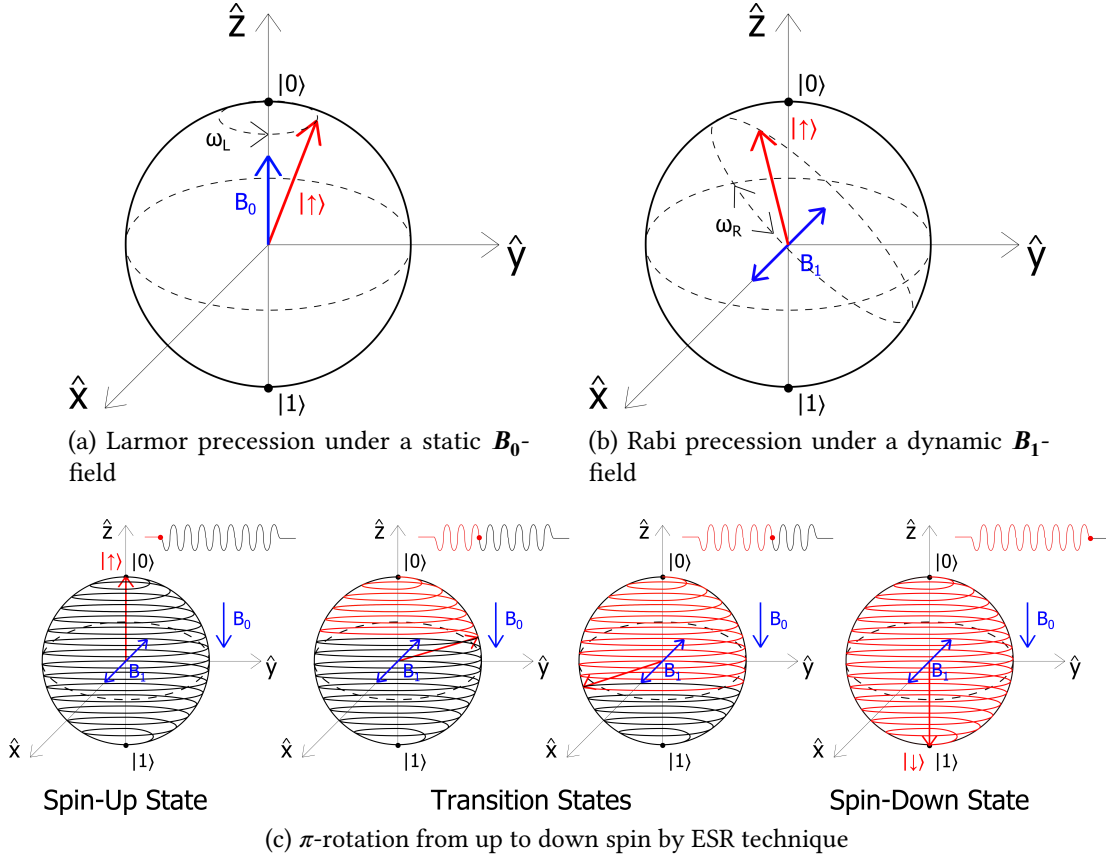


Figure 3.1: Graphical description of ESR spin manipulation mechanisms

pulse, it is therefore possible to perform coherent control of the electron spin, as reported in [37] and [38]. Moreover, ESR can also become a powerful tool for limiting quantum decoherence: exploiting the continuous conversion between up and down states offered by multiple  $\pi$ -rotations, as reported in [39], such a technique, known as spin-echo manipulation, has been actually one of the major key factors for pushing the limits of coherence time for Si-spin Qubits up to milliseconds.

### 3.2.2 Spin Qubits Manipulation: Practical Implementations

As it has been previously discussed in §3.2.1, spin control and manipulation play an essential role in QC, especially for what it concerns the implementation of quantum logic gates. As a matter of fact, such a technique for manipulating spin works very well for  $\pi$  and  $\pi/2$ -rotations, enabling the possibility to realize 2-Qubit operations, such as *CNOT* (see [40]).

In the following, an alternative approach to ESR will be briefly discussed in terms of physical concepts, while, in the subsequent paragraph, some of the many engineering

approaches for implementing spin control mechanisms will be presented.

### Electric Dipole Spin Resonance

Even if Electron-Spin Resonance is the main tool used nowadays for locally addressing spin Qubit, Electric Dipole Spin Resonance (EDSR) is gradually becoming a valid alternative for electron spin manipulation. First reported by the physicist Emmanuel I. Rashba in 1960, EDSR works on the same principle as ESR: however, in this case, the control of electron spin is not performed by means of magnetic fields, but recurring to dynamic electric fields.

The key factor for such a technique is based on electron spin-orbit coupling in solid lattices: as matter of fact, when electrons move in a solid, in a region in which an electric field gradient is applied, because of relativistic effects, they experience the application of an effective magnetic field.

In other words, if describing the Hamiltonian of an electron moving inside a crystal (*i.e.* silicon) by recurring to a wave packet, whose waves have a wavenumber  $\mathbf{k}$  inside the first Brillouin-zone, it is possible to demonstrate (see [41]) that the crystal momentum defining its motion in a semi-classical way is given by

$$\mathbf{p}(\mathbf{r}, t) = \hbar\mathbf{k} - \frac{e}{c}\mathbf{A}(\mathbf{r}, t)$$

being  $c = 2,998 \times 10^8$  m/s the speed of light in vacuum and  $\mathbf{A}(\mathbf{r}, t)$  the magnetic vector potential, defined in the framework of electrodynamics for  $\mathbf{B}(\mathbf{r}, t) = \nabla \times \mathbf{A}(\mathbf{r}, t)$ .

Since also the electric field can be rewritten in terms of the magnetic vector potential  $\mathbf{A}(\mathbf{r}, t)$  and the electrostatic potential  $\phi(\mathbf{r}, t)$  as

$$\mathbf{E}(\mathbf{r}, t) = -\nabla\phi(\mathbf{r}, t) - \frac{\partial\mathbf{A}(\mathbf{r}, t)}{\partial t}$$

the semi-classical Hamiltonian of the moving electron  $H = \frac{p^2}{2m^*} - e\phi(\mathbf{r}, t)$  (where  $m^*$  is the electron effective mass inside the lattice) is therefore governed by a term depending on the externally applied electric field. Recurring to Lorentz relativistic transformations, it is possible to demonstrate that the electron mainly feels the action of an effective magnetic field in its reference framework, finally originating a magnetic momentum able to couple the electric field to its spin, as first discussed in §3.2.1.<sup>5</sup>

### ESR and EDSR State of the Art for QC Applications

ESR and EDSR represent nowadays the most promising candidates for the implementation of control lines on Si spin-based Qubits systems. Such integrated structures are

---

<sup>5</sup>A discussion about the relativistic formulation of electromagnetism is beyond the scope of this work; for more information about Lorentz transformations and the semi-classical description of electron motion inside a crystal, the reader is invited to refer to [33].

essentially nanoscale RF fields emitter, whose electrical control enables the manipulation of electron spin, respectively, by means of oscillating  $B$  or  $E$ -fields.

Even if in the following chapters it will be mainly discussed about the study of ESR-based structures, it is important to present also the current state of the art of both techniques, highlighting their respective advantages, as well as the complementary drawbacks.

Electron-Spin Resonance, as reported in [42], has been historically the first technique exploited for addressing single electron coherent spin control in QDs. In particular, up to now, many different implementations of ESR lines have been proposed, dealing with coplanar striplines (see [42]), as well as CPW discussed in Chapter 2 (see [43]). By making an AC electric current circulating through a short-circuited line, it is, actually, possible to generate an oscillating microwave magnetic pulse allowing to precisely control the spin state of a single electron in QDs or donor dopant atoms. In Figure 3.2 it is reported an example of ESR antenna implemented by means of coplanar integrated transmission lines.

However, one of the main disadvantages of ESR lines is the difficulty to design a large-scale integrated system for properly controlling many Qubits in singular ways, because of the engineering challenges for harnessing  $B$ -fields in silicon substrates. Such a problem especially concerns nanoscale devices, such as QDs or nanowires, for which it is difficult to individually address single spins (sufficiently close to each other for enabling entanglement mechanisms) by means of different magnetic pulses.

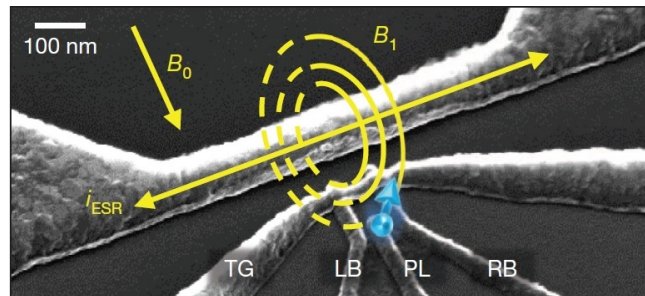


Figure 3.2: SEM picture of spin control shorted ESR line [15]

On the other hand, even if much more complex in terms of physical behaviour, recent EDSR techniques can become a valid alternative to ESR: as a matter of fact,  $E$ -fields are well routed in current VLSI CMOS-based technology and offer, therefore, a versatile tool for manipulating many correlated spins. In particular, Electric Dipole Spin Resonance could be engineered by exploiting the same coplanar technology as ESR, but, in this case, an open-circuit must be created at the end of the transmission line, in order to achieve a larger oscillating electric field, as reported in [44]. Moreover, another interesting implementation, discussed in [18], deals with gating structures for both confining single electrons on nanowire QDs and providing the electrical control for EDSR spin manipulation.

Unfortunately, such a spin-orbit coupling is extremely weak in silicon lattice. In order to enhance its effectiveness, many approaches have been proposed so far, exploiting hole spin-valley coupling, recurring to nuclear spin control or dealing with the use of micromagnets to generate local  $B$ -fields (see respectively [18], [44] and [45]).

### 3.3 Simulation of a CPW Broadband ESR Line

As reported in §3.2.2, ESR lines must be designed to be able to address single Qubits, in order to process spin manipulation for the implementation of quantum gates. In this section, it will be first reported the adopted procedure for simulating an ESR line designed in terms of coplanar waveguides; then, the main simulation results will be described for both a preliminary structure comprising a CPW-line directly on Si and a final version, in which the ESR line is post-processed on a dielectric-based passivation layer.

#### 3.3.1 Physical Specifications

Since the extremely fragile nature of spin quantum states, limited by decoherence times, working conditions for QC operations typically require cryogenic temperatures (*i.e.* in the order of few  $mK$ ): the design of ESR line is, therefore, subjected to particular specifications, in order to realize a structure which could effectively address single spin QDs manipulation. As a matter of fact, the line should be able to generate a sufficiently high oscillating magnetic field  $B_1$  over a wide range of frequencies, in order to operate different 1-Qubit operations, exploiting ESR spin rotations (see [43]).

##### $B_1$ Larmor Oscillating Field

First of all, in order to distinguish spin orientations in Si QDs, a static magnetic field  $B_0$  must be externally applied: in particular, its amplitude should be sufficient for overcoming thermal energy fluctuations  $\Delta E_T \simeq 5k_B T$ , being  $k_B = 1,381 \times 10^{-23} J/K$  the Boltzmann constant and  $T$  the absolute temperature in the Qubit location. As a matter of fact, thanks to Zeeman effect (see [36]), the spin-splitting energy is given by  $E_Z = \hbar\gamma B_0$ , whose value should be greater than

$$E_Z > \Delta E_T \Rightarrow B_0 > \frac{5k_B T}{\hbar\gamma}$$

Moreover, in order to exploit ESR phenomenon, it is also important to set the frequency of the dynamic  $B_1$  to be precisely at the Larmor resonance condition (as described in §3.2.1). In so doing, such a frequency should be:

$$f_1 = \frac{E_Z}{h} = \frac{\gamma B_0}{2\pi}$$

For instance, at  $T \simeq 10 \text{ mK}$ , the amplitude of the static magnetic field must be  $B_0 > 37,17 \text{ mT}$ , while the minimum ESR line deliverable frequency of the oscillating field has to be  $f_1 \simeq 1,04 \text{ GHz}$ , which gives the  $\text{GHz}$  order of magnitude for cryogenic ESR resonance frequencies.

### **$B_1$ -Field Amplitude for Rabi Oscillations**

As described in [43], the time an electron spin necessitates for undergoing a complete up-down conversion (*i.e.* a  $\pi$ -rotation) is defined for  $t_\pi = \frac{2\pi}{2\gamma B_1}$ , essentially depending on the amplitude of the oscillating magnetic field. In order to provide a coherent spin control mechanism, such a rotation time must be shorter than the dephasing time  $T_2^*$  (in [16], it is reported to have measured  $T_2^* \simeq 60 \text{ ns}$  in Si). In so doing, it is necessary to provide a dynamic field  $B_1 > 0,30 \text{ mT}$ .

### **$E_1$ -Field Amplitude for Readout Operations**

On the other hand, also the electric field generated by the ESR microwave antenna must be taken into account. As a matter of fact, as reported in [42], such an  $E_1$ -field could be able to couple to electrons in QDs via emission of photons, enabling tunnelling mechanisms which could possibly discharge the charge-sensing readout apparatus and contribute to an over-heating, due to larger current circulation in the SET nanowire. In such conditions, the electric field must be essentially minimized, while the magnetic field must be maximized at the QDs location: this is the reason why the nano-antenna is basically designed to behave like a short-circuit.

In Table 3.1, the specifications for implementing a correctly working ESR line are briefly summarised.

Field	Magnitude	Operating Frequency
$B_0$	$> 37,17 \text{ mT}$	static field
$B_1$	$> 0,30 \text{ mT}$	$> 1,04 \text{ GHz}$
$E_1$	as low as possible	$> 1,04 \text{ GHz}$

Table 3.1: Field specifications for the design of an On-SI ESR antenna at  $10 \text{ mK}$

### **3.3.2 CPW-based ESR Line Geometry**

The ESR structure simulated in this work basically consists of an aluminium CPW line terminated on both the signal-to-ground sides by means of a nano-antenna (*i.e.* two short-circuits connecting the signal line both to the right and left ground lines) placed in the surroundings of the Qubit QDs. Such a geometry, illustrated in 3.3, is very similar to one of the designs proposed in [43]: in this work, however, for the sake of simplicity,

only the On-Chip ESR has been simulated,<sup>6</sup> without considering QDs SET and gating structures.

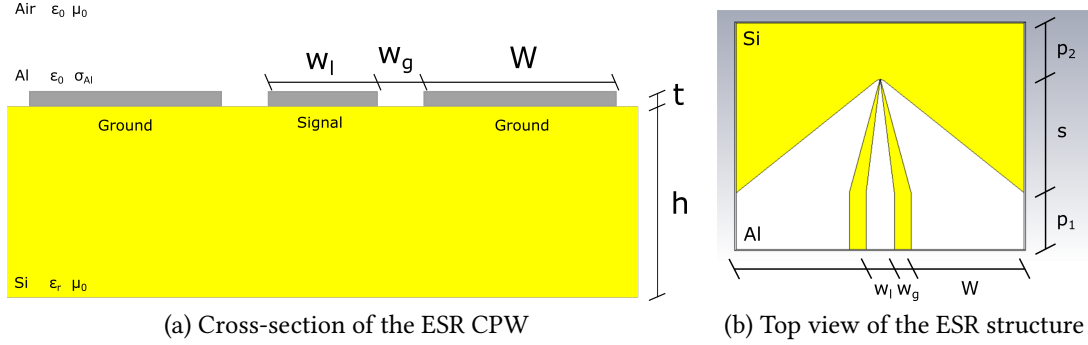


Figure 3.3: Geometry of the simulated CPW-based ESR control line

In particular, such a configuration is found to be a promising candidate for the implementation of an integrated ESR line for the following reasons:

- Relying only on CPW technology, it preserves the same propagating modes of the PCB coplanar waveguides connecting the cryogenic chip to control electronics stacks at higher temperatures.
- It presents, therefore, a quite large range of propagating frequencies, introducing a very small amount of mismatching losses.
- It allows to generate a very stable broadband magnetic field at the two shorts locations.
- Since the signal is split in two different branches at the antenna termination, it provides a reduced  $E$ -field at the QDs location, with respect to other designs relying on coplanar striplines (see [43]).

### Overall CPW Dimensions

In Table 3.2 are reported the values for the preliminary CPW On-Si ESR line design: in particular, the signal line width is set up to be  $w_l = 250 \mu m$ , in order to be consistent with the previous study of coplanar waveguides reported in §2.2.1, while  $w_g \simeq 148 \mu m$  is first optimized for obtaining a  $52 \Omega$  impedance match at  $10 GHz$  (see appendix §B.2.2).

<sup>6</sup>The simulation of the ESR line has been carried out by means of CST Studio Suite<sup>®</sup> by Dassault Systèmes<sup>®</sup>: such a software has been preferred to Ansys<sup>®</sup> HFSS<sup>®</sup> essentially because it allows to better deal with the mm-to-nm scale of the ESR structure and it is able to compute and display the values of the  $E$  and  $B$ -fields inside a solid with higher accuracies. For more information, visit <https://www.3ds.com/products-services/simulia/products/cst-studio-suite/>.



Dimension	Value	Geometrical Meaning
$w_l$	$250 \mu\text{m}$	Signal Line Width
$w_g$	$148 \mu\text{m}$	Gap Width
$W$	$1 \text{ mm}$	Ground Lines Width
$t$	$100 \text{ nm}$	CPW Thickness
$h$	$775 \mu\text{m}$	Substrate Thickness
$p_1$	$500 \mu\text{m}$	CPW Length
$s$	$1 \text{ mm}$	Transition Line Length
$p_2$	$500 \mu\text{m}$	Above Nanoantenna Region Length

Table 3.2: Geometrical dimensions for the overall CPW-based ESR line

### ESR Short-Line Dimensions

Since the microwave antenna is characterized by nanoscale dimensions, Figure 3.4 presents a zoom of the ESR structure in the surroundings of the short-circuit, while Table 3.3 sums up the values of geometrical features describing the antenna. Such values are chosen to be similar to [43], in order to obtain a first result check for this preliminary version of the control line.

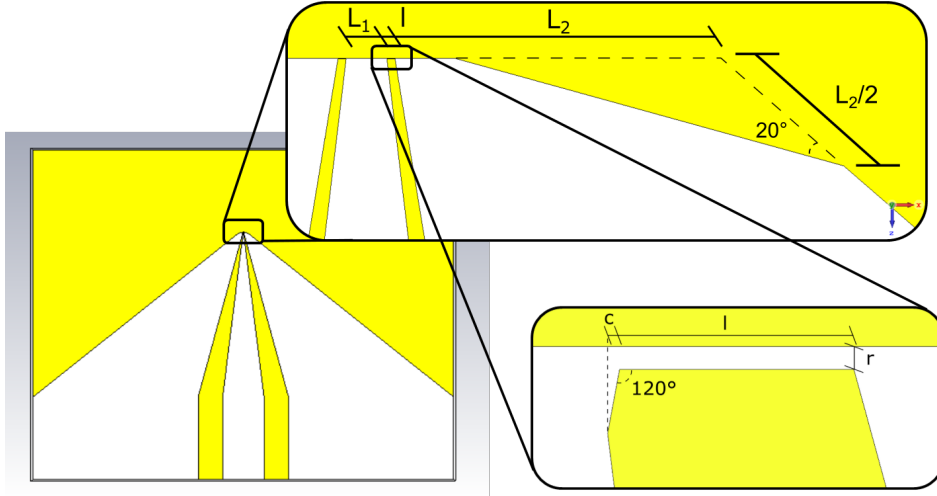


Figure 3.4: Zoomed top view of the ESR nano-antenna

### 3.3.3 Simulation Results of an Al CPW On-Si ESR Line

Since the simulation setup is similar to the one previously mentioned for the analysis of the CPW transmission line in §2.3.1, the whole discussion will be only reported in appendix §B.2, for the sake of completeness. It is, therefore, possible to run CST®

Dimension	Value	Geometrical Meaning
$L_1$	$2,5 \mu\text{m}$	Short-Signal Line Width
$l$	$500 \text{ nm}$	Short Length
$L_2$	$20 \mu\text{m}$	Short-Ground Lines Width
$c$	$50 \text{ nm}$	Symmetry Angle Base
$r$	$50 \text{ nm}$	Short Width

Table 3.3: Geometrical dimensions for the ESR nano-antenna

Frequency solver over a broadband [100 MHz; 60 GHz] range. In particular, for this preliminary configuration, the waveguide port is excited with an injected power  $P_{in} = 1 \text{ mW} = 0 \text{ dBm}$ , as it is explained in [43], in order to have a quantitative comparison for the simulation results.<sup>7</sup>

### Port Information

First of all it is possible to analyse the waveguide port results. In particular, Figure 3.5 clearly confirms that the structure has been correctly designed for a single Quasi-TEM propagation mode: at 10 GHz, the impedance line is approximately  $Z_{port} \simeq 52 \Omega$ , validating the results discussed in appendix §B.3.

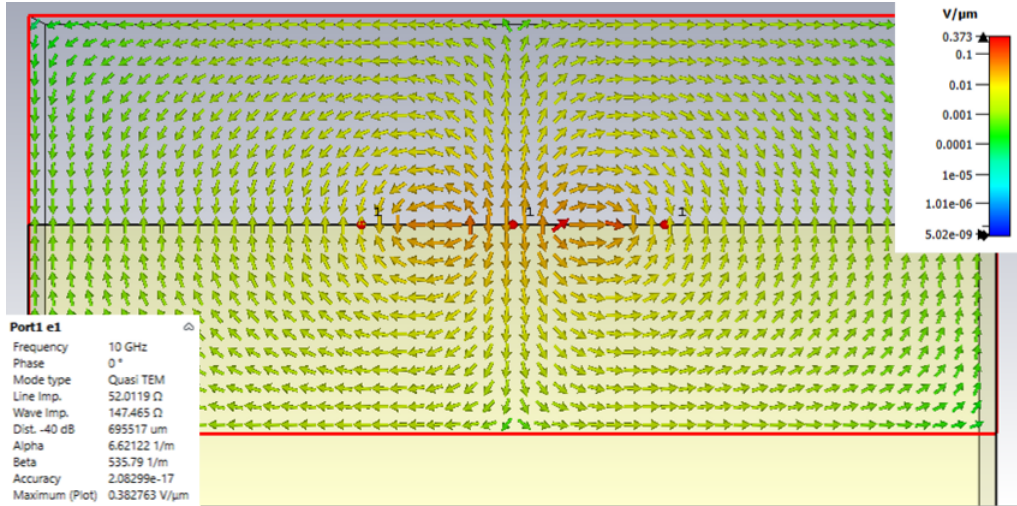
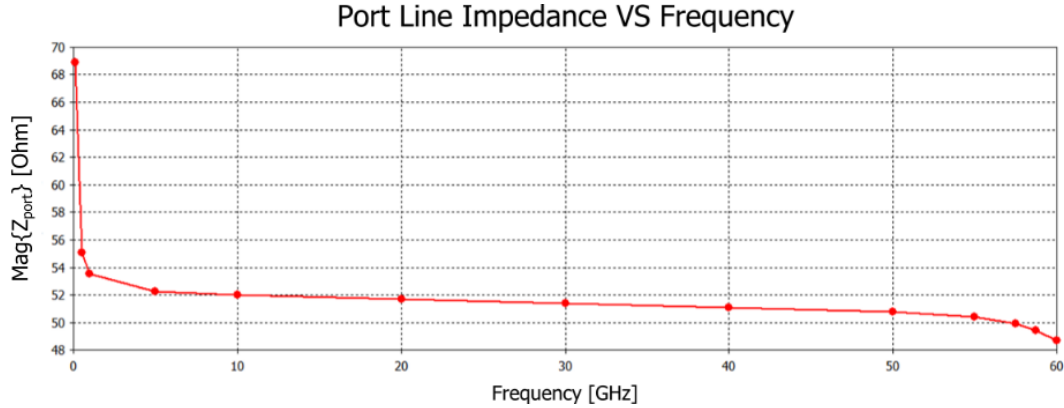


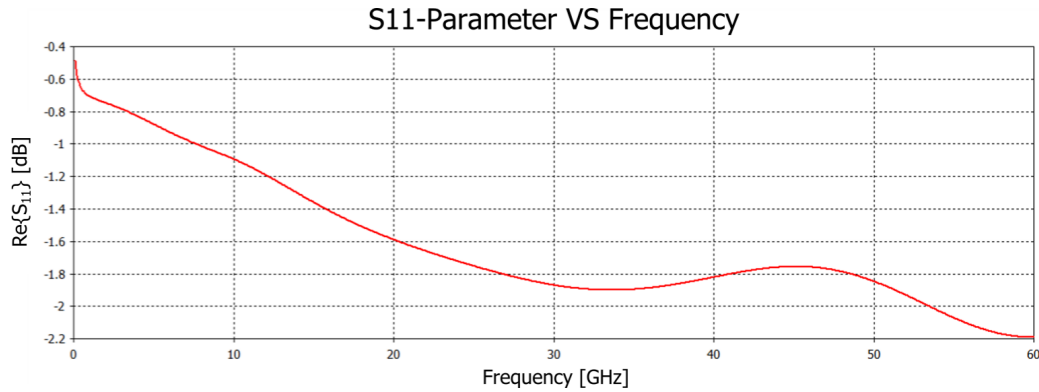
Figure 3.5: ESR line Quasi-TEM electric field port cross-section at 10 GHz

<sup>7</sup>Such a power is probably too high for the control of QDs, because it can both be a relevant source of dissipation (and, therefore, it can contribute to the heating of the quantum chip) and cause the physical melting of the fabricated ESR antenna, as reported in [44].

More precisely, the behaviour of the line impedance is reported in Figure 3.6(a): in the ESR frequency range, between  $1\text{ GHz}$  and  $60\text{ GHz}$ ,  $Z_{port}$  changes in  $+2,9\%$  and  $-6,3\%$  with respect to the  $52\ \Omega$  nominal value at  $10\text{ GHz}$ , providing an acceptably stable impedance match all over the interest broadband.



(a) ESR line impedance at the waveguide port



(b) ESR line  $S_{11}$  scattering parameter

Figure 3.6: ESR line port information over the simulated frequency range

On the other hand, in Figure 3.6(b) it is plotted the behaviour of the scattering parameter  $S_{11}$ : as it is possible to notice, the reflection parameter presents an almost linear behaviour,<sup>8</sup> dissipating more and more energy as the frequency increases and reaching a minimum of nearly  $-2,2\text{ dB}$  at  $60\text{ GHz}$ , in agreement with what is reported in [43].

<sup>8</sup>In §3.3.4, several geometrical sweeps will be performed in order to increase as much as possible the  $S_{11}$ -parameter, in order to reduce losses and eliminate resonance phenomena (*i.e.* the bumps present in Figure 3.6(b)).

## *E* and *B*-Fields

Dealing with the propagation of electric and magnetic fields all over the structure, the simulated ESR line will generate a *B*-field which will be maximum at the ESR antenna location, being the antenna essentially a short-circuit. On the contrary, the *E*-field is expected to be mainly located inside the signal-grounds gap, in particular, at the outermost conducting edges of the line. Figure 3.7 respectively shows the behaviour of the two fields on the top 2D plane of the structure at the Si-air interface.<sup>9</sup> Such results, for an injected power of  $0\text{ dBm}$ , are qualitatively similar with respect to the ones reported in [43], since it is possible to notice the predicted distribution of the fields: however, a quantitative comparison is not possible because of the different geometry and the different way of defining the Al line.

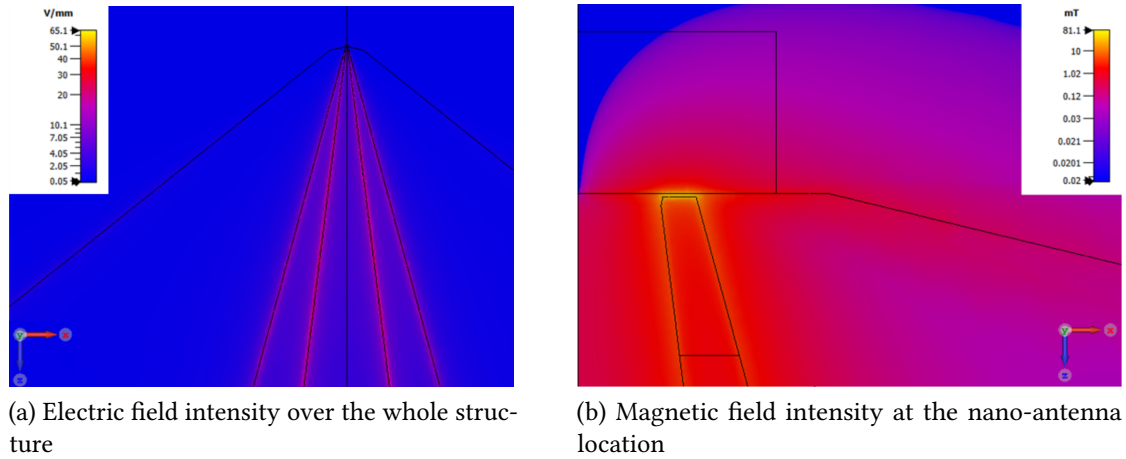


Figure 3.7: 2D top view of *E* and *B*-fields over the ESR line at  $50\text{ GHz}$  ( $P_{in} = 0\text{ dBm}$ )

Inserting some probes in close proximity to the nano-antenna, where the P-dopant atoms discussed in [43] should be located, nearly  $100\text{ nm}$  deep inside the Si substrate (as depicted in Figure 3.8(a)), it is also possible to have a look on the behaviour of the fields all along the frequency range. As shown in Figure 3.8(b) and (c), the *B*-field is quite constant all along the simulated range: considering, for example, the rightmost probe above the line, the magnitude of the magnetic field nearly reaches a value of  $7\text{ mT}$ . On the other hand, the *E*-field shows values comprised between  $12\text{ kV/m}$  and  $3\text{ kV/m}$ , with a minimum case of almost  $4\text{ kV/m}$  for the rightmost above probe.

<sup>9</sup>It is important to notice that CST<sup>®</sup> Microwave Studio provides AC values according to the peak-to-peak convention: in order to get Root-Mean-Square results, one should convert the generic *A* quantity as  $A_{RMS} = 0,353A_{pp}$ .

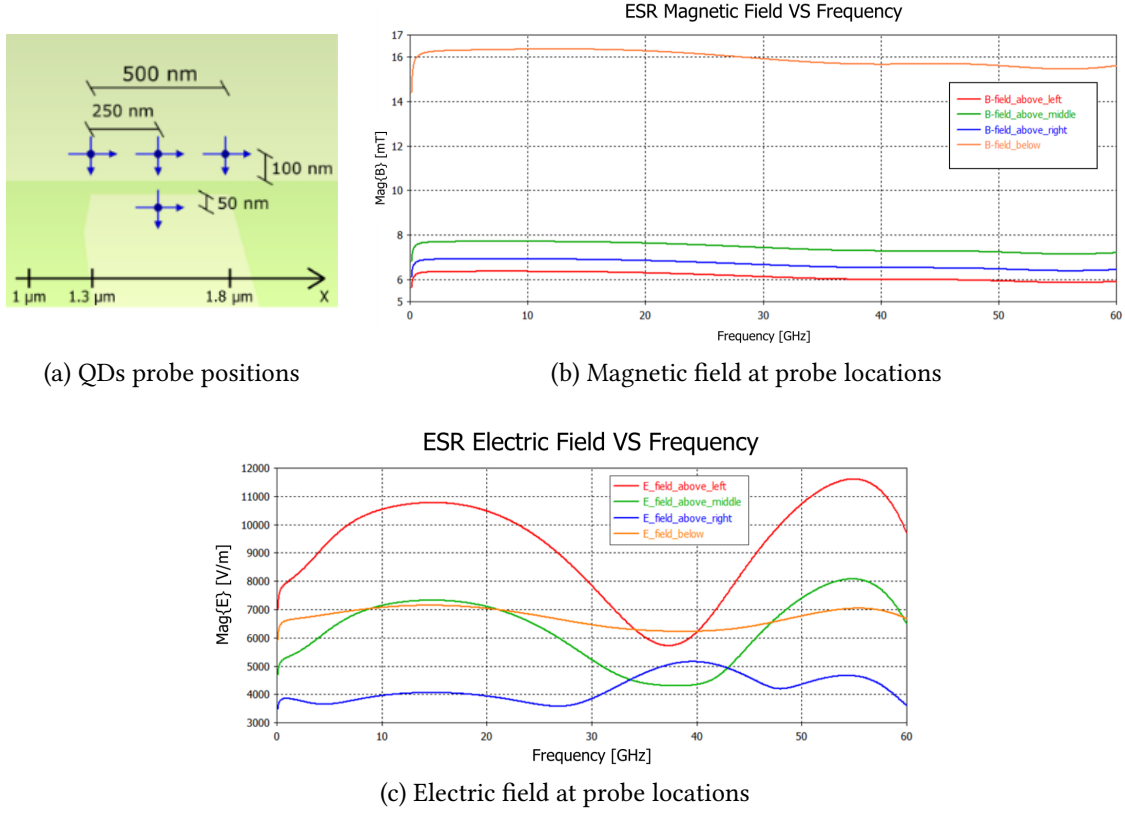


Figure 3.8:  $B$  and  $E$ -fields all along the frequency range for each probe ( $P_{in} = 0 \text{ dBm}$ )

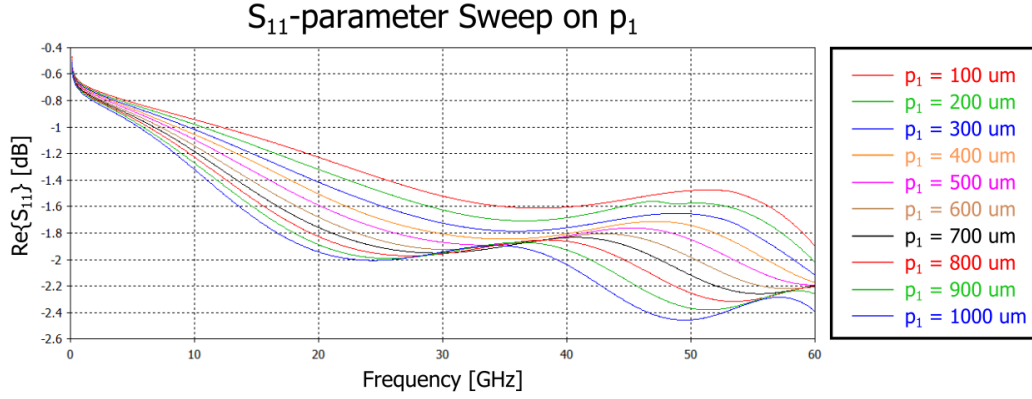
### 3.3.4 Optimization Results of an Al On-Si ESR Line

In order to reduce losses all along the line, maximize the  $B$ -field and minimize the  $E$ -field in correspondence of QDs location, it is necessary to modify the proposed structure by optimizing its geometrical parameters. To do so, a series of sweep analyses are performed on many crucial geometrical features of the ESR structure.

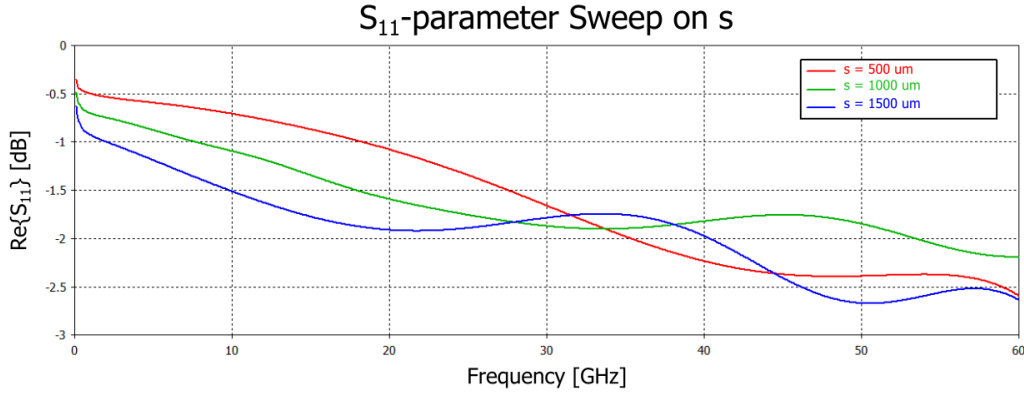
#### $S$ -Parameter Optimization

First, losses, and therefore power dissipation, can be reduced by increasing the value of the  $S$ -parameter, which basically defines the amount of the return signal which is collected back at the 1-port interface: for an ESR shorted antenna, such a value is expected to be almost  $0 \text{ dB}$ , meaning that all the injected power is coming back at the port location. To do so, mainly two sweeps on  $p_1$  and  $s$  are performed, without modifying the cross-section geometry of the line.

Figure 3.9 presents the results for the sweep analyses on  $p_1$  and  $s$ . It is possible to clearly see that, in both cases,  $S_{11}$  behaviour is subject to vertical shifts: such a situation



(a) Sweep analysis on  $p_1$ , for  $S_{11}$



(b) Sweep analysis on  $s$ , for  $S_{11}$

Figure 3.9: Influence of the transmission line length on power dissipation

can be easily explained by recalling that the ESR structure basically acts as a transmission line, whose resistance increases when increasing the length of the line, increasing power dissipation and, consequently, shifting downward the  $S$ -parameter. Moreover also line inductance and capacitance will increase, shifting leftward the position of the first resonance condition and introducing more and more bumps in the frequency range, explaining the horizontal shifts of the  $S$ -parameter.

In particular, the basic optimization for improving the ESR performances is mainly achieved by shortening as much as possible the length of the transmission line: as a matter of fact, also the first CPW line length can be reduced, following the same argument previously discussed.<sup>10</sup>

<sup>10</sup>In practice, in order to make the ESR line design as compact as possible, also a  $W$  ground signal width decrease should be adopted.

### Fields Optimization on QDs Location

In a second time, it is also possible to proceed to an optimization of the short-circuit geometry, in order to maximize the  $B$ -field and minimize the  $E$ -field in the proximity of Qubits. Such a goal is realized by analysing the results of many parametric sweeps for the nano-antenna dimensions (see Figure 3.10(a)): in particular, the fields are measured on the  $x$ -axis parallel to the nano-antenna, 100 nm above this latter, as shown in Figure 3.10(b).

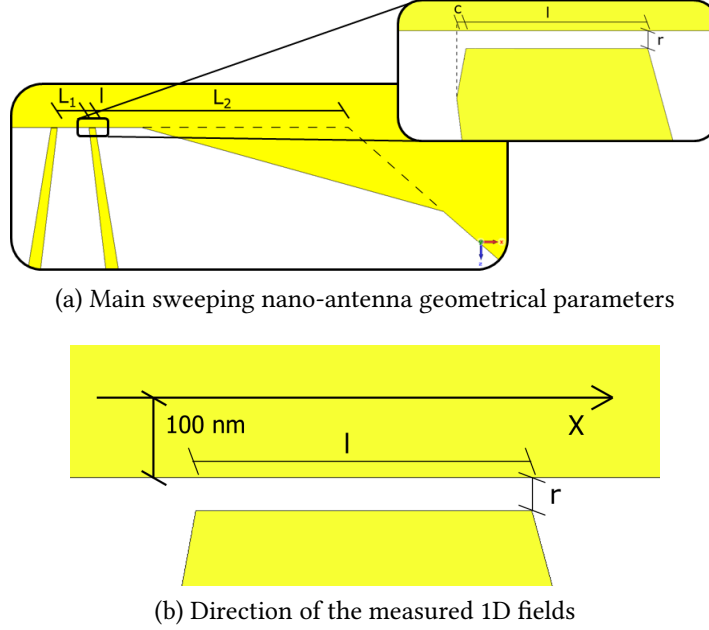


Figure 3.10: Zoom on the shorted microwave antenna for field optimization

Without entering too much into the details, it is at least important to qualitatively describe the meaning of the reported sweeping behaviours:

- **$l$  sweep:** for an increase in the length of the antenna, the magnetic field is found to increase up to a converging value. Such a situation is well predicted when a constant magnetic field is generated by a stationary current circulating in a finite-length wire, resulting in the constant Biot-Savart law for sufficiently long wires, as formulated in the following:

$$B(R) = \frac{\mu_0 I}{4\pi R} \cdot \left[ \sin \left( \arctan \left( \frac{x_1}{R} \right) \right) + \sin \left( \arctan \left( \frac{x_2}{R} \right) \right) \right] \xrightarrow{x_1, x_2 \rightarrow \infty} \frac{\mu_0 I}{2\pi R}$$

being  $I$  the current circulating inside the wire,  $R$  the distance of the point from the center of the wire,  $x_1$  and  $x_2$  its distance, respectively, from the rightmost and leftmost ends of the wire. In reality, Biot-Savart law is quantitatively valid only for  $B$ -fields generated by DC currents: however, in first approximation, considering the current circulating at the center of the antenna, since the minimum wavelength

of the short AC current is  $\lambda_{min} \simeq 5 \text{ mm}$ , it is possible to consider a quasi stationary condition for the AC current oscillating all along the short.

On the other hand, also the electric field seems to increase along the antenna for an increasing length, because of the short resistance growing (see Figure 3.11);

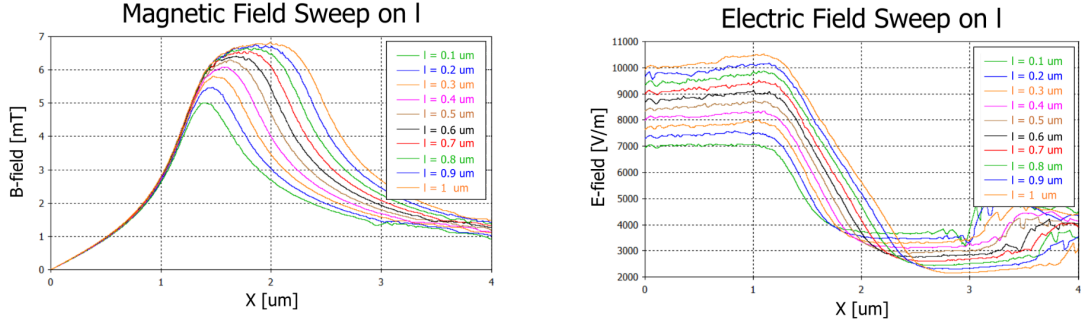


Figure 3.11: Sweep analysis on  $l$ , for  $B$  and  $E$ -fields ( $P_{in} = 0 \text{ dBm}$ )

- $L_1$  sweep: when enlarging the signal line width at the ESR antenna, the same current will circulate inside the short, but the same voltage will drop over a larger conductor, making the  $E$ -field to decrease along the line (see Figure 3.12);

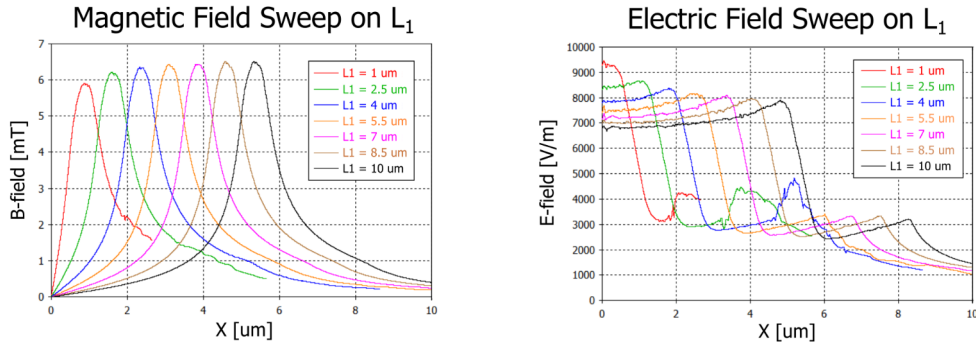
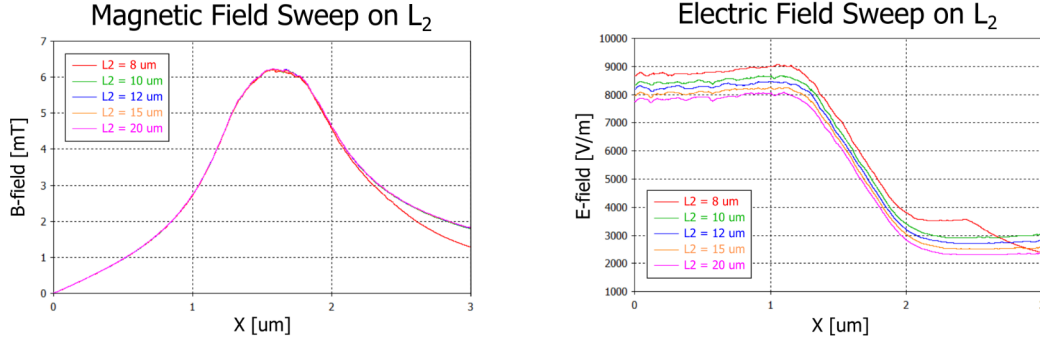


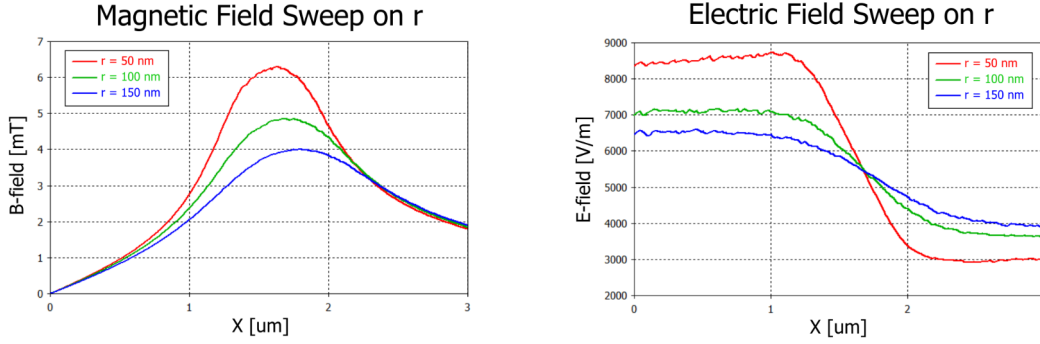
Figure 3.12: Sweep analysis on  $L_1$ , for  $B$  and  $E$ -fields ( $P_{in} = 0 \text{ dBm}$ )

- $L_2$  sweep: the same situation happens also for an increasing of the ground lines width at the short location, making  $B$ -field essentially unchanged, but lowering the value of the electric field (see Figure 3.13);
- $r$  sweep: as reported in Figure 3.14, the magnetic field is expected to decrease as the short width is increased, since the probes are placed further and further from the center of the antenna; however, the  $1/R$  relation provided by Biot-Savart law is not valid, as it is possible to notice from the peak values of the field (see Table 3.4), meaning that a more accurate model is needed for the quantitative prediction of




 Figure 3.13: Sweep analysis on  $L_2$ , for  $B$  and  $E$ -fields ( $P_{in} = 0 \text{ dBm}$ )

such a phenomenon. On the other hand, the electric field is found to stabilize because of the decrease of the antenna resistance.


 Figure 3.14: Sweep analysis on  $r$ , for  $B$  and  $E$ -fields ( $P_{in} = 0 \text{ dBm}$ )

$r$	50 nm	100 nm	150 nm
$B$ -field	6,2 mT	4,9 mT	4 mT

 Table 3.4: Maximum  $B$ -field VS antenna width  $r$ 

Summing up, except for the short width  $r$ ,<sup>11</sup> the fields can be optimized at the QDs locations basically by increasing the sweeping parameters without exceeding too much. As a matter of fact, the ESR should be still sufficiently small in order to properly address single Qubit coherent control at the nanoscale.

<sup>11</sup> $r$  should be actually decreased as much as possible, but not indefinitely, as the current density would increase very quickly, inducing an overheating of the antenna, which could even melt it (see [44]).

### 3.3.5 Simulation Results for an Al On-Insulators ESR Line

Once having run optimization sweeps for improving the performances of the ESR line in terms of impedance match losses and field intensities, it is possible to proceed with the analysis of a more realistic situation. As already explained in §2.3.3, RF structures are, actually, realized On-Chip during back-end fabrication phases: in so doing, many dielectric layers are necessary for the passivation of the front-end stack, in which silicon QDs are fabricated.

#### Geometry and S-Parameter

The geometry of the structure is essentially the one already presented in §3.3.2. However, in this case, the QDs CMOS based Qubits are buried inside an equivalent dielectric layer<sup>12</sup> placed on a  $SiO_2$  BOX: the thickness of the two layers is respectively  $h_1 = 170\text{ nm}$  and  $h_2 = 145\text{ nm}$  (see Figure 3.15(a)).

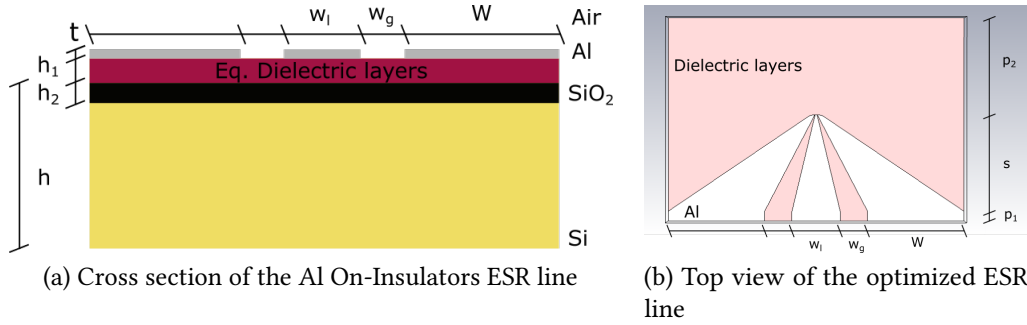


Figure 3.15: Geometry of the optimized Al On-Insulators structure

Moreover, the structure is optimized according to the guidelines reported in §3.3.4: in Figure 3.15(b) it is possible to have a look on the final design of the ESR line, while in Table 3.5 are reported the dimensions defining the microwave antenna. In particular, the value of the gap between the signal and the two ground lines is determined to be  $w_g \simeq 142\ \mu\text{m}$  by adopting the same procedure discussed in §3.3.2, in order to obtain a  $52\ \Omega$  impedance match at the CPW port interface.<sup>13</sup> The smaller gap difference is due to the fact that two dielectric layers with relative permittivities larger than the one of the substrate are present, reducing the value of the line capacitance and, therefore,

<sup>12</sup>In reality, this passivation coating is realized by combining many layers of different materials: such a technological process is implemented so that the layers result in a thin equivalent dielectric layer, whose relative permittivity is almost  $\epsilon_r \simeq 5$ .

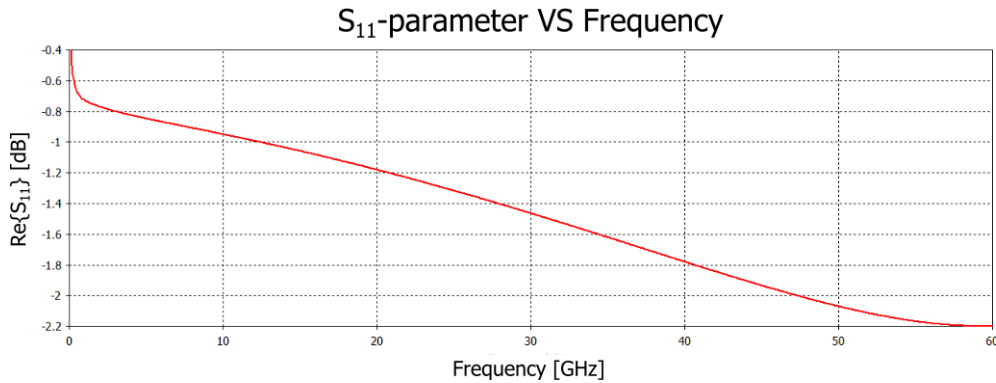
<sup>13</sup>As already explained in 2.1, no decrease in resistance has been observed in Al for CEA technological processes, so, the Al conductivity is set up to the default room-temperature value  $\sigma_{Al} \simeq 3,56 \times 10^7\ S/m$ : such a condition is, therefore, considered as a worst case situation.

Dimension	Value	Geometrical Meaning
$w_l$	250 $\mu m$	Signal Line Width
$w_g$	142 $\mu m$	Gap Width
$W$	500 $\mu m$	Ground Lines Width
$t$	200 $nm$	CPW Thickness
$h$	775 $\mu m$	Substrate Thickness
$h_1$	170 $nm$	Passivation Layer Thickness
$h_2$	145 $nm$	$SiO_2$ BOX Thickness
$p_1$	50 $\mu m$	CPW Length
$s$	500 $\mu m$	Transition Line Length
$p_2$	500 $\mu m$	QDs Region Length
$L_1$	10 $\mu m$	Short-Signal Line Width
$l$	800 $nm$	Short Length
$L_2$	20 $\mu m$	Short-Ground Lines Width
$c$	100 $nm$	Symmetry Angle Base
$r$	100 $nm$	Short Width

Table 3.5: Optimized geometrical dimensions for the Al On-Insulators ESR line

increasing the characteristic impedance: to compensate such effect, the signal-to-ground gap of the line has to be decreased. Furthermore, also the decrease in the Al conductivity with respect to the previous case plays a significant role in the variation of the gap.

For this case, the device is simulated under an injected power  $P_{in} = 0,1 mW = -10 dBm$ , to be more realistic for cryogenic implementations of the antenna. Once having defined the structure, it is possible to have a look on the behaviour of the  $S$ -parameter, shown in Figure 3.16: as predicted, the decrease of the longitudinal line dimension has allowed for an increase in the line inductance and capacitance, making resonance effects to disappear along the frequency range.

Figure 3.16:  $S$ -parameter of the optimized Al On-Insulators structure

## Electric and Magnetic Fields

For what it concerns the intensities of the fields in close proximity to the ESR antenna (always refer to Figure 3.8(a)<sup>14</sup> for having in mind the locations of the probes and the Qubits above the line), it is possible to obtain results similar to the ones for the Al On-Si structure; obviously,  $E$  and  $B$ -field intensities will be reduced, because of the different excitation power, one order of magnitude lower with respect to the previous case, and the optimized geometry. The 2D top view of the magnitudes at the passivation layer-air interface is depicted in Figure 3.17.

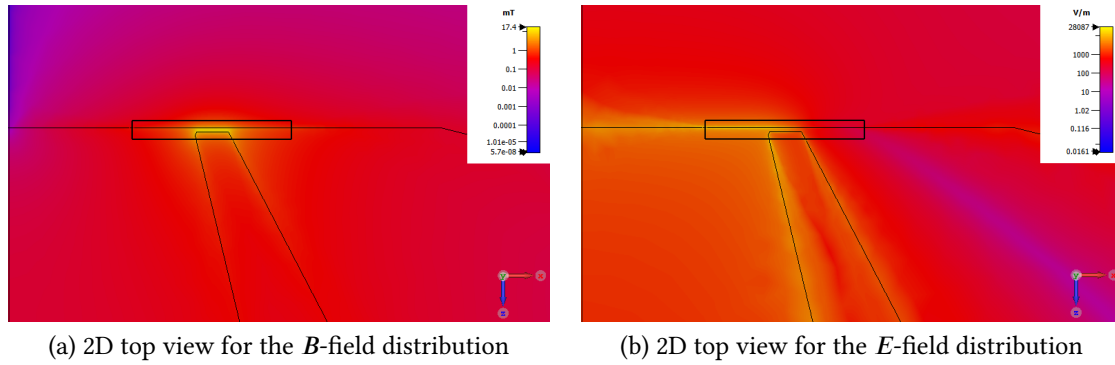


Figure 3.17: Field distributions at the optimized Al On-Insulators nano-antenna at  $10\text{ GHz}$  ( $P_{in} = -10\text{ dBm}$ )

Considering a frequency of  $10\text{ GHz}$ , the values of the magnetic and electric fields can be plotted along the  $x$ -axis parallel through the short antenna and passing through the QDs position probes. Such results, presented in Figure 3.18, are important for understanding where it should be more suitable to place spin Qubits for optimizing the influence of the generated  $B$ -field and minimize the action of the electric one. In particular, the maximum  $B$ -field intensity  $B_{MAX} = 1,41\text{ mT}$  is found to be at  $x = 5,62\ \mu\text{m}$  and a 5% decrease is observed between  $x_{min} = 5,29\ \mu\text{m}$  and  $x_{MAX} = 5,86\ \mu\text{m}$ . In these two last points, the electric field is measured to be  $E_{MAX} = 2,78\text{ kV/m}$  and  $E_{min} = 1,31\text{ kV/m}$ , suggesting that the QDs should be placed on the right side of the short line.

## Extraction of RLC Parameters

Finally, basing on the equivalent model presented in Figure 3.19, it is possible to extract the  $RLC$  parameters modelling the ESR line structure. In particular, these values can be

<sup>14</sup>For this configuration, the QDs are buried inside the passivation layer,  $10\text{ nm}$  above the equivalent dielectric-BOX interface.

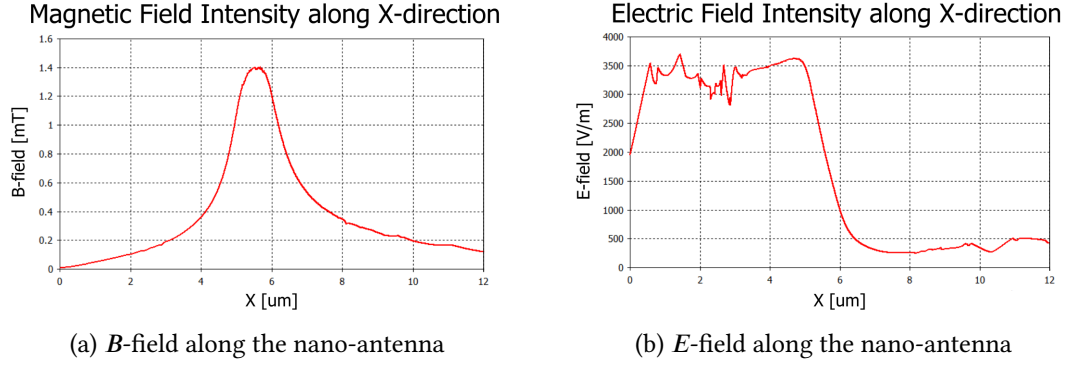


Figure 3.18: Electric and magnetic fields running parallel to the short line ( $P_{in} = -10 \text{ dBm}$ )

calculated by analysing the port impedance  $Z_{11}$  and admittance  $Y_{11}$ .<sup>15</sup> The values of the overall line resistance, inductance and capacitance are, actually, calculated as it follows:

$$R = \Re\{Z_{11}\}$$

$$L = \frac{\Im\{Z_{11}\}}{2\pi f}$$

$$C = \frac{\Im\{Y_{11}\}}{2\pi f}$$

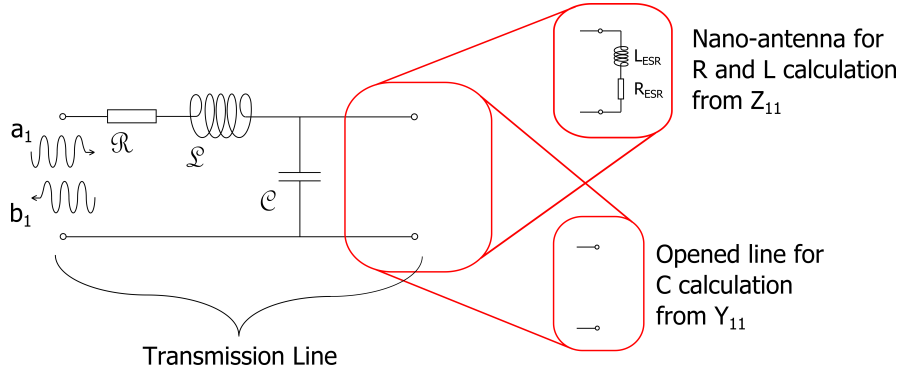


Figure 3.19: Simplified  $RLC$  model of the ESR line

In particular,  $R$  and  $L$  values also consider the contribution of the ESR antenna resistance  $R_{ESR}$  and inductance  $L_{ESR}$ , whose values are not negligible since, for instance,

<sup>15</sup> $Y_{11}$  can be used for extracting the value of the line capacitance  $C$ , simulating the ESR structure in an open-terminated condition: namely, without the two nano-antennas.

in DC it is possible to calculate  $R_{ESR_{DC}} = \frac{1}{\sigma_{Al}} \frac{l}{rt} \simeq 1,1 \Omega$ . As a matter of fact, having the smallest cross-section, the antenna represents the predominant contribution to the overall ESR line resistance. In Figure 3.20 are reported the frequency behaviours of the  $RLC$  parameters extracted by the impedance and admittance calculations: it is possible to clearly notice the presence of a resonance condition at around  $47 GHz$ . In order to exploit the ESR line in the predicted way, it is, therefore, important to excite it with frequencies below the  $40 GHz$  limit.

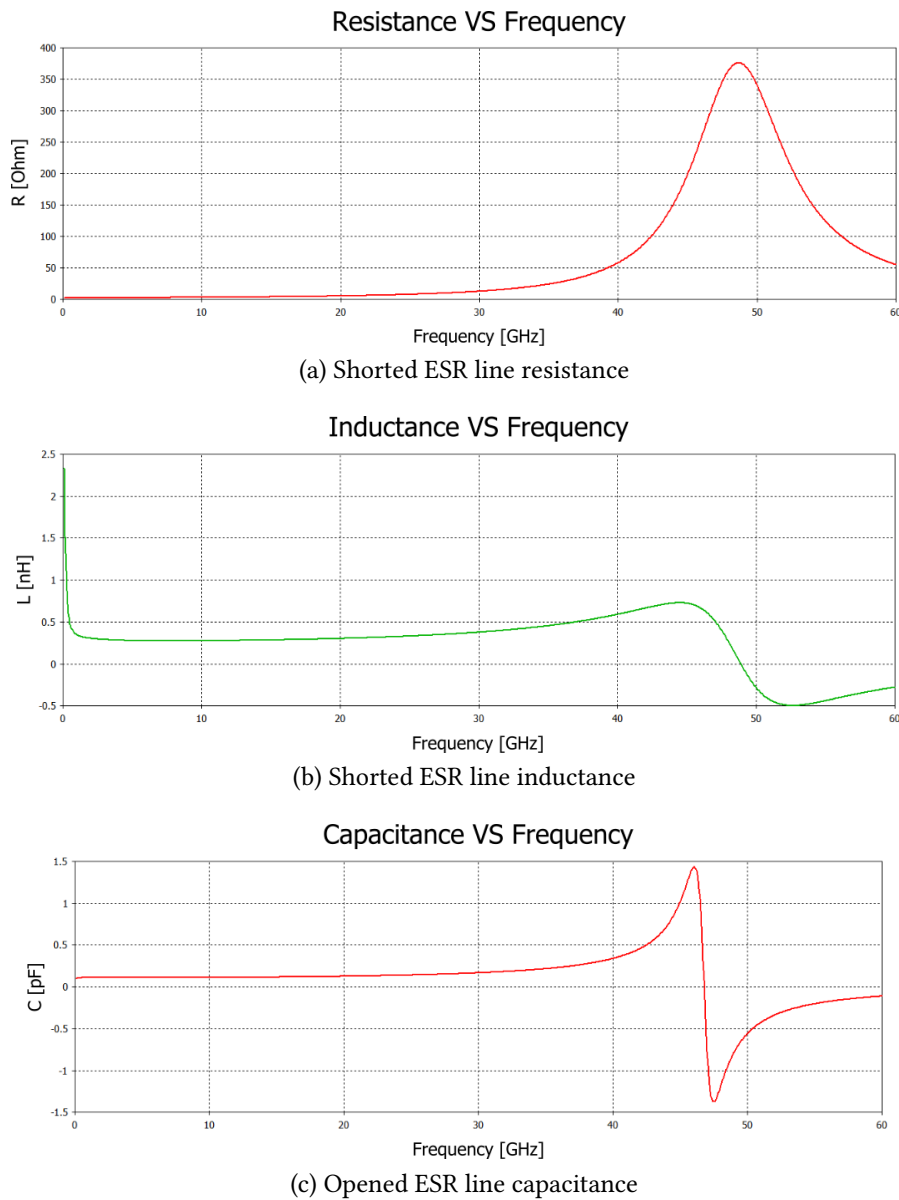


Figure 3.20:  $RLC$  parameters for the optimized Al On-Insulators ESR line

$f$ [GHz]	0,1	0,5	1	5	10	20	30
$R$ [ $\Omega$ ]	2,09	2,36	2,34	2,65	3,17	5,39	12,74
$L$ [nH]	2,33	0,47	0,34	0,28	0,27	0,30	0,38
$C$ [pF]	0,09	0,11	0,11	0,11	0,11	0,12	0,17

Table 3.6:  $RLC$  parameters values of the ESR line

Furthermore, in order to provide a quantitative estimation of the  $RLC$  model of the simulated ESR line, in Table 3.6 are reported the parameter values for some sampling frequencies over the whole range. In particular, such values are selected for frequencies well below the resonance frequency of the structure, where the line should be used in a reliable way not exciting parasitic components.

In the end, by means of Ampère's theorem, described in the following expression

$$\oint_S \mathbf{H}(\mathbf{r}, t) \cdot d\mathbf{l} = I_S$$

where  $S$  is a surface,  $d\mathbf{l}$  describes the infinitesimal length of the its contour and  $I_S$  is the total current circulating through the surface, it is possible to exploit CST<sup>®</sup> line-integration features to extract the value of the current circulating inside each short branch. In so doing, it is found out that, at 10 GHz, the total RMS current circulating inside the structure is

$$I = 0,353(I_{L_{pp}} + I_{R_{pp}}) = 0,353(1,977 \text{ mA} + 1,983 \text{ mA}) \simeq 1,398 \text{ mA}$$

being  $I_{L_{pp}}$  and  $I_{R_{pp}}$  the peak-to-peak values of the currents circulating, respectively, in the left and right shorting branches. Such a value results in a corresponding RMS injected power  $P_{in} = Z_0 I^2 \simeq 0,098 \text{ mW}$  for a  $Z_0 = 50 \Omega$  impedance structure: in so doing, it is possible to notice that the calculated power is different from the  $-10 \text{ dBm}$  specification only by a 2% factor, giving an idea about the accurate impedance matching condition for the ESR line.

In order to conclude, since the ESR structure resistance at 10 GHz is found to be  $R \simeq 3,17 \Omega$ , the RMS power dissipated by the line can be easily calculated as  $P_{diss} = RI^2 \simeq 6,20 \mu\text{W}$ , sufficiently low for cryogenic spin Qubits manipulation (see [43]).

## 3.4 Conclusion

Electron-Spin Resonance has shown to be a powerful and effective phenomenon to coherently control the spin state of Si Qubits. In particular, the generation of sufficiently high magnetic fields over a wide frequency range, by means of a short-circuited nano-antenna, is a key element to enable the realization of quantum gates in a CMOS-compatible technology. Moreover, the further emission of a small electric field plays a

significant role when considering also the possibility to build up the integrated gating components for readout mechanisms.

### 3.4.1 Achievements

In this chapter it has been first introduced the physical description of ESR for controlling the spin state of electrons in Si QDs, comparing, then, such a technique to the promising alternative of EDSR. In a second time, it has been discussed about the simulation and the optimization of an ESR line, whose design has been adapted from [43]. In particular, a first preliminary Al On-Si test has been set up, allowing to compare the simulation results with literature material. Later on, an optimization analysis has been performed over the ESR line, in order to provide the design of a higher performances structure, whose simulation has been, finally, implemented taking into account more realistic conditions for an Al On-Insulators line.

For what it concerns the main results obtained during this work, it has been possible to extract the values of the generated fields at the Qubits location, clearly showing that the ESR line is able to provide a few  $mT$   $B$ -field over a wide frequency range, while, at the same time, reducing the influence of  $E$ -fields on the QDs. In this way, the structure completely showed to represent an effective and valid control line implementation, respecting physical and design specifications. As a matter of fact, the proposed optimized ESR will be post-processed on a quantum chip by CEA experimental research group, in order to provide a reliable tool for investigating silicon Qubits properties and controlling QDs spin states.

In the end, by means of the extraction of  $RLC$  parameters, it has been possible to evaluate the performances of the component in terms of working frequency and power dissipation: for this last case, for few  $\mu W$  power consumption, it has been shown that the configuration fully respects the constraints for a cryogenic On-Chip implementation.

### 3.4.2 Future Work

Before definitely concluding the analysis of the spin control 1-metal layer structure described in this chapter, it is important to provide some guidelines for future researches on this topic. As a matter of fact, many aspects still need to be investigated: first of all, for example, a full study of EDSR techniques should be carried out, comparing the performances of these more recent alternatives to the aforementioned ESR line. In this perspective, both the opened nano-antenna and the gating structure reported in §3.2.2 could be seriously considered for the implementation of an electric field Qubits control line. Moreover, the  $RLC$  parameters extracted from the software could be analysed in order to develop a distributed-circuit model of the ESR line, pointing at obtaining a full Spice-compatible netlist for the study of the structure at more abstract levels.



## Chapter 4

# Planar Superconducting Inductor for Spin Qubits Readout

### 4.1 Introduction

Even if readout mechanisms have been proposed as the last criteria for validating an effective QC implementation (see [6]), there is no question that the possibility to accurately measure the final state of a Qubit is as important as the capability to coherently address it for computational purposes. As a matter of fact, because of the probabilistic nature of Qubits, a quantum computer should be able to provide a high-fidelity estimation of the results of a calculation, at least over a statistically repeated set of measures. In this sense, many different readout architectures have been proposed over the last years for Si-QC, ranging from proximal charge sensors, reported in [46], to the more innovative gate reflectometry (see [47]).

Indeed, CMOS technologies theoretically allow to easily integrate readout circuitry and front-end silicon QDs based SETs at cryogenic temperatures, largely contributing to the scalability of many Qubits on the same quantum processor. In particular, in the framework of gate reflectometry, an *RLC* resonator is connected to one of the two QDs control gates, in order to provide a dispersive information about spin states, by means of a shift in the resonance frequency of a gate-applied electric signal.

In this chapter it will be, therefore, first reported the most diffused techniques for implementing a high-fidelity readout of electron spins defining CMOS Qubits. In this perspective, a brief comparison between disruptive and dispersive mechanisms will be carried on and, then, the main working principle of gate reflectometry will be elucidated. Later on, there will be presented the most relevant results for the simulation of a superconducting coplanar inductor, an essential component to perform an accurate spin

readout by recurring to the aforementioned technique. Practically, a first simpler study will be set up as a benchmark test and, in a second, time, the definitive version of the inductance will be fully analysed, by exploiting microwave models for superconductivity.

## 4.2 Electron Spin State Readout

Since in silicon Quantum Computing the two energy levels systems on which Qubits are typically based are QDs electron spins, it is essential to design a reliable measurement apparatus that could detect, with high accuracy, single spin values. Unfortunately, as reported in [46], because of the very small magnetic moment of electron spin, such a quantity interacts with modern magnetometers in an extremely weak way, making its direct detection almost impossible and, even in the best cases, impracticable for a scalable quantum chip. However, recent developments in CMOS technologies have allowed the possibility to read the value of electron spin in solids; by exploiting spin-to-charge conversion inside confined nanostructures, it is now possible to implement readout systems able to detect electric signals associated to particular spin configurations.

Such techniques differentiate each others with respect to the fact of irremediably destroying the quantum state or not. In particular, double QDs SET current measurements and gate reflectometry will be now compared, focusing, later on, on this latter mechanism for the design of high-performances superconducting readout circuitries.

### 4.2.1 SET Current Disruptive Readout

As it has been already explained in §1.2.3, a CMOS silicon spin Qubit is basically made up of two quantum dots, confined along a silicon nanowire by means of the application of two gate voltages. In particular, the gating structures, which are fabricated close enough to make inter-dots single electron tunneling possible, are essential to define QDs wells, provide coherent control on one QD electron spin and implement electrostatically-driven spin readout on the other one. In Figure 4.1 it is presented a schematic description of such a structure, in which gate 1 is providing microwave spin control by means of EDSR technique and gate 2 is dedicated to the application of the detuning potential  $\Delta V_G$ .<sup>1</sup>

As explained in [46], Coulomb blockade phenomenon, originating from the 3D confinement introduced by the presence of two QDs and a non-zero inter-dot tunneling probability  $T_{tun}$ , is exploited along the nanowire in order to make a single-electron<sup>2</sup>

<sup>1</sup>The detuning energy, defined as  $\epsilon = -e(V_R - V_L) = -e(V_{G2} - V_{G1})$ , is a crucial electric signal for the the correct alignment of QDs levels, making inter-dots tunneling possible.

<sup>2</sup>In reality, the device demonstrated in [16] is basing on holes-current, since their control via EDSR, and therefore an electric field, is much more effective with respect to electrons, because of a stronger spin-orbit holes coupling. The scope of this short explanation of Qubits readout techniques is well-beyond a solid-state description of such a phenomenon and, so, electrons and holes are considered in the same way for readout issues: the interested reader can refer to [18] for more information on holes physics.

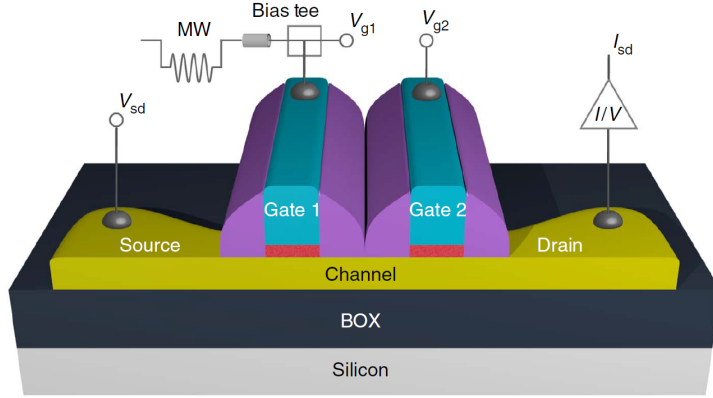


Figure 4.1: Graphical representation of a CMOS silicon spin Qubit [16]

current circulating from the source to the drain reservoirs: in so doing, it is possible to physically address single spin states. However, in such a situation, the energy quantization is still degenerate for spin configurations, making impossible to distinguish if an electron possesses a spin-up or a spin-down value: to overcome this issue, an external static magnetic field  $\mathbf{B}_0(\mathbf{r})$  is applied in-plane, originating a Zeeman energy splitting for  $|\uparrow\rangle$  and  $|\downarrow\rangle$  spin populations.

### Spin States Double Quantum Dots Systems

By controlling both  $V_L = V_{G1}$  and  $V_R = V_{G2}$ , it is possible to tune the number of electrons inside each quantum dot by integer quantities (see [40]). Assuming to adopt the  $(L, R)$  convention for indicating the electron configuration of the two QDs (where  $L$  and  $R$  denote, respectively, the number of electrons inside the left-1 and right-2 QDs), only  $(0,1)$ ,  $(1,1)$  and  $(0,2)$  cases are interesting for spin quantum computing.<sup>3</sup> In this perspective, the first one denotes the occupation of the only right dot, while the second one represents the occupation, with different spins, of both the left and the right dots; the last one is, trivially, the case in which 2 electrons occupy the right dot, having opposite spin values. The right spin has to be, therefore, in a perfectly known and fixed spin state, working as a comparison term for the left one: such a value must be preliminary established with an initialization phase of the Qubit.

From Quantum Mechanics, it is possible to demonstrate (see [36]) that the 2-spins system can be generally described in terms of two spin wavefunctions, a singlet state  $S(L, R)$  and a triplet one  $T(L, R)$ . In Figure 4.2(a) there are depicted the energy levels of such a system, for both the  $(1,1)$  and  $(0,2)$  configurations. In particular, this last schematic reports the case for  $T_{tun} = 0$  and  $\mathbf{B}_0 = 0$ , meaning that no interaction is

<sup>3</sup>In order to implement a single Qubit, relying on single spin configurations, only 1 confined electron per QD must be actually considered.

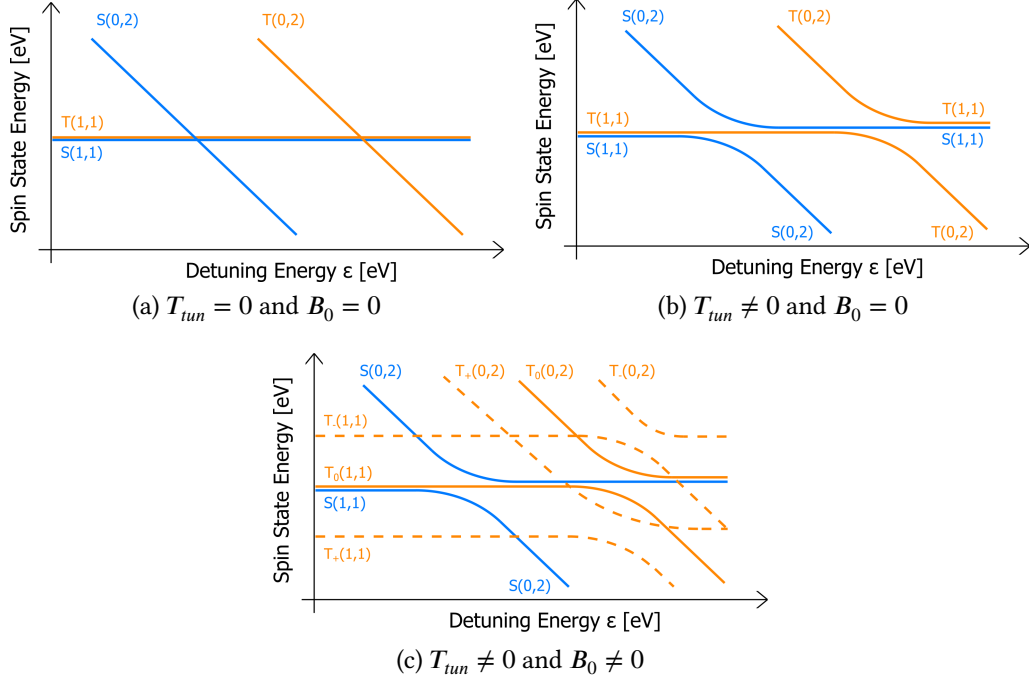


Figure 4.2: Two spins QDs energy levels with respect to detuning (adapted from [46])

possible between the two dots and the triplet states are still degenerate. Proceeding in this discussion, if the two QDs are close enough to allow tunneling phenomena (*i.e.*  $T_{tun} \neq 0$ ), the situation evolves as represented in Figure 4.2(b), in which it is possible to notice state hybridization due to inter-dots coupling: in particular, since tunneling transitions must preserve spin values,  $S(1,1)$  and  $T(1,1)$  only hybridize, respectively, with  $S(0,2)$  and  $T(0,2)$ .

Finally, if also a static  $\mathbf{B}_0(\mathbf{r})$  field is applied,<sup>4</sup> then the triplet states become energetically distinguishable, making the associated energy levels to broaden (see Figure 4.2(c)) and describing the (1,1) and (0,2) configurations with respect to the following spin wavefunctions:

$$\begin{aligned}
 S(1,1) &= (|\uparrow_L \downarrow_R\rangle - |\downarrow_L \uparrow_R\rangle)/\sqrt{2} & S(0,2) &= (|\uparrow_R \downarrow_R\rangle - |\downarrow_R \uparrow_R\rangle)/\sqrt{2} \\
 T_0(1,1) &= (|\uparrow_L \downarrow_R\rangle + |\downarrow_L \uparrow_R\rangle)/\sqrt{2} & T_0(0,2) &= (|\uparrow_R \downarrow_R\rangle + |\downarrow_R \uparrow_R\rangle)/\sqrt{2} \\
 T_+(1,1) &= |\uparrow_L \uparrow_R\rangle & T_+(0,2) &= |\uparrow_R \uparrow_R\rangle \\
 T_-(1,1) &= |\downarrow_L \downarrow_R\rangle & T_-(0,2) &= |\downarrow_R \downarrow_R\rangle
 \end{aligned}$$

<sup>4</sup>Such a magnetic field must be sufficiently high to overcome thermal fluctuations: its broadening energy  $E_Z$  must be, therefore, at least larger than  $5k_B T$ , as already explained in §3.3.1.

In such a way, by fixing a particular value for the detuning energy  $\epsilon$ , it is possible to align, or eventually misalign, the energy levels inside the two QDs for making spin-driven tunneling possible along the nanowire: only electron transitions that satisfy Pauli exclusion principle can actually occur, as it will be elucidated in the following section.

### Spin-to-Charge Conversion

Once having defined the different spin configurations that the two QDs system can occupy, both in terms of singlet and triplet spin states and the corresponding energy levels, it is necessary to introduce the phenomenon known as Pauli blockade, to understand how it is possible to exploit inter-dots transitions for Qubits readout. Such a quantum mechanism mainly arises from simple energy considerations: in particular, Figure 4.3 schematically shows the spin dynamics leading to the generation of a measurable SET current.

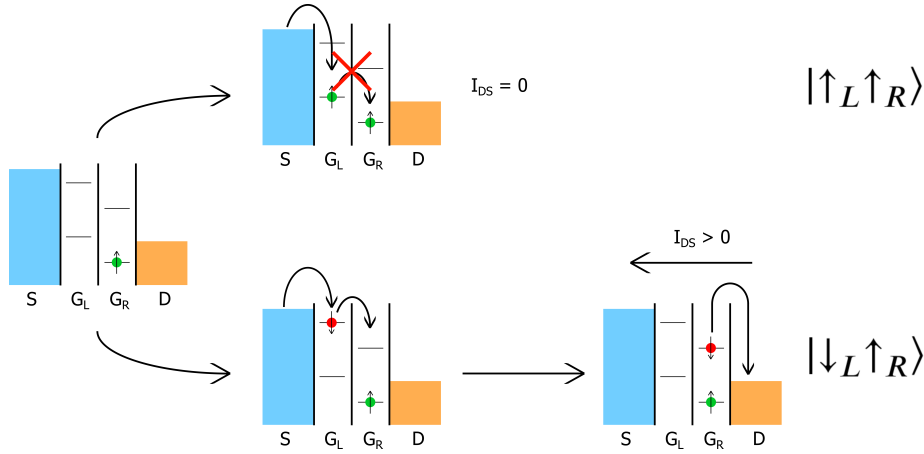


Figure 4.3: Schematic description of possible SET current dynamics

As a matter of fact, when applying a positive  $V_{SD}$ , an electron from the source reservoir can enter the left quantum dot, occupying a ground or an excited level basing on its spin value. Such an electron spin, together with the reference one present in the right dot, can form, therefore, a singlet state  $S(1,1)$  or a triplet one  $T(1,1)$ . At this moment, because of spin conservation tunneling (see [46]), the configuration can naturally evolve from  $S(1,1)$  to  $S(0,2)$ , or from  $T(1,1)$  to  $T(0,2)$ . If a particular detuning is applied at the two gates (usually set in the proximity of the  $S(L, R)$  curve bending), only the transition between singlet states would be allowed, while the one between triplet states would be forbidden, being the energy difference between the  $T(L, R)$  states too high for tunneling.<sup>5</sup> In so doing, only for the singlet-to-singlet transition it will be

<sup>5</sup>In reality, such a transition can happen by means of a photon-assisted phenomenon, in which

generated a single electron current, flowing through the all length of the nanowire, from the drain to the source: as reported in [46], such a current, in the order of the tens of  $fA$ , can be effectively measured, providing a successful method to understand if the left electron possesses the same spin as the reference right one, or not.

## 4.2.2 Gate Reflectometry Dispersive Readout

Even if the previous techniques have been crucial for demonstrating the practical implementation of a CMOS silicon spin Qubit (see [16]), many aspects prevent the spin-to-charge based SET current to be an effective readout mechanism for a many Qubits quantum processor. As a matter of fact, such a phenomenon is purely disruptive, meaning that the quantum information is completely lost and no more available for further calculations, since the controlled electron spin can be transported from one dot to the drain reservoir. Furthermore, as explained in [46], because of the  $RC$  characteristic delay introduced by the nanowire, the tunnel rate is basically limited to some  $kHz$ : since the best coherence time, that can be achieved today in spin Qubits, is in the order of milliseconds, such a consideration implies that only very few operations can be performed on a Qubit before it loses its quantum properties. In order to overcome such an issue, in the last years it has been proposed a new innovative spin readout setup, relying on a gate sensing measurement, called gate reflectometry: such a technique has been, actually, demonstrated to reach  $GHz$  speeds, providing a spin single shot measurement fidelity larger than 98%, as discussed in [48].

### QDs Differential Quantum Capacitance

The key idea for discriminating between a  $|\uparrow_L\uparrow_R\rangle$  and a  $|\downarrow_L\uparrow_R\rangle$  spin state, by exploiting a gate sensing technique not requiring any drain-to-source current, relies on the fact that the two QDs inside the silicon nanowire are theoretically coupled by a tunnel quantum capacitance  $C_Q$ . In particular, the value of such a capacitance depends on the spin configuration of the Qubit; it is actually possible to demonstrate (see [49]) that this quantity is proportional to the curvature of the 2-spins system energy levels as following:

$$C_Q \propto \frac{\partial^2 E(\epsilon)}{\partial^2 \epsilon}$$

In so doing, if the detuning potential  $\epsilon_0$  is correctly set to be located at the  $S(1,1)$ -to- $S(0,2)$  hybridization region, as it is depicted in Figure 4.4, the quantum capacitance

---

an electromagnetic wave can provide sufficient energy for realizing the inter-dots spin transfer: this phenomenon is a killing effect for accurate spin readout and this is the reason why the design of the nanoantenna in §3.3.2 has been made in order to minimize the intensity of electric fields at the Qubit location.

related to the triplet  $|\uparrow_L \uparrow_R\rangle$  spin configuration will be 0, while a non-zero value will be observed for the singlet  $|\downarrow_L \uparrow_R\rangle$  state.

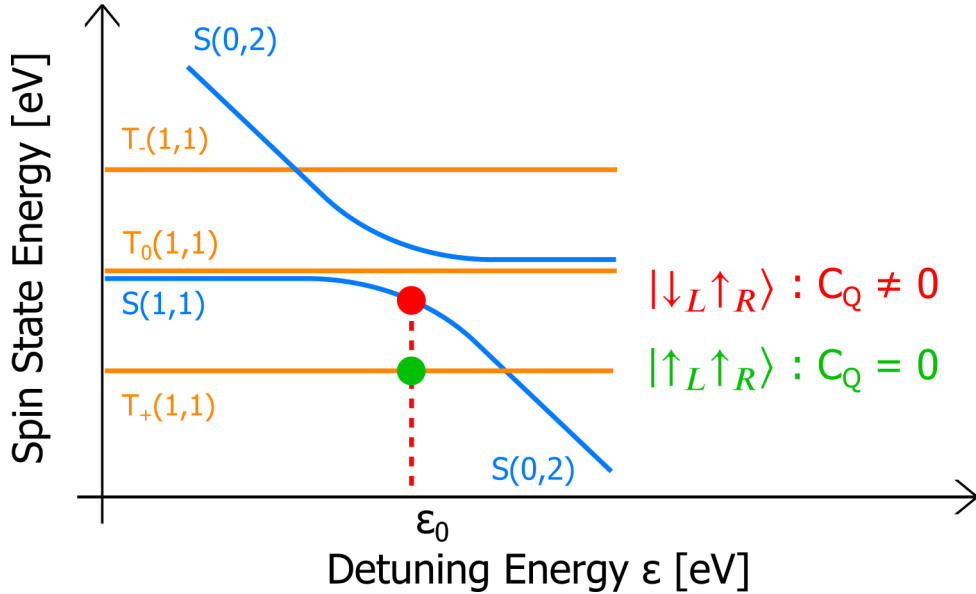


Figure 4.4: Inter-dots  $C_Q$  dependence on the energy levels bending (adapted from [50])

### RLC Gate Resonator

Once having introduced the characteristic phenomenon on which gate reflectometry is based, it is now possible to proceed to the explanation of its practical implementation. In this sense, Figure 4.5 schematically presents the common circuitry that is currently used for analysing CMOS spin Qubits. In particular, on the left it is shown the microwave excitation that has to be applied at gate 1 in order to provide a coherent control of the target spin, while the right side of the picture reports the circuit devoted to Qubit readout, by means of the gate sensing of the reference right dot.

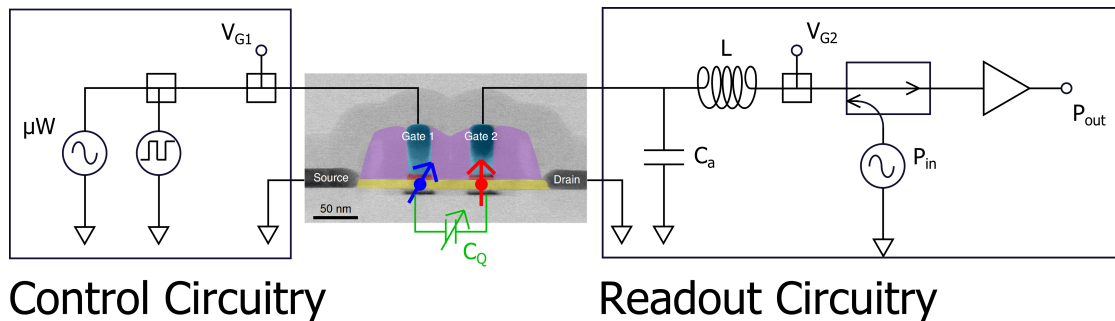


Figure 4.5: Schematic showing CMOS spin Qubits control and readout circuits

It is important to notice that both the source and the drain reservoirs have been grounded, in order to avoid current circulating along the nanowire.<sup>6</sup> Moreover, focusing on the readout part of the structure, an RF electric signal is applied to gate 2, as explained in [51], in order to sense a variation of the total gate capacitance, being  $C_a$  a parasitic component resulting from gate-to-bulk coupling, while  $C_Q$  is the aforementioned quantum capacitance, whose value depends on the spin configuration of the Qubit.

In this perspective, the CMOS Qubit acts as a variable capacitive load for the AC generator, electrically resulting in a series *RLC* circuit.<sup>7</sup> Since the resonance frequency of the system is defined as

$$f_r = \frac{1}{2\pi\sqrt{LC}}$$

such a quantity will assume, in principle, 2 values, depending on the value of the quantum capacitance. In so doing, a shift in the resonance frequency of the system, measured by means of either the amplitude or the phase of the reflected signal, as reported in [51], will provide a single shot accurate measurement of the state of the target spin Qubit. Such a sensing operation is possible thanks to a reflection of the input power, due to the high impedance termination of the line at the resonance frequency (see [50]).

### 4.2.3 Superconductivity Models for HF Components Design

In order to implement such a gate reflectometry scheme, it is essential to accurately assess the RF performance of the inductor which, together with the variable capacitance, is able to introduce an *LC* characteristic resonance for the readout circuitry. Unfortunately, common surface-mounted inductors present a parasitic series resistance that can contribute in a significant way to the degradation of the sensitivity of the apparatus, by absorbing and dissipating the signal power.

In order to overcome such an issue, since Qubits require cryogenic temperatures to coherently maintain their quantum properties, it is possible to exploit superconducting materials, possessing an extremely low parasitic resistance at high frequencies. In so doing, as explained in [47], the detrimental losses introduced in the sensing structure by normal metals, accounting even for a relevant 10% attenuation of the reflected signal, can be drastically reduced, improving the overall performances of gate reflectometry (see [48]). However, before proceeding with the detailed explanation of the inductor design and the related simulation results, it is important to spend some few words about superconductivity and how it can be modelled for RF components analysis.

---

<sup>6</sup>In this configuration, gate reflectometry is able to sense electron spin without any charge collection, preserving, therefore, quantum information inside the Qubit and implementing a dispersive readout mechanism.

<sup>7</sup>In reality, also a series resistance term should be considered, but in this work the inductor will be designed by recurring to a superconducting material, with a negligible AC resistance, as discussed in §4.2.3.



## London's Equations

Superconductivity is a peculiar property of some materials, for which, if cooled down below a characteristic critical temperature  $T_C$ , they exhibit an abrupt transition in their conducting state, showing a perfect 0 resistance in DC. Moreover, when undergoing such a state transition, these materials are also able to completely expel external magnetic fields from their inner solid volume.<sup>8</sup> As reported in [52], such a property has been intensively exploited in the last decades for the implementation of high-performances RF structures: as a matter of fact, superconductors present a non-zero resistance in AC, but still many orders of magnitude smaller than classical conductors, allowing to design microwave structures with very low losses and high quality factors (see [25]).

In order to explain such an anomalous phenomenon, in 1935 the German physicists Fritz and Heinz London derived two phenomenological equations able to predict perfect conductivity and the Meissner effect for a metal at cryogenic temperatures. In particular, assuming that the whole current circulating in a superconductor is made up of both a normal and a superconducting contributions,<sup>9</sup> namely  $\mathbf{J} = \mathbf{J}_n + \mathbf{J}_s$ , then it is possible to demonstrate (see [41]) that the behaviour of the superconducting current is ruled by the following equations:

$$\frac{\partial \mathbf{J}_s}{\partial t} = \frac{n_s e^2}{m_e} \mathbf{E} = \frac{1}{\Lambda} \mathbf{E} \quad (4.2.3.1)$$

$$\nabla \times \mathbf{J}_s = -\frac{n_s e^2}{m_e} \mathbf{B} \quad (4.2.3.2)$$

being  $n_s$  the superconducting carriers density.

It is important to notice that Equation 4.2.3.1 can be used to define an imaginary conductivity for superconducting Cooper's pairs, while Equation 4.2.3.2 can be combined to DC Ampère's law  $\nabla \times \mathbf{B} = \mu_0 \mathbf{J}_s$  and Gauss' law for magnetism  $\nabla \cdot \mathbf{B} = 0$  in order to find out:

$$\nabla^2 \mathbf{B} = \mu_0 \frac{n_s e^2}{m_e} \mathbf{B} = \frac{1}{\lambda_L^2} \mathbf{B} \quad \text{where} \quad \lambda_L = \sqrt{\frac{m_e}{\mu_0 n_s e^2}}$$

In this last case, an external magnetic field, propagating at the  $z = 0$  surface of the superconductor inside the metal volume, has to present an expression like  $\mathbf{B}(z) = \mathbf{B}(0)e^{-z/\lambda_L}$ . In so doing, a magnetic field will exponentially decay at the outer surface of a superconductor, propagating inside only for a few nanometres characteristic length  $\lambda_L$ , called London penetration depth, which basically defines a thin outer shell where the whole current is forced to circulate inside the superconductor.

<sup>8</sup>These effects, respectively named perfect conductivity and Meissner–Ochsenfeld effect, are the two characteristic phenomena describing superconductivity and they cannot be predicted by classical electromagnetism theories.

<sup>9</sup>This latter is characterized by a theoretically  $\tau_s \rightarrow \infty$  collision time for its super-carriers, resulting in no scattering events and, therefore, originating a DC infinite conductivity.

### Two-Fluids Complex Conductivity Model

In this perspective, it is possible to calculate the HF conductivity of a superconducting material reasoning on the fact that, for  $T < T_C$ , the current inside the superconductor is carried both by normal electrons and superconducting Cooper's pairs, whose state densities are respectively  $n_n$  and  $n_s$ , linked together by the following expressions:

$$\begin{cases} n = n_n + n_s \\ \left(\frac{n_n}{n_s}\right) = \left(\frac{T}{T_C}\right)^4 \end{cases}$$

Moreover, since the total current is made up of both a  $\mathbf{J}_n$  term and a  $\mathbf{J}_s$  one, as explained in [53], each contribution will be linked to the electric field  $\mathbf{E}$  respectively as

$$\begin{aligned} \mathbf{E} &= \Lambda \frac{\partial \mathbf{J}_s}{\partial t} \\ e\mathbf{E} - \frac{m_e}{n_n e} \frac{\mathbf{J}_n}{\tau_n} &= \frac{m_e}{n_n e} \frac{d\mathbf{J}_n}{dt} \end{aligned}$$

where the dynamics of superconducting electrons is governed by the first London's equation, while the one of normal electrons is derived by the Drude's model of metallic HF conductivity.

Assuming, now, that both currents are frequency-dependent (*i.e.*  $\mathbf{J}_{n,s}(t) = \mathbf{J}_{n,s}(0)e^{j\omega t}$ ), it is possible to find an analogous Ohm's law proportionality expression between the total current and the electric field, as  $\mathbf{J} = \mathbf{J}_n + \mathbf{J}_s = \sigma \mathbf{E}$ , where the HF superconducting conductivity is a complex quantity defined as following:

$$\sigma = \sigma_1 - j\sigma_2 = \frac{n_n}{n_s} \frac{\tau_n}{\Lambda} \left( \frac{1}{1 + (\omega\tau_n)^2} \right) - j \frac{1}{\Lambda\omega} \left[ 1 + \frac{n_n}{n_s} \frac{(\omega\tau_n)^2}{1 + (\omega\tau_n)^2} \right] \quad (4.2.3.3)$$

Even if such a simple model for describing a superconducting material, based on the definition of two-fluids complex conductivity, relies on London's equations (only providing a phenomenological explanation of superconductivity effects and not able to predict the normal transition under over-critical current and field conditions, as discussed in [52]),<sup>10</sup> it efficiently proved its validity for modelling and simulating superconducting RF transmission lines (see [54],[55] and [56]), all over the last decades.

### Superconducting Surface Impedance Model

By developing more in deep the calculations of the two-fluids model, since the circulating current is theoretically constrained to a very few nanometres outer shell, it is possible to

---

<sup>10</sup>In order to consider the field-dependent behaviour of superconductivity, more sophisticated models, based on Ginzburg-Landau phenomenological or BCS microscopic theories, should be adopted (see [41]): in the following simulation work, such complex models will not be considered.

derive a simplified model for the definition of a superconducting material. As a matter of fact, as explained in [53], it is possible to introduce the concept of surface impedance  $Z_S = R_S + jX_S$ , in order to describe the limited propagation of the electromagnetic field inside a superconductor. In particular,  $R_S$  describes the surface resistance term associated to the motion of classical electrons, while  $X_S$  is the surface reactance describing the inductive behaviour of the Cooper's pairs circulating inside the material; practically, it is possible to derive the expressions of these two quantities, as done in [53], obtaining that:

$$\begin{cases} R_S = \frac{\mu_0 \lambda_L \omega^2}{2} \frac{n_n}{n_s} \tau_n \\ X_S = \mu_0 \lambda_L \omega \end{cases} \quad (4.2.3.4)$$

In the end, by means of this impedance definition, it is possible to define a superconductor simply in terms of its external surfaces: this approach can simplify simulation complexity and reduce calculation times, still preserving the correct description of superconducting effects, as reported in [56].

## 4.3 Electromagnetic Simulation of a Planar Superconducting Inductor

Dealing with gate reflectometry readout, the design of the gated series inductor is crucial for correctly setting up the value of the resonance frequency of the  $RLC$  spin sensing circuit and to provide a high quality factor of the resonator. . This section is, therefore, devoted to the description of a planar superconducting spiral inductor, designed for a high-performances gate reflectometry readout: in particular, Ansys<sup>®</sup> HFSS<sup>®</sup> software will be used for simulating a simpler benchmark structure, aiming at understanding the validity of the previous HF superconductivity models. Then, the final version of the inductor will be analysed, in order to extract its electromagnetic parameters and evaluating its performances.

### 4.3.1 Planar Inductor Design

The superconducting inductor has been designed by the Néel Institute group, in the framework of the Quantum Silicon Grenoble collaboration project between Grenoble CEA-LETI, CEA-IRIG and CNRS, exploiting a spiral coplanar circular shape, in order to uncouple it with respect to the in-plane external static magnetic field  $\mathbf{B}_0(\mathbf{r})$  (see [57]). Figure 4.6 presents the overall structure of such an RF component: in terms of materials, the inductor is made up of Niobium (a type-I superconductor undergoing a transition at  $T_C \simeq 9,2 K$ , as reported in [41]) on a silicon substrate.

In particular, the inductance value is calculated by means of the current sheet approximated expression described in [58] and reported in the following:

$$L_S \simeq L_{csa} = \frac{\mu_0 n^2 D_{avg} c_1}{2} \left[ \ln(c_2/\rho) + c_3 \rho + c_4 \rho^2 \right] \quad (4.3.1.1)$$

being  $n$  the number of spiral turns constituting the inductor,  $D_{avg} = \frac{2R_i + 2(R_i + W_o)}{2}$ ,  $\rho = \frac{R_i + W_o - R_i}{R_i + W_o + R_i}$  and  $c_j$  are layout dependent coefficients<sup>11</sup> and the other parameters are defined in Table 4.1.

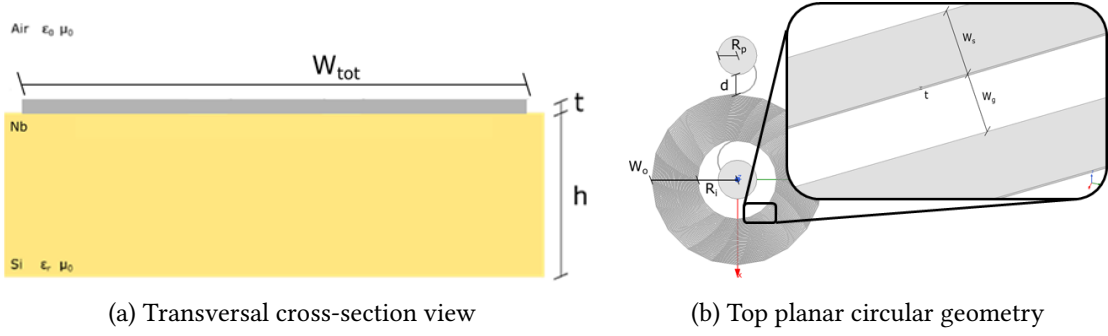


Figure 4.6: planar superconducting Nb spiral inductor geometry

### Geometry Definition

In Table 4.1 are reported the geometrical parameters defining the aforementioned inductor; by substituting such quantities into Equation 4.3.1.1, it is possible to find an inductance value of nearly  $L_S \simeq 517,64 \text{ nH}$ . In particular, considering such geometrical parameters, the total length of the inductor can be calculated by means of a line integral in polar coordinates on the radius function  $r(\varphi) = R_i + \frac{W_s + W_g}{2\pi} \varphi$  (for  $\varphi \in [0, 2\pi n]$ ) as:

$$\begin{aligned} l &= \int_0^{2\pi n} \sqrt{r^2 + \left(\frac{dr}{d\varphi}\right)^2} d\varphi = \dots = \\ &= \frac{W_s + W_g}{2\pi} \left( \frac{\Phi}{2} \sqrt{\Phi^2 + 1} + \frac{1}{2} \ln(\Phi + \sqrt{\Phi^2 + 1}) \right) \Big|_{\Phi_0}^{\Phi_1} \simeq 45,24 \text{ mm} \end{aligned}$$

being  $\Phi = \varphi + \frac{2\pi R_i}{W_s + W_g}$  an exchange variable necessary to analytically solve the line integral.

<sup>11</sup>For a circular spiral layout, such coefficients are respectively  $c_1 = 1,00$ ,  $c_2 = 2,46$ ,  $c_3 = 0,00$  and  $c_4 = 0,20$ .

Dimension	Value	Geometrical Meaning
$n$	30	Number of Turns
$W_s$	$3 \mu m$	Line Width
$W_g$	$3 \mu m$	Gap Width
$W_o$	$177 \mu m$	30 Turns Spiral Width
$W_{tot}$	$654 \mu m$	Whole Inductor Outer Diameter
$R_i$	$150 \mu m$	Internal Radius
$R_p$	$75 \mu m$	Pads Radius
$d$	$75 \mu m$	External Pad Distance
$t$	$60 nm$	Nb Line Thickness
$h$	$775 \mu m$	Si Substrate Thickness

Table 4.1: Geometrical dimensions for the Nb planar inductor

Moreover, as shown in Figure 4.6(b), the inductor shape implemented in Ansys® HFSS® is not perfectly circular: this is done in order to simplify the 3D meshing procedure of the structure and, therefore, reduce simulation time. Finally, it is important to highlight the fact that a 1-port simulation is carried out, both for the 2-turns benchmark and for the 30-turns final versions, in order to consider a much simpler analysis in terms of computational time and complexity : the simulation setup procedure is reported, for the sake of completeness, in appendix §C.1.

### Superconducting Niobium Models

Before proceeding, it is useful to spend some last few words about the superconductivity models that are used to describe Nb at  $T = 4 K$  cryogenic temperature, in the superconducting state. As a matter of fact, three different models will be basically used in the following descriptions, summed up as:

- **Perfect Electric Conductor (PEC):** a material with an ideal and constant 0 resistance is used in order to represent the perfect conductivity of the Nb inductor. In Ansys® HFSS®, such a material description is provided by default by the *PEC* material, having the highest possible finite conductivity the software can handle, that is to say,  $\sigma_{PEC} = 10^{30} S/m$ ;<sup>12</sup>
- **London Complex Conductivity:** in this case, a material with the complex conductivity derived by the two-fluids model is defined for the spiral inductor (see

<sup>12</sup>In reality, a fourth model is considered, dealing with a very high conductivity  $\sigma_{fc} = 10^{15} S/m$ , but still lower than PEC case, in order to consider the presence of slightly more losses: such a case is defined in the following as **Finite Conductivity** model.

§4.2.3), having such a quantity equal to:

$$\sigma_{complex} = \sigma_1 - j\sigma_2 = \frac{n_n \tau_n}{n_s \Lambda} \left( \frac{1}{1 + (\omega\tau_n)^2} \right) - j \frac{1}{\Lambda\omega} \left[ 1 + \frac{n_n}{n_s} \frac{(\omega\tau_n)^2}{1 + (\omega\tau_n)^2} \right]$$

- **Surface Impedance:** also the situation taking into account the superconducting surface impedance is considered, as explained in §4.2.3, defining a 3D virtual void inductor, on whose surface is applied a surface impedance boundary defined as:

$$Z_S = R_S + jX_S = \frac{\mu_0 \lambda_L \omega^2}{2} \frac{n_n}{n_s} \tau_n + j\mu_0 \lambda_L \omega$$

In particular, in Table 4.2 are reported the Nb parameters defining its superconducting nature, as extracted by [56].

Parameter	Value	Geometrical Meaning
$T$	4 K	Nb Working Temperature
$T_C$	9,2 K	Nb Critical Temperature
$\tau_n$	$10^{-12}$ s	Normal Electrons Collision Time
$\lambda_L$	100 nm	Nb London Penetration Depth

Table 4.2: Superconductivity parameters for two-fluids and  $Z_S$  models

Furthermore, Figure 4.7 describes a simplified equivalent model of the 1-port superconducting inductor, considering main HF parasitic effects at 4 K. In particular, a capacitance  $C_P$  is placed in parallel to the inductance, modelling the electric coupling between spiral turns, between the planar line and the reference ground, and accounting for the parasitic capacitance coming from the pads;  $L_S$  is the designed geometrical inductance due to the induced external magnetic flux. On the other hand,  $R_S$  defines the parasitic series resistance originated by RF losses in superconducting materials, while  $L_{kin}$  the so-called kinetic inductance of the superconductor (see [59]). As explained in [53] such a last term mainly originates from the AC motion of high-mobility Cooper's pairs inside the material; the energy of these quasi-particles can be actually modelled as an inductive term, defined basing on the following equations:<sup>13</sup>

$$\begin{cases} \frac{1}{2} m_s v_s^2 (n_s l A) = \frac{1}{2} L_{kin} I_s^2 \\ I_s = e_s v_s n_s A \end{cases}$$

<sup>13</sup>In particular, for  $t < \lambda_L$ , it is possible to assume that the current is homogeneously circulating inside the superconductor, resulting in an effective cross-section  $A \simeq W_s t$ .

being  $m_s = 2m_e$  and  $e_s = 2e$  respectively the mass and charge of a Cooper's pair. By merging together such expressions for  $t < \lambda_L$ , it is possible to find the value of the kinetic inductance as  $L_{kin} = \frac{\mu_0 \lambda_L^2}{W_{st}} l \simeq 3,16 \text{ nH}$ . This quantity is, therefore, absolutely negligible with respect to the design external inductance  $L_S \simeq 517 \text{ nH}$  and it will not be, therefore, considered in the next discussions.

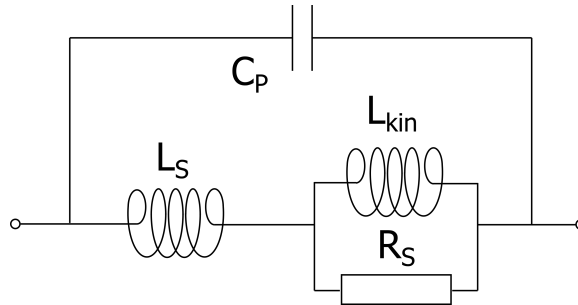


Figure 4.7: Proposed equivalent lumped model of a superconducting inductor

### 4.3.2 Simulation Results of a 2-Turns Benchmark Inductor

First of all, because of the complex geometry of the Nb planar superconducting inductor and its peculiar properties, it is necessary to perform a preliminary simulation of a much simpler structure, in order to assess the validity of the aforementioned superconductivity models. To do so, an inductor having exactly the same geometrical and material parameters as the ones reported in §4.3.1, but made up of only  $n = 2$  turns, is analysed, whose geometry is shown in Figure 4.8.

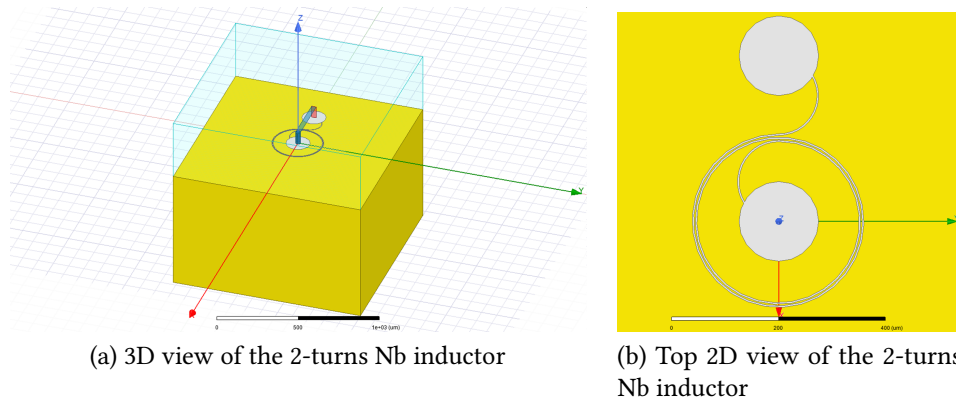


Figure 4.8: 2-turns benchmark Nb inductor

As usual, before simulating the whole structure, it is important to correctly set the dimensions of the lumped port excitation. In particular, the shorting Perfect Electric

(PE) field boundary that is applied between the port and the PEC cylinder, in order to close the circuit for a 1-port analysis, could perturb the propagation of the fields: such a boundary, actually, acts as a 0 tangential  $E$ -field, simulating a perfect electric conducting sheet. A sweep on the height of the lumped port  $h_L$  is made, as explained in appendix §C.2, finding out that a sufficient value for  $R_S$ ,  $L_S$  and  $Q$  convergence is  $80 \mu\text{m}$ . After having set the correct value for the port sizing, it is possible to proceed to simulate this benchmark structure over a  $[100 \text{ MHz}; 20 \text{ GHz}]$  frequency range: in particular, the analysis is carried out by exciting the structure with a lumped port, injecting a default  $0 \text{ dBm}$  power for a series  $50 \Omega$  impedance generator.

### $E$ and $H$ -Fields

In order to verify the correctness of such a frequency simulation, it is first possible to have a look on the fields propagating inside the structure. In particular, in Figure 4.9 it is reported the magnitude of electric and magnetic fields at the  $z = 0$  silicon top surface for  $f = 10 \text{ GHz}$ : such plots are realized only for the London Complex Conductivity model, which considers the most of the physical parameters for superconductivity. It is possible to clearly notice that the highest  $E$ -field values are correctly located at the outermost edges of the pads and all along a single spiral line, meaning that the maximum intensity of nearly  $E_{MAX} \simeq 0,25 \text{ MV/m}$  is placed inside the gap of the 2-turns inductor. On the other hand, the magnetic field (maximum for  $H_{MAX} \simeq 50 \text{ mA/m}$ ) is mainly located along a 2-turns spiral connecting the pads: this result basically confirms that the magnetic field is propagating inside the superconducting material, since its thickness is smaller than the London penetration depth (*i.e.*  $t = 60 \text{ nm} < 100 \text{ nm} = \lambda_L$ ).

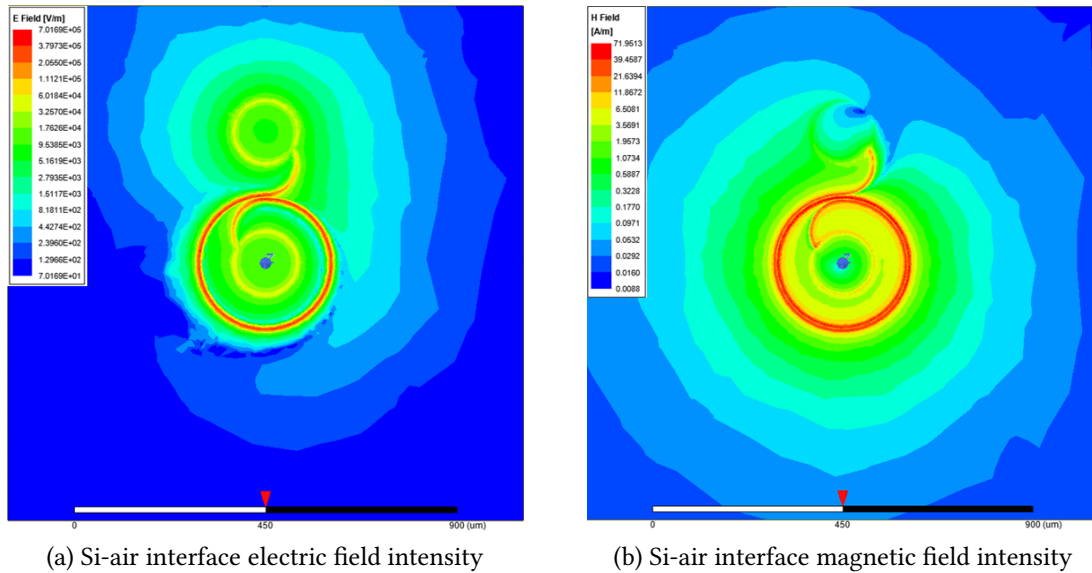
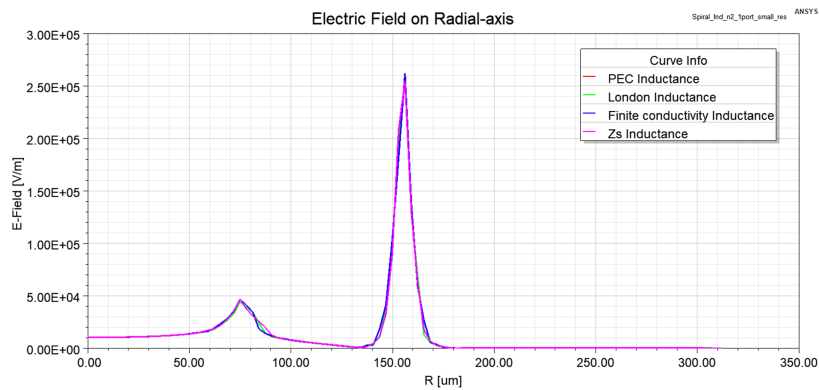


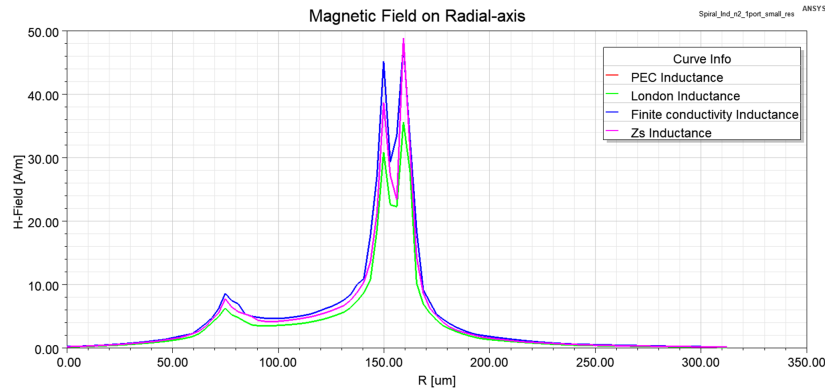
Figure 4.9: 2D top view of the propagating fields of the 2-turns Nb inductor ( $P_{in} = 0 \text{ dBm}$ )



Moreover, by defining a plot-line starting at the center of the internal pad and running on the horizontal  $y$ -axis, from  $y_{in} = 0$  to  $y_{fin} = R_i + W_o + R_i$ , on the top silicon surface ( $z = 0$ ), it is possible to obtain the 1D fields plots presented in Figure 4.10, considering all the 4 material models. Looking at the radial electric field, one can clearly distinguish the single peak, related to the inter-turns gap, located just after the internal inductor radius  $y = 150 \mu\text{m}$ . For what it concerns the  $H$ -field, the two maximum peaks are placed at the 2-turns, while a minimum value is present inside the gap, confirming the fact that the current is circulating in the whole cross-section of the Nb line. However, it is also important to notice that all the superconductivity models are able to predict the spatial propagation of the generated fields, well reproducing the high AC conductivity of superconducting Nb line.



(a) 1D radial plot of the electric field



(b) 1D radial plot of the magnetic field

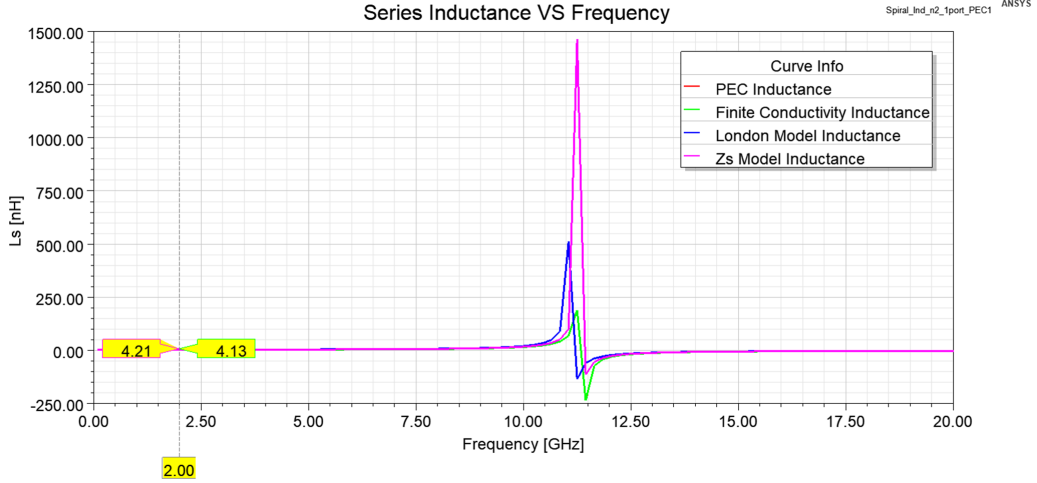
Figure 4.10: 2-turns inductor 1D fields for the 4 material models ( $P_{in} = 0 \text{ dBm}$ )

### Planar Inductor Parameters

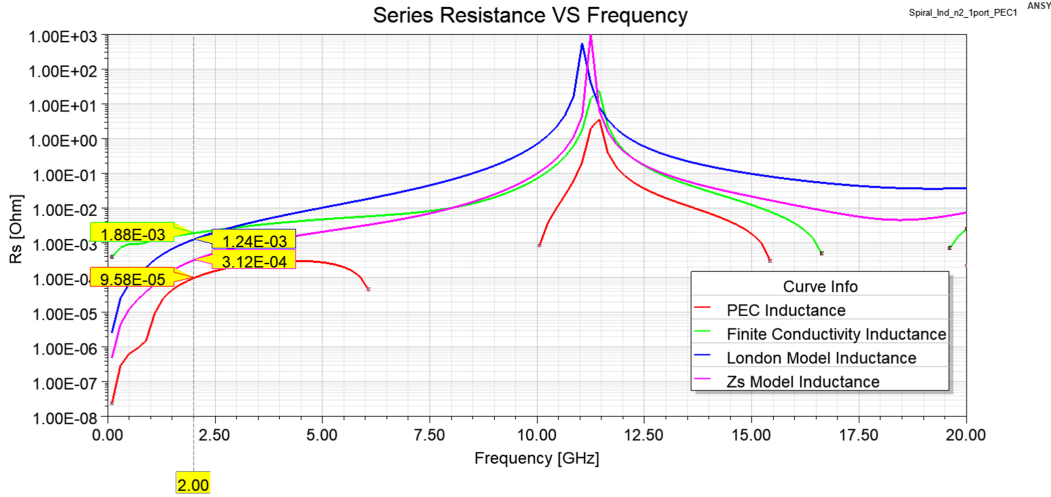
By recalling that a 1-port simulation is performed, it is possible to extract the lumped parameters of the superconducting inductor, with respect to the model described in

Figure 4.7, by exploiting the structure impedance  $Z_{11} = R_S + j\omega L_S$  calculated by Ansys® HFSS®. In so doing, as reported in [24], the series inductance  $L_S$ , the parasitic series resistance  $R_S$  and the inductor quality factor  $Q$  can be determined as:

$$R_S = \Re\{Z_{11}\} \quad L_S = \frac{\Im\{Z_{11}\}}{2\pi f} \quad Q = \frac{2\pi f L_S}{R_S}$$



(a) Series inductance frequency behaviour



(b) Series resistance frequency behaviour

Figure 4.11: Lumped series inductance and resistance of the 2-turns Nb inductor

In Figure 4.11(a) it is reported the behaviour of the inductor for all the four models: since the geometrical inductance  $L_S \simeq 3,4 \text{ nH}$  is the predominant term, all the cases are able to predict a value in agreement to the design one, nearly  $4 \text{ nH}$  at  $2 \text{ GHz}$ . Moreover,

a resonance is clearly visible between 11,5 GHz and 12 GHz, due to the appearance of the parasitic  $C_P$  term, which makes the inductor to behave like a capacitance. On the other hand, Figure 4.11(b) presents the behaviour of the parasitic series resistance, clearly showing that PEC and Finite Conductivity models are not able to accurately predict the behaviour of such a quantity over a broadband frequency range.<sup>14</sup> In particular, the plot is realized on a y-semi-logarithmic axis, in order to show the increase of the resistance over different orders of magnitudes, starting from some  $\mu\Omega$  low frequency values up to a 1 k $\Omega$  peak at the resonance condition, as reported in literature (see [52]). In this sense, London and  $Z_S$  models are perfectly able to provide a reasonable behaviour of the parasitic resistance over the whole range of frequencies, with a mismatch probably due to the different nature of the models: the complex conductivity one, actually, considers a bulky 3D material, while the surface impedance one deals with a 2D-based geometry.

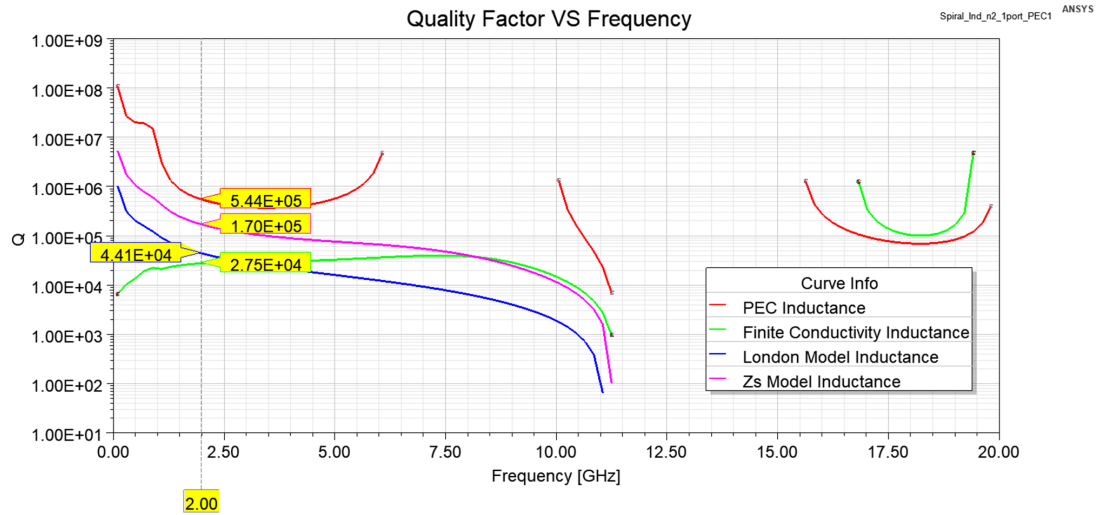


Figure 4.12: Quality factor of the 2-turns Nb inductor

The behaviour of the quality factor is reported in Figure 4.12, where it is possible to see, once again, that the two physical superconductivity models describes in a reasonable way the properties of the inductor, while PEC and Finite Conductivity models are affected by too high numerical inaccuracies. In particular, at 2 GHz, London and  $Z_S$  models respectively provide a quality factor of  $Q_{London} \simeq 4,4 \times 10^4$  and  $Q_{Z_S} \simeq 1,7 \times 10^5$ , before turning negative at the resonance, because of the predominance of the parasitic capacitance effects. Even if the order of magnitude is similar to the one found in literature (see [52]), an important mismatch between the two models is present. This is probably due to the poor accuracy achieved by a whole frequency range simulation of the structure,

<sup>14</sup>As a matter of fact, the discontinuity regions for the two models are basically defining negative resistance values, completely wrong results due to numerical errors introduced when dealing with such high conductivities.

basically introducing numerical errors in the extraction of the inductor resistance<sup>15</sup> and, therefore, also in the evaluation of the quality factor: such a broadband methodology is therefore, not suitable for a precise simulation of the superconducting inductor.

### 4.3.3 Simulation Results of the 30-Turns Final Version Inductor

Once having proved the validity of the superconductivity models in the description of the properties of a simpler Nb inductor, it is now possible to proceed to the discussion of the simulation results concerning the 30-turns final inductor. The HFSS<sup>®</sup> geometry of such a structure is shown in Figure 4.13.

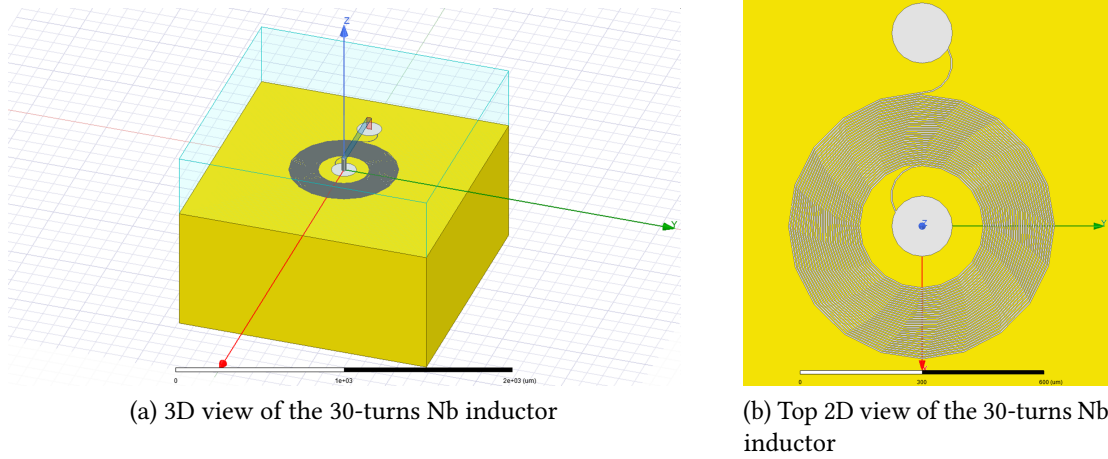


Figure 4.13: 30-turns final Nb inductor

In particular, since the component is far more complex than the previous one, involving a very dense meshing of the whole structure,<sup>16</sup> only some single-points simulations will be carried out, over a narrower [50 MHz; 1 GHz] range, in order to reduce the simulation time. As a matter of fact, since the number of turns is drastically increasing, an overall increase in the turn-to-turn parasitic capacitance will take place, for which it is expected a resonance frequency shift below 1 GHz: it is even, therefore, useless to simulate such an inductor over the complete previous broadband frequency range.<sup>17</sup>

<sup>15</sup>As a matter of fact, the  $S_{11}$  parameter is found to be in the order of  $-10 \times 10^{-6} dB$  (negligible losses for a superconductor), at the limit of solver precision, but still expected for a superconducting material.

<sup>16</sup>Moreover, a whole frequency simulation has been shown to fail for an overall accurate analysis: this actually suggests to proceed with single frequencies analyses.

<sup>17</sup>Only three models will be analysed, namely the London Complex Conductivity, the Surface Impedance and the PEC, this latter kept only as comparison condition for the two more accurate ones.

### *E* and *H*-Fields

First of all, Figure 4.14 presents the top and the cross-sectional view of the electric and magnetic field intensities, for the London Complex Conductivity model at  $100\text{ MHz}$  and  $0\text{ dBm}$  injected power, being possible to see the 3D propagation of the fields all over the system. In particular, the maximum intensities are located in the presence of the 30 Nb turns.<sup>18</sup>

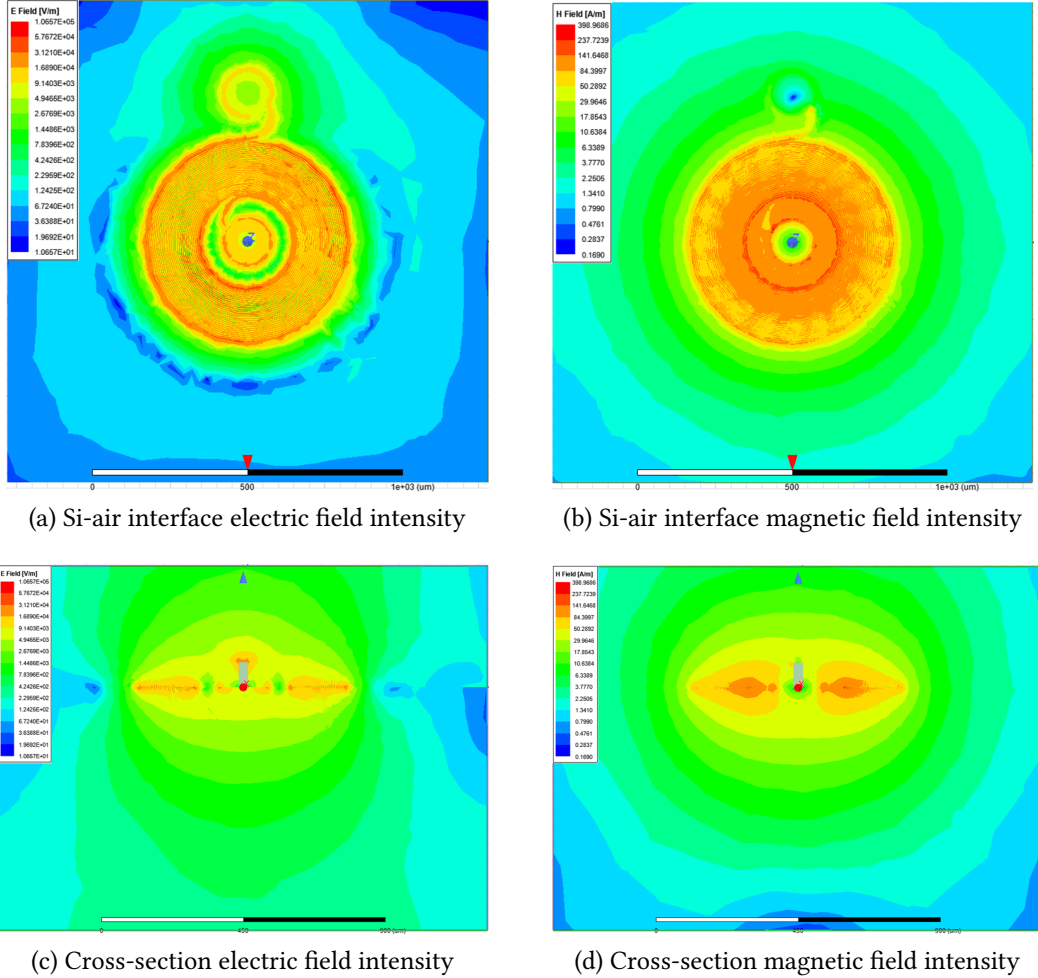
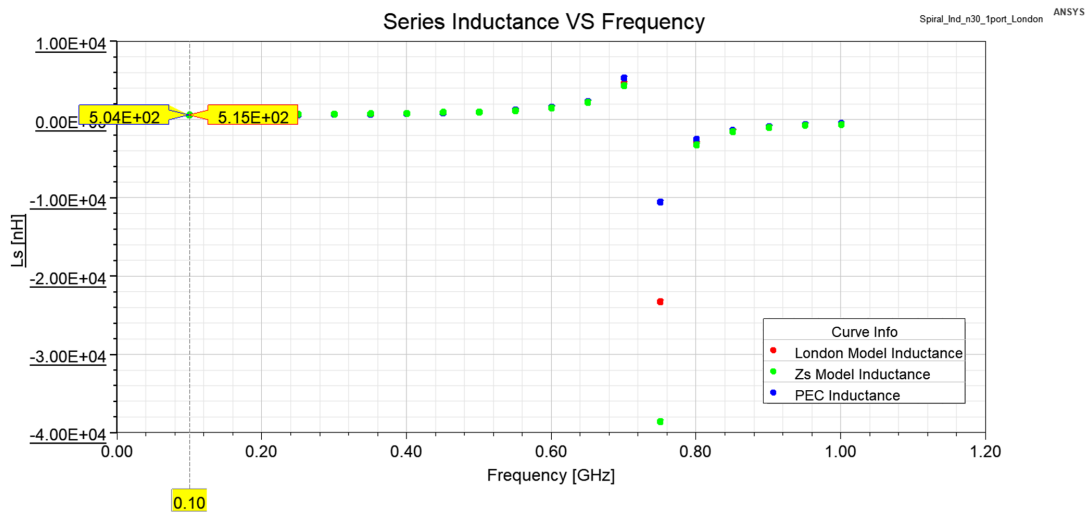


Figure 4.14: 2D field views for the 30-turns Nb inductor ( $P_{in} = 0\text{ dBm}$ )

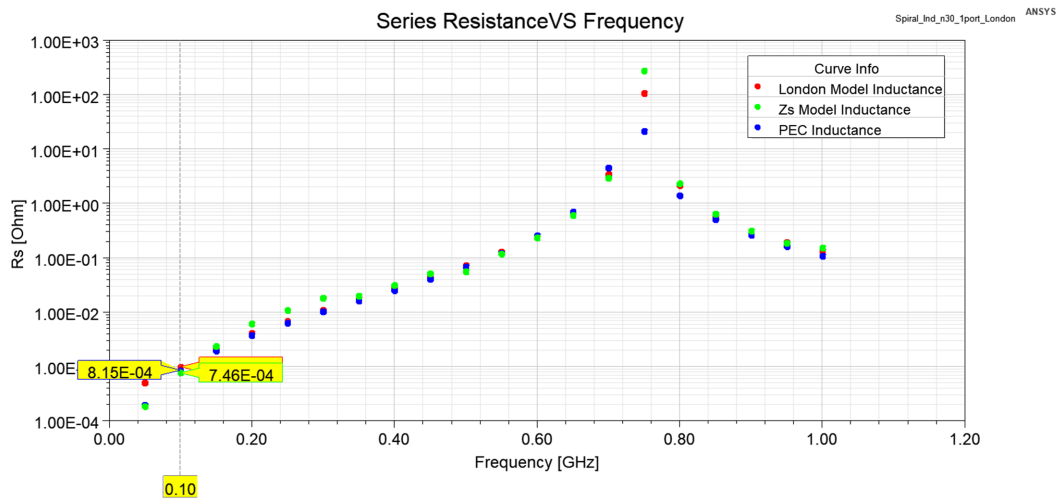
<sup>18</sup>It is important to notice that for the electric field a small perturbation is generated by the presence of the shorting PE boundary. However, as explained in appendix §C.2, such an effect is negligible with respect to the overall field calculations, since a sufficient high port height is considered for accurate convergence on the inductor lumped parameters. On the other hand, it is possible to notice that a certain amount of electric field is collected by the bottom ground plane, meaning that the parasitic capacitance also results from a line-to-ground electric coupling.

### Planar Inductor Parameters

For what it concerns the extraction of the superconducting lumped parameters, in Figure 4.15 are presented the frequency behaviours for the series inductance and resistance. In particular, as reported in Table 4.3, it is possible to see that at 100 MHz the calculated inductance is almost equal to the predicted design one  $L_S = L_{c\text{sa}} \simeq 517,64 \text{ nH}$ , diverging at most for a 2,6% in the PEC case. On the other hand, dealing with the parasitic resistance, such a quantity is accounting only for less than 1 mΩ, as expected for a superconducting material at high frequencies.



(a) Series inductance frequency behaviour



(b) Series resistance frequency behaviour

Figure 4.15: Lumped series inductance and resistance of the 30-turns Nb inductor

	London Model	$Z_S$ Model	PEC Model
$L_S$	515,1 nH	514,3 nH	504,2 nH
$R_S$	0,95 m $\Omega$	0,81 m $\Omega$	0,75 m $\Omega$
$Q$	$4,3 \times 10^5$	$3,9 \times 10^5$	$3,4 \times 10^5$

Table 4.3:  $L_S$ ,  $R_S$  and  $Q$  of the 30-turns inductor at 100 MHz

Moreover, for both the previous quantities it is possible to notice the presence of the resonance condition, due to the parasitic capacitance  $C_P$  at nearly 720 MHz, originating an equivalent peak series resistance value in the order of few k $\Omega$ . It is important to stress that, for this final version inductor, as shown in Table 4.3, all the three models provide quality factors in the same order of magnitude: such a situation is probably due to the fact that single frequencies analyses are performed, for which the mesh generation is optimized over each different frequency, certainly leading to a better accuracy with respect to the previous structure.

On the other hand, Figure 4.16 describes the frequency behaviour of the quality factor, calculated from the the series inductance and resistance of the Nb structure, highlighting, once again, the good agreement of all the three models.

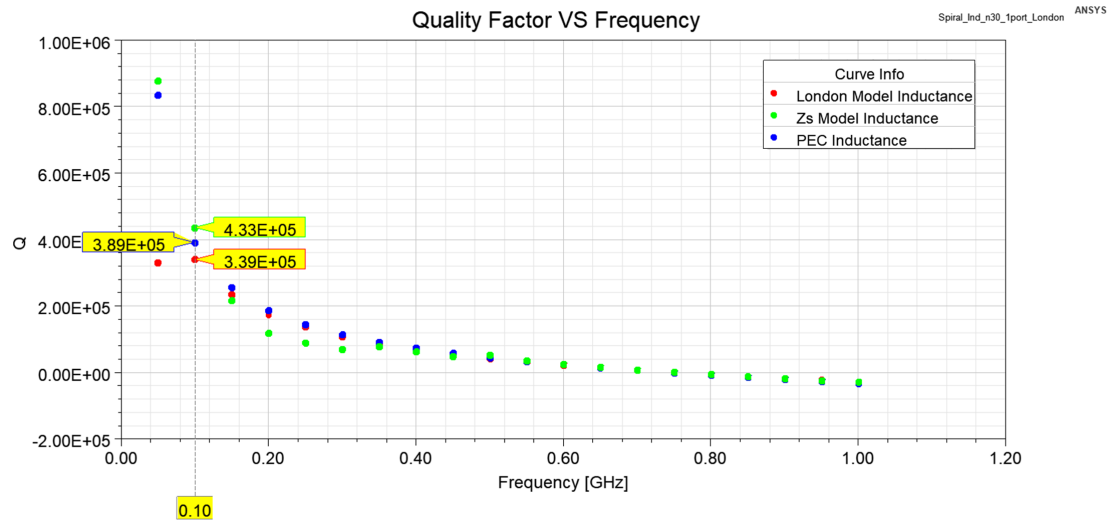


Figure 4.16: Quality factor of the 30-turns Nb inductor

### Extraction of the Parasitic Capacitance

As last analysis, a frequency simulation over the whole [50 MHz; 1 GHz] frequency range is set up by means of the Surface Impedance model (which is the fastest one in terms of computational performances). In so doing, it is possible to precisely measure the

resonance frequency of the corresponding structure and extract the parasitic capacitance exploiting the following formula:

$$f_{res} = \frac{1}{2\pi\sqrt{L_S C_P}}$$

In Table 4.4 are reported the RF extracted values of the 30-turns Nb planar inductor, considering also the extraction of the parasitic capacitance of the component.<sup>19</sup> As it is possible to notice, the prediction of the inductance value  $L_S$  is very accurate, only nearly 0,6% different from the design value, sufficiently high for allowing gate spin sensing in the  $MHz$  range. Furthermore, the quality factor of the structure is predicted to be extremely high, due to the low resistance of the inductor, validating the use of superconducting materials for the implementation of gate reflectometry resonators for the precise measurement of resonance frequency shifts.

$L_S$	$R_S$	$Q$	$f_{res}$	$C_P$
514,3 nH	0,81 mΩ	$3,9 \times 10^5$	715,1 MHz	95,8 fF

Table 4.4: Inductor parameters at 100 MHz for the  $Z_S$  model

## 4.4 Conclusion

Gate reflectometry has shown to be a powerful technique to address single spin readout. In particular the resonance frequency shift caused by a spin-related inter-dots quantum capacitance is a key element for the realization of an RF resonator: in this perspective, the design of the corresponding inductor plays an important role for what it concerns the accuracy in such a dispersive frequency measurement. Moreover, the performances of such a dispersive technique can be drastically improved by recurring to superconducting materials for the realization of such a circuit, making losses on the reflected signal extremely small.

### 4.4.1 Achievements

This chapter has first introduced a simplified description of the main inter-dots mechanism that are currently exploited for implementing the readout of CMOS spin Qubits.

---

<sup>19</sup>In particular, two simulations considering both the presence of the bottom ground and its absence have been carried out, discovering that the resonance frequency does not undergo a significant variation. This result means that the main contribution to the parasitic capacitance comes from the turn-to-turn coupling and the effects of the pads.



Moreover, in a second time, a short explanation of superconductivity and how such an amazing property can be modelled for the design of high-performances HF circuits has been discussed. After this preliminary introduction, the main results concerning the simulation of a planar superconducting inductor for gate reflectometry resonance have been presented, first focusing on a very simple structure, in order to compare the accuracy of several superconductivity models, and then analysing the real final version of such a component.

Considering the results obtained in this work, the benchmark 2-turns inductor allowed to have an idea of the main issues characterizing the designed system. By means of the lumped elements extraction, for such an easier case, the 4 models used to describe Nb superconductivity have been tested, finally discovering that the London Complex Conductivity and the Surface Impedance cases were the most accurate ones, even if a bit more complex, still needing for single-frequencies high-accuracy simulations. When taking into account such models for the simulation of the effective version of the inductor, it has been possible to perform many single-frequencies simulations, allowing to finally extract the value of the series inductance and compare it with the design one. In the end, the extraction of the parallel parasitic capacitance has been carried out, giving an idea of the main turn-to-turn coupling contribution to this quantity.

#### **4.4.2 Future Work**

Even if such an inductor has been deeply analysed, many different aspects still need to be studied and addressed before finally fabricating it for a scalable implementation of spin readout. As a matter of fact, the presence of the double QDs should be considered, at least considering their lumped tunable capacitance load, possibly verifying the effective shift of the resonance frequency for particular spin configurations. Moreover, a more sophisticated model of the superconducting inductor, taking into account critical field and current effects should be set up, basing on technological parameters available from the fabrication processes exploited in the framework of the Grenoble Quantum Silicon collaboration project. In the end, it would be interesting to validate the correct functioning of such a system by means of precise and well defined measurement procedures on a fabricated version of the aforementioned inductor.



# Chapter 5

## General Conclusion

In the end, this work has shown the possibility to study the performances of high-frequencies routing for CMOS quantum bit systems by recurring to dedicated full 3D electromagnetic simulation softwares. In particular, RF control and readout interconnects have been simulated, focusing on the analysis of 1-metal layer structures for addressing single spin Qubits. In this perspective, it has been first studied the case for an On-Chip transmission of microwave signals by exploiting CPW technology. In a second time, a control ESR line for the coherent manipulation of electron spin has been simulated and a geometrical optimization has been performed, assessing its performances over a broadband frequency range. Finally, spin readout issues have been addressed by performing electromagnetic simulations of a superconducting inductor, analysing its resonance behaviour in the framework of gate reflectometry.

### 5.1 Achievements

Many different results have been obtained, assessing the directly On-Chip integration of the aforementioned structures at cryogenic temperatures, for the implementation of a full CMOS-compatible silicon quantum processor. In the following are reported the most important objectives that have been reached during this master thesis project, focusing on 1-metal layer interconnections for routing, control and readout of spin Qubits microwave signals.

- **CPW Transmission Line:** Ansys<sup>®</sup> HFSS<sup>®</sup> software has been exploited in order to simulate the electromagnetic behaviour of a Coplanar Waveguide transmission line for HF On-Chip routing. In particular, it has been possible to design such a structure for an almost  $50 \Omega$  impedance matching condition, verifying the correct propagation of a single Quasi-TEM mode all along a broadband frequency range. Moreover, by recurring to transmission line theory, the *RLC* line parameters have been extracted, contributing to describe the low insertion loss levels of the CPW geometry.

- **ESR Control Line:** An Electron Spin Resonance structure for the coherent control of QDs spin has been designed and simulated by means of CST Studio Suite<sup>®</sup> software. As a matter of fact, a first trial structure has been analysed, in order to obtain a comparison with literature results and, then, a series of optimization simulations have been performed in order to consider a structure respecting the low-temperature physical constraints of such a device, for fast and coherent spin manipulation. An optimized version of the aforementioned line has been, therefore, simulated with high accuracy levels, allowing to verify the presence of a Max- $B$ -field and a min- $E$ -field at the nano-antenna location; finally, the  $RLC$  parameters have been extracted, discovering the limiting resonance frequency for the correct use of the structure and calculating the power dissipation, respecting the few  $\mu W$  constraint imposed by Qubits cryogenic working conditions.
- **Superconducting Readout Inductor:** In the framework of gate reflectometry, the design of a planar spiral inductor has been simulated recurring to Ansys<sup>®</sup> HFSS<sup>®</sup>. In particular, by exploiting Nb superconductivity, it has been possible to fully satisfy the constraints both on a high inductance value for  $MHz$  spin gate sensing and on a high quality factor, for increasing precision in the measurement of the spin-induced resonance frequency shift. For instance, a first benchmark 2-turns inductor has been tested, in order to understand the main issues of such a complex electromagnetic simulation and assess the validity of HF models for superconductivity. In the end, the designed 30-turns inductor has been fully analysed, extracting its  $L_S$  and  $Q$  with high accuracy and evaluating its lumped elements model.

## 5.2 Future Perspectives

Even if this work has been focused on the investigation of the performances of single metallization layer structures for the CMOS integrated control and readout of spin Qubits, many further aspects still need to be addressed for the implementation of a scalable architecture able to address many Qubits. First of all, interconnect networks of growing complexity (2D and 3D) should be analysed, recurring to the methodology discussed in this work. Moreover, concerning coherent control, other mechanisms, such as Electric-Dipole Spin Resonance, should be considered, assessing advantages and drawbacks of different spin manipulation tools for implementing quantum gates. On the other hand, the readout inductor previously described could be analysed more in deep, considering also the presence of the variable impedance load of QDs gate connection and providing a design optimization for reaching higher and higher accuracy in the measurement of the spin state-dependent resonance frequency. In the end, all the structures simulated during this internship should be experimentally tested, in order to validate their functioning and further investigate their electromagnetic properties.

# Appendices



# Appendix A

## Transmission Coplanar Waveguide Simulation

### A.1 Port Sizing for Line Impedance Convergence

As reported on Ansys® HFSS® documentation, a preliminary study regarding the dimensions of the waveguide ports must be carried out. As a matter of fact, HFSS® solves Maxwell's equations at the excitation ports in order to obtain a stable configuration of the fields to propagate, then, on the remaining 3D structure: it is, therefore, important to correctly find the values for  $W_{port}$  and  $H_{port}$  dimensions (see Figure A.1).

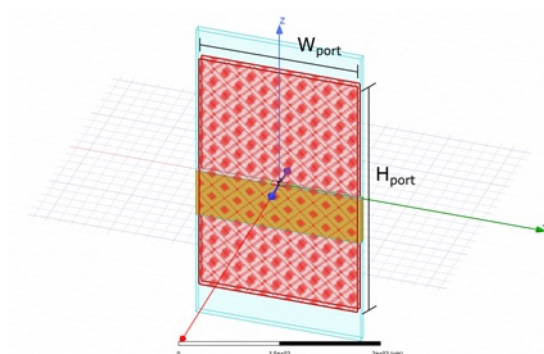
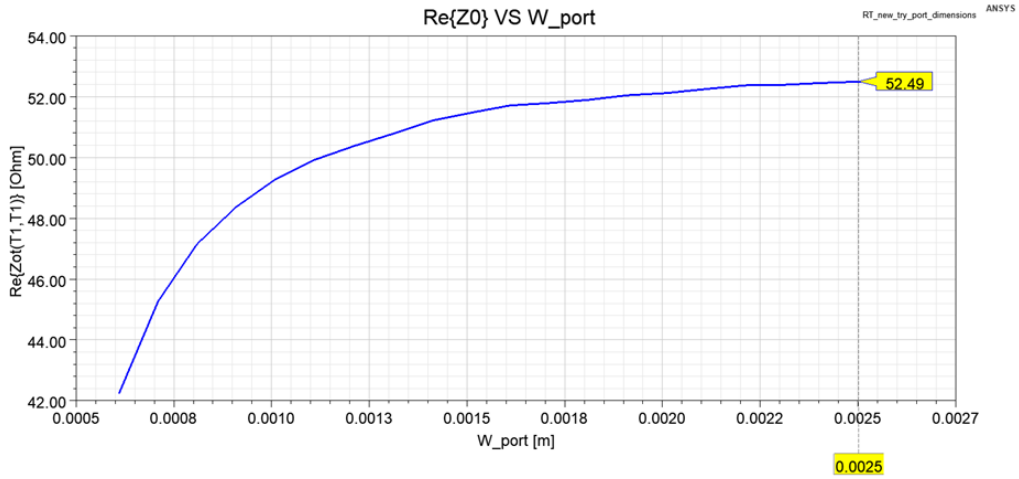


Figure A.1: Wave port dimensions on 3D CPW structure

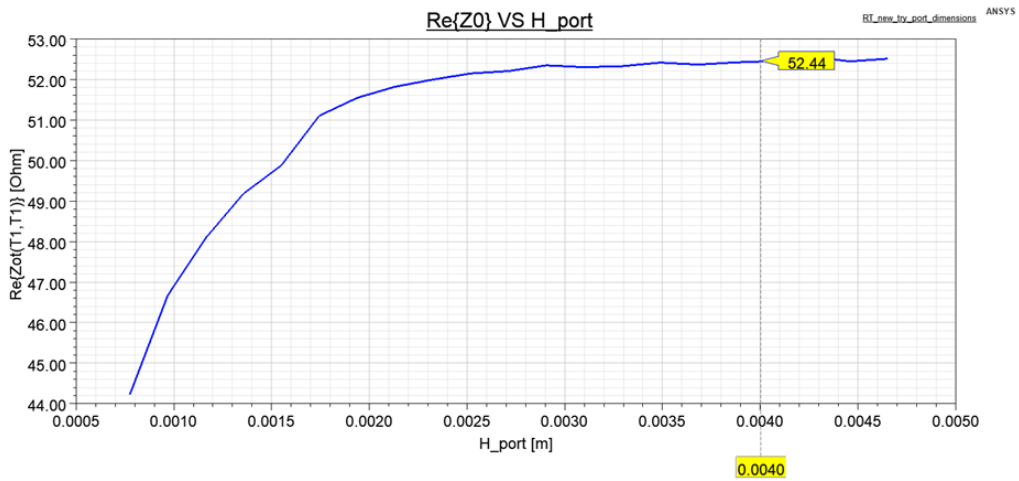
In particular, HFSS® documentation strongly suggests, for considering enough electromagnetic field at the excitation source, to recur to the following guidelines:

$$\begin{cases} W_{port} > 3(w_l + 2w_g) \\ H_{port} > 4h \end{cases}$$

By considering such restrictions, two sweep analyses are performed at  $10\text{ GHz}$  on  $W_{port}$  and  $H_{port}$ , finally getting the results reported in Figure 2.3, from which it is possible to notice that  $W_{port} = 2,5\text{ mm}$  and  $H_{port} = 4\text{ mm}$  guarantee a sufficient convergence for the line impedance calculation to almost  $52\ \Omega$ .



(a) Line impedance calculation with  $W_{port}$  sweep



(b) Line impedance calculation with  $H_{port}$  sweep

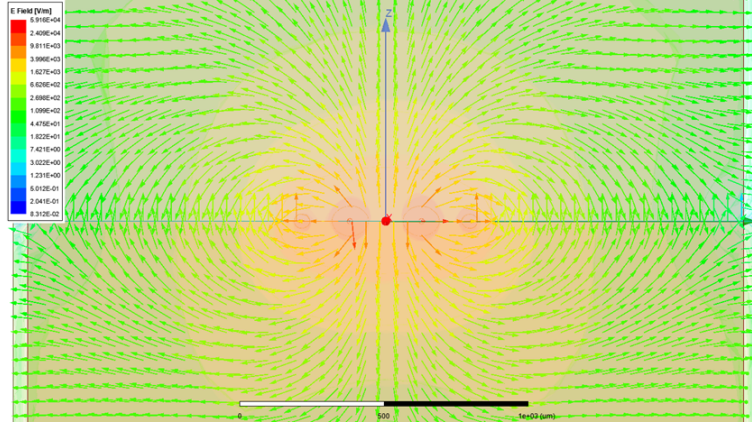
Figure A.2: Waveport dimensions optimization

## A.2 Quasi-TEM Field Distribution at CPW Port

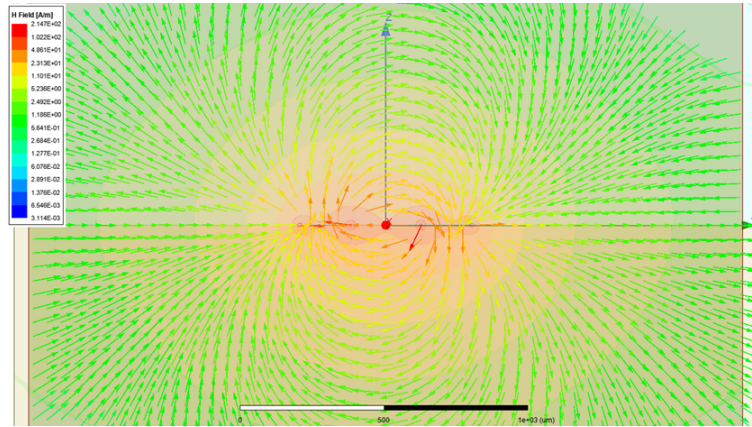
Figure A.3 presents the  $E$  and  $H$ -fields configuration at the wave port for  $f = 10\text{ GHz}$ . As it is possible to notice, the electric field correctly leaves the central signal line, being collected in a symmetric way by the two surrounding ground lines, while the magnetic



field envelops the central conductor, in a clockwise orientation, according to the direction of the injected excitation current. Moreover, the reader should easily notice that the most of the electromagnetic field is collected by the ground lines inside the framework of the wave port, which, actually, highlights the correctness of the wave port dimensioning procedure for fields calculation.



(a) Electric field at the wave port location



(b) Magnetic field at the wave port location

Figure A.3:  $E$  and  $H$  fields at the excitation port for  $10\text{ GHz}$  ( $P_{in} = 0\text{ dBm}$ )

### A.3 Conversion Relations for $S$ , $ABCD$ and $Z$ Matrices

Considering a 2-ports network, whose ports are both referred to the same real impedance  $Z_0$ , it is possible to demonstrate that its electronic system can be represented both by its  $S$  scattering matrix and its  $Z$  impedance matrix. As a matter of fact, as reported in [24], the conversion between  $S$  and  $Z$ -parameters can be realized by recurring to the

following relations:<sup>1</sup>

$$S_{11} = \frac{(Z_{11} - Z_0)(Z_{22} + Z_0) - Z_{12}Z_{21}}{\Delta Z}$$

$$S_{12} = 2 \frac{Z_{12}Z_0}{\Delta Z}$$

$$S_{21} = 2 \frac{Z_{21}Z_0}{\Delta Z}$$

$$S_{22} = \frac{(Z_{11} + Z_0)(Z_{22} - Z_0) - Z_{12}Z_{21}}{\Delta Z}$$

where  $\Delta Z = (Z_{11} + Z_0)(Z_{22} + Z_0) - Z_{12}Z_{21}$ .

On the other hand, also  $ABCD$  matrix can be linked to the scattering  $S$ -parameters, by means of the following relations (as in the previous case, refer to [24] for the complete expressions):

$$A = \frac{(1 + S_{11})(1 - S_{22}) + S_{12}S_{21}}{2S_{21}}$$

$$B = Z_0 \frac{(1 + S_{11})(1 + S_{22}) - S_{12}S_{21}}{2S_{21}}$$

$$C = \frac{1}{Z_0} \frac{(1 - S_{11})(1 - S_{22}) - S_{12}S_{21}}{2S_{21}}$$

$$D = \frac{(1 - S_{11})(1 + S_{22}) + S_{12}S_{21}}{2S_{21}}$$

## A.4 Linking Expressions Between $ABCD$ and Line Parameters

Considering a general transmission line (*i.e.* a coaxial cable, a metallic rectangular waveguide, a CPW and so far and so on), whose total length is  $l$ , it is possible to express its 2-ports  $ABCD$  matrix in terms of its propagation constant  $\gamma$  and characteristic line impedance  $Z_C$ . As a matter of fact, referring to [29], such quantities are linked in the following way:

$$A = D = \cosh(\gamma l)$$

$$B = Z_C \cdot \sinh(\gamma l)$$

$$C = \frac{1}{Z_C} \cdot \sinh(\gamma l)$$

---

<sup>1</sup>The inverse relations have not been exploited in this work; however, the interested reader can find them in [24].

In particular, from such relations it is possible to extract the transmission line parameters as:

$$\gamma = \frac{\text{acosh}(A)}{l}$$

$$Z_C = \frac{B}{\sinh(\gamma l)}$$

In so doing, it is possible to fully characterise the transmission line in terms of its characteristic parameters: such a method allows, therefore, to link together the electronic matrix-based description of a system to its microwave model.



# Appendix B

## ESR Control Line Simulation

### B.1 Derivation of the Rabi Spin Precession Frequency

In this section it will be completely reported the demonstration for the Rabi precession of an electron spin under the application of a static and a dynamic magnetic fields. In particular, it will be shown that this specific combined electromagnetic action finally results on a spin rotation from up to down states, or vice versa.

First of all, in the case in which an electron is placed in a space region in which both a static  $\mathbf{B}_0(\mathbf{r}) = B_0\hat{\mathbf{z}}$  and a dynamic  $\mathbf{B}_1(\mathbf{r}, t) = B_1 \cos(\omega t)\hat{\mathbf{x}}$  are applied perpendicularly to each others, its Hamiltonian, expressed in the lab framework, is defined as:

$$H(t) = \frac{1}{2}\hbar\gamma(\mathbf{B}_0 + \mathbf{B}_1) \cdot \boldsymbol{\sigma} = \frac{1}{2}\hbar\gamma(B_0\sigma_z + B_1 \cos(\omega t)\sigma_x) \quad (\text{B.1.0.1})$$

Since, generally, such an Hamiltonian does not commute for two different time instants (*i.e.*  $[H(t_1), H(t_2)] \neq 0$ ), it is not possible to apply the propagator formula for the time evolution operator  $U(t)$ , as it has been done in §3.2.1: as reported in [33], actually, a new strategy has to be adopted.

In particular, it is necessary to redefine the wavefunction in the Larmor frequency rotating framework:

$$|\psi'(t)\rangle = e^{j\omega_L\sigma_z t/2} |\psi(t)\rangle$$

Applying Schrödinger equation to such a wavefunction, it is possible to get the Hamiltonian  $H'(t)$ , defined in the rotating framework

$$\begin{aligned}
 j\hbar \frac{d}{dt} |\psi'(t)\rangle &= j\hbar \cdot \frac{j\omega_L \sigma_z}{2} |\psi'(t)\rangle + e^{j\omega_L \sigma_z t/2} \cdot j\hbar \frac{d}{dt} |\psi(t)\rangle \\
 &= -\frac{\hbar\omega_L \sigma_z}{2} |\psi'(t)\rangle + e^{j\omega_L \sigma_z t/2} H(t) |\psi(t)\rangle \\
 &= -\frac{\hbar\omega_L \sigma_z}{2} |\psi'(t)\rangle + e^{j\omega_L \sigma_z t/2} H(t) e^{-j\omega_L \sigma_z t/2} e^{j\omega_L \sigma_z t/2} |\psi(t)\rangle \\
 &= \left( -\frac{\hbar\omega_L \sigma_z}{2} + e^{j\omega_L \sigma_z t/2} H(t) e^{-j\omega_L \sigma_z t/2} \right) |\psi'(t)\rangle \\
 &= H'(t) |\psi'(t)\rangle
 \end{aligned}$$

and, substituting the lab framework Hamiltonian defined in Equation B.1.0.1, remembering that  $\omega_L = \gamma B_0$ , it is possible to get the following result:

$$\begin{aligned}
 H'(t) &= -\frac{\hbar\omega_L \sigma_z}{2} + \frac{1}{2} \hbar\gamma e^{j\omega_L \sigma_z t/2} (B_0 \sigma_z + B_1 \cos(\omega t) \sigma_x) e^{-j\omega_L \sigma_z t/2} \\
 &= \frac{1}{2} \hbar\gamma e^{j\omega_L \sigma_z t/2} B_1 \cos(\omega t) \sigma_x e^{-j\omega_L \sigma_z t/2}
 \end{aligned} \tag{B.1.0.2}$$

At this point, recalling the matrix expressions in Equation 3.2.1.1, it is useful to define Pauli raising and lowering operators  $\sigma_{\pm} = (\sigma_x + j\sigma_y)/2$ . Once having introduced these new operators,<sup>1</sup> the dynamic field can be rewritten in terms of two counter-rotating waves:

$$\begin{aligned}
 B_1 \cos(\omega t) \sigma_x &= \frac{B_1}{2} ((\cos(\omega t) \sigma_x + \sin(\omega t) \sigma_y) + (\cos(\omega t) \sigma_x - \sin(\omega t) \sigma_y)) \\
 &= B_1 ((e^{-j\omega t} \sigma_+ + e^{j\omega t} \sigma_-) + (e^{j\omega t} \sigma_+ + e^{-j\omega t} \sigma_-))
 \end{aligned} \tag{B.1.0.3}$$

By substituting Equation B.1.0.3 into Equation B.1.0.2 and recalling the  $\sigma_z$  matrix property 3.2.1.4, it is possible to re-elaborate the expression of the rotating framework Hamiltonian in order to get the following result:

$$\begin{aligned}
 H'(t) &= \frac{1}{2} \hbar\gamma e^{j\omega_L \sigma_z t/2} B_1 \cos(\omega t) \sigma_x e^{-j\omega_L \sigma_z t/2} \\
 &= \frac{B_1}{2} \hbar\gamma \left( e^{j\omega_L \sigma_z t/2} ((e^{-j\omega t} \sigma_+ + e^{j\omega t} \sigma_-) + (e^{j\omega t} \sigma_+ + e^{-j\omega t} \sigma_-)) e^{-j\omega_L \sigma_z t/2} \right) \\
 &= \frac{B_1}{2} \hbar\gamma \left( ((e^{-j(\omega-\omega_L)t} \sigma_+ + e^{j(\omega-\omega_L)t} \sigma_-) + (e^{j(\omega+\omega_L)t} \sigma_+ + e^{-j(\omega+\omega_L)t} \sigma_-)) \right) \\
 &= \frac{B_1}{2} \hbar\gamma \left( (\sigma_+ + \sigma_-) + (e^{2j\omega_L t} \sigma_+ + e^{-2j\omega_L t} \sigma_-) \right) \quad \text{for } \omega = \omega_L
 \end{aligned}$$

<sup>1</sup>Such a quantization in terms of raising and lowering spin operators mainly corresponds to the decomposition of the polarized  $B_1$  field into two counter-rotating waves: such an approximation is well-known in HF electromagnetism, naming rotating wave approximation (RWA).

Recurring to the rotating wave approximation, it is possible to demonstrate (see [33]) that the second term introduces an oscillation which is far faster than the first one, resulting in a negligible effect for the spin dynamics. Therefore, the rotating framework Hamiltonian can be finally expressed in the simplified form

$$H'(t) \simeq H' = \frac{B_1}{2} \hbar \gamma (\sigma_+ + \sigma_-) = \frac{B_1}{2} \hbar \gamma \sigma_x \quad (\text{B.1.0.4})$$

Such an expression is essentially time-independent and, therefore, it is possible to apply the propagator formula on the time evolution operator

$$U'(t) = e^{-\frac{j}{\hbar} \int_0^t H'(t') dt'} = e^{-j B_1 \gamma \sigma_x t / 2}$$

for the state  $|\psi'(t)\rangle$ . In this case the calculation becomes quite longer and trickier, involving the change of coordinates into the  $|+\rangle$  and  $|-\rangle$  orthonormal basis: for this reason, the remaining part of the demonstration is omitted, being conceptually equal to the one presented in §3.2.1.

In the end, the Larmor resonance condition for the application of the dynamic field  $\mathbf{B}_1(\mathbf{r}, t)$  is a key factor for discovering that, under these particular conditions, the spin in the rotating framework is made to precess also around the x-axis at a frequency  $\omega_R = \gamma B_1/2$  known as Rabi frequency. This last result concludes the demonstration that the combined application of a static and a dynamic magnetic fields, perpendicularly to each others, has the effect of a whole up-down rotation, due to the precession of the spin around the two magnetic axes.

## B.2 Simulation Setup

Once having defined the global geometry of the ESR line, it is necessary to proceed to the definition of meshing techniques for FEM calculations and the source of excitation for the CPW port. Such aspects are crucial for well describing the system and be sure that the software can easily solve Maxwell's equation all over the structure.

### B.2.1 Meshing Techniques and Aluminum Thick-Sheet Definition

First of all, because of the high aspect ratio of the designed structure, it is important to pay attention to the mesh generation. CST<sup>®</sup> Microwave Studio is, actually, able to automatically detect regions of interest and refine the mesh around these areas; however, a good initial mesh must be provided, especially in the short-circuit surroundings. To do so, a virtual object can be created over the microwave antenna and its meshing can be manually set to be finer with respect to the remaining structure. In Figure B.1 it is possible to see the final result for the meshing of the whole structure, having also a zoom on the finer mesh region surrounding the ESR antenna.

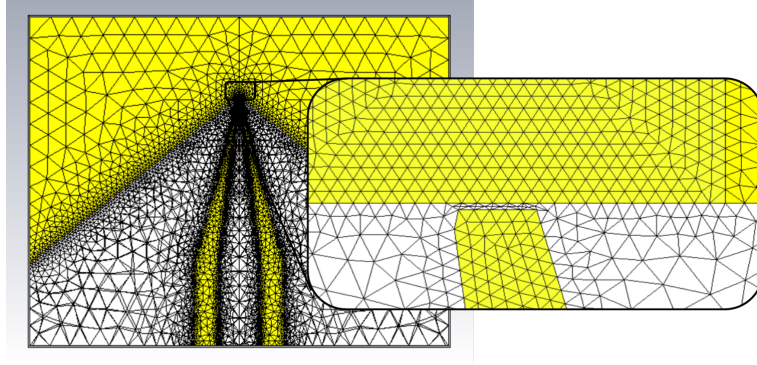


Figure B.1: Mesh generation for the whole ESR structure

Furthermore, a smart way to additionally optimize simulation time is by recurring to the definition of Al CPW as a finite-thickness sheet, simulating, therefore, only a 2D object which is actually considered as a 3D one. Thanks to the macros presented in CST<sup>®</sup> Microwave Studio, it is possible to define the metallic 3D-structure as a tabulated impedance sheet, specifying the conductivity of aluminum<sup>2</sup>  $\sigma_{Al} \simeq 14,29 \times 10^7 \text{ S/m}$  and the thickness of the metallic line  $t = 100 \text{ nm}$ .

This particular method also allows to consider the fact that the CPW thickness is considerably smaller than the minimum skin depth for the simulation frequency range (*i.e.*  $\delta_{60 \text{ GHz}} = (\pi \sigma_{Al} f \mu_0)^{-1/2} \simeq 172 \text{ nm}$ ), meaning that the CPW behaves like a transparent material allowing field propagation inside of it.

## B.2.2 Waveguide Port and Boundary Conditions

As in Ansys<sup>®</sup> HFSS<sup>®</sup>, also in CST<sup>®</sup> Microwave Studio it is important to correctly set the dimensions of the exciting waveguide port. As a matter of fact, if the port is too small, not enough field is considered for the port mode field configuration, while, on the other hand, if the dimensions are too big, extra virtual cavity modes can be excited during the simulation over the  $[100 \text{ MHz}; 60 \text{ GHz}]$  frequency range.

As mentioned by the software documentation, the port width and height should be, respectively, at least  $W_{port} = 3(w_l + 2w_g)$  and  $H_{port} = (w_l + 2w_g)$  (see Figure B.1(a)): in particular, in appendix §B.3, are reported the main results dealing with the preliminary simulations for correctly setting-up the port dimensions and finding the appropriate  $w_g \simeq 148 \mu\text{m}$  for a  $52 \Omega$  line impedance matching.

<sup>2</sup>Such a value is the one reported in [43] for the measured Al conductivity at a nearly 4 K cryogenic temperature. Moreover, it is important to emphasize that, nor in this case neither in the following Al On-Insulators one, the Al line undergoes a superconducting transition, since an external  $\mathbf{B}_0$  higher than the critical field (*i.e.*  $10 \text{ mT}$ , as reported in [41]) is assumed to be applied.



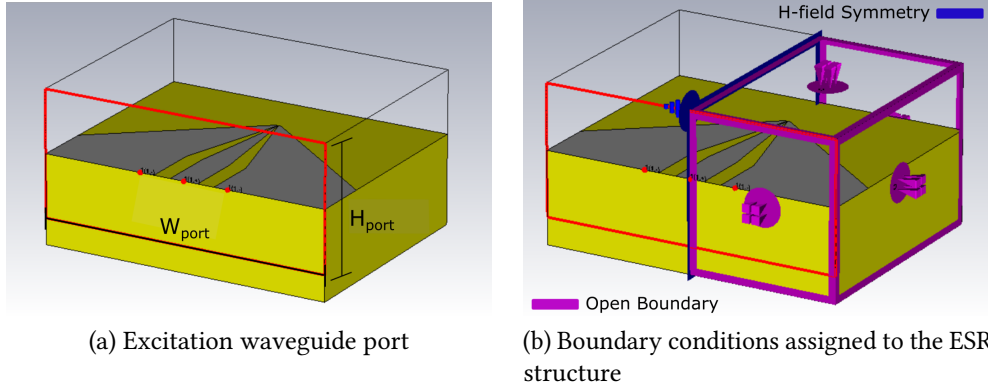


Figure B.2: 3D view of the ESR line, comprising waveguide port and boundaries

Moreover, for this kind of frequency range simulation, a set of open boundaries conditions are applied to the external surfaces of the structure,<sup>3</sup> while an  $H$ -field symmetry is applied to the symmetry  $y$ -plane of the line, in order to halve calculation time. The application of such conditions is illustrated in Figure B.1(b).

## B.3 Wave Port Dimensions

In this section it will be discussed about the main results dealing with the correct dimensioning of the excitation waveguide port. After having first set up  $W_{port} = w_l + 2(w_g + W)$  (i.e. the whole width of the structure) and  $H_{port} = 2(w_l + 2w_g)$ , in order to respect the conditions reported in appendix §B.2.2, it is possible to run a preliminary simulation only at  $10\text{ GHz}$ , by exploiting the *Optimizer* feature of CST<sup>®</sup> Microwave Studio, in order to find the optimal value  $w_g \simeq 148\ \mu\text{m}$  for a  $52\ \Omega$  impedance matching. In a second time, two separated sweeps on  $W_{port}$  and  $H_{port}$  dimensions can be processed, in order to make sure about the convergence for the calculated line impedance at  $10\text{ GHz}$ : the sweeping parameters are shown in Figure B.3.

### B.3.1 $Z_{port}$ Convergence for $W_{port}$

First, the sweep analysis is carried out on  $W_{sweep}$ , making it to linearly increase from  $W_{sweep,in} = w_l/2 + w_g \simeq 273\ \mu\text{m}$ , for a sufficiently large height  $H_{port} = 2(w_l + 2w_g) = 546\ \mu\text{m}$ . Figure B.4(a) shows the result of such a simulation, making evident that the convergence on  $Z_{port}$  is reached for  $W_{port} = 2W_{sweep} = 1,2\text{ mm}$ .

<sup>3</sup>CST<sup>®</sup> open boundaries are essentially equal to HFSS<sup>®</sup> radiation boundaries described in §2.3.1, allowing the fields to indefinitely propagate in space.

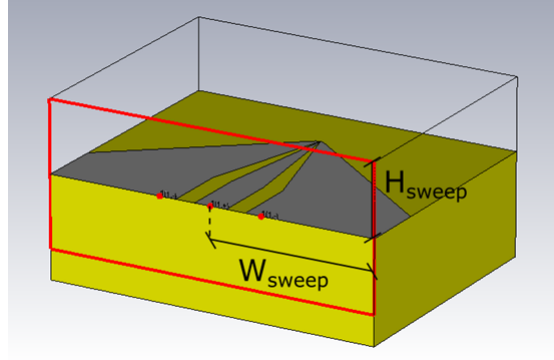


Figure B.3: 3D view of the ESR line, showing the port sweep dimensions

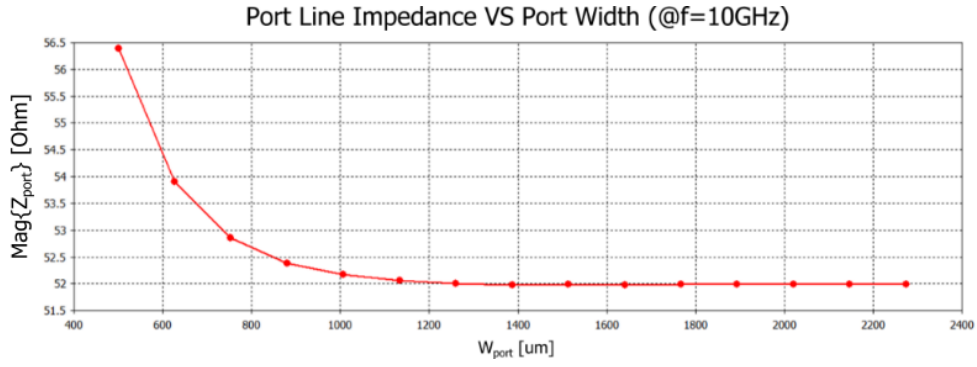
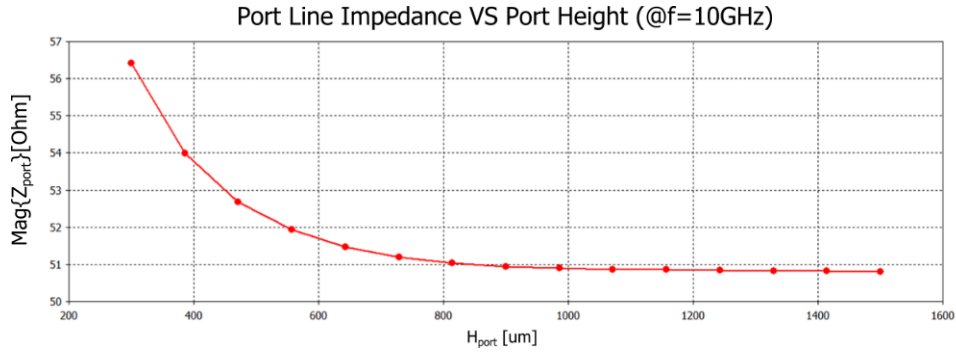

 (a) Line impedance convergence for  $W_{port}$  sweep

 (b) Line impedance convergence for  $H_{port}$  sweep

 Figure B.4: Sweep analysis for calculating optimal port dimensions ( $f = 10 \text{ GHz}$ )

### B.3.2 $Z_{port}$ Convergence for $H_{port}$

On the other hand, the sweep analysis for  $H_{port}$  is carried out fixing  $W_{port} = w_l + 2(W + w_g) \approx 2,5 \text{ mm}$  (i.e. the maximum width of the structure) and starting from  $H_{sweep_{in}} = w_l/2 + w_g = 273 \text{ μm}$ . Looking at Figure B.4(b), it is possible to notice that a good convergence is starting at  $H_{port} = 2H_{sweep} = 1 \text{ mm}$ : however, for this sweep

analysis,  $Z_{port}$  is found to converge to a value of nearly  $51 \Omega$ . Such a result basically means that the port height should be increased for the optimization run extracting the value of  $w_g$ .

Unfortunately, it is not possible to increase  $H_{port}$  further than  $600 \mu m$  since CST will simulate open boundaries considering them as metallic enclosures and, therefore, virtual cavity modes will arise in the frequency range, from nearly  $40 GHz$ , influencing the behaviour of the ESR line. The values for the port dimensioning are therefore set to be

$$\begin{cases} W_{port} = w_l + 2(w_g + W) \simeq 2,5 \text{ mm} \\ H_{port} = 2(w_l + 2w_g) \simeq 546 \mu m \end{cases}$$

remembering that an acceptable 2,2% approximation error is present, due to simulation software issues. Moreover, this error, introduced by the way CST<sup>®</sup> software considers port dimensioning issues, is probably the cause for the mismatch line-to-gap width between the value calculated using HFSS<sup>®</sup> in §2.3.2 and the one obtained recurring to CST<sup>®</sup>.



## Appendix C

# Readout Superconducting Inductor Simulation

### C.1 Planar Inductor Simulation Setup

As already discussed in §4.3.1, the superconducting inductor under analysis is constituted by a 30 turns planar Nb line, whose thickness, metallic width and inter-turns gap are, respectively,  $t = 60 \text{ nm}$ ,  $W_s = 3 \mu\text{m}$  and  $W_g = 3 \mu\text{m}$ . Such a structure is designed to provide a geometrical inductance value of  $L_S \simeq 517 \text{ nH}$  and it is reported in Figure C.1(a), where it is possible to notice also the Nb circular pads used for experimental characterization.

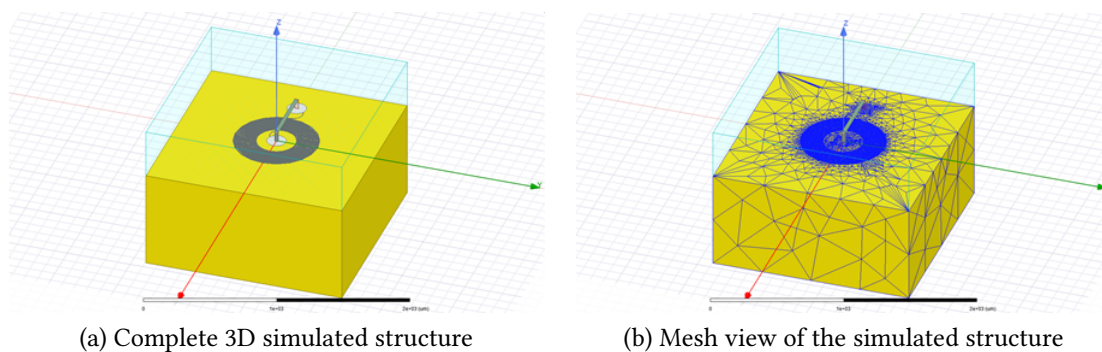


Figure C.1: HFSS<sup>®</sup> 3D view of the planar Nb superconducting inductor

#### C.1.1 Mesh Generation

The first simulation issue that has to be taken into account concerns the mesh of the structure. As a matter of fact, the high aspect ratio between the thickness of the Nb

metallic line and the dimensions of the overall inductor, considering also the high number of turns and spacings, easily make the HFSS<sup>®</sup> meshing to exceed millions of tetrahedrons for a broadband  $GHz$  simulation, exponentially increasing simulation times. However, a good way to overcome such a computational problem is to decrease the accuracy on the  $S$ -parameter calculation ( $\Delta_S = 0.01$ , sufficient for a 1-port simulation of an inductor) and provide an initial seeding mesh to the Nb inductor with a maximum  $20 \mu m$  meshing elements length. In so doing, the mesh is refined for accuracy only at the Nb line (see Figure C.1(b)) and calculation time is drastically reduced, making the simulation over a narrower [ $50 MHz$ ;  $1 GHz$ ] feasible for single frequencies analyses.

### C.1.2 Signal Excitation and Boundaries

Differently from the previous CPW and ESR line simulations, since the inductor must be excited at the interior of the 3D system, a lumped port is applied at one of the two pads, precisely, at the external one. Such a lumped port injects a  $0 dBm$  power with a  $50 \Omega$  generator impedance at the superconducting inductor. Moreover, in order to close the excitation source to the other pad, a PEC cylinder with an height  $h_L$  and a radius  $R_c = R_p/2 = 37,5 \mu m$  is connected to the internal pad and shorted to the lumped port by means of a Perfect Electric (PE) field boundary sheet. In Figure C.2(a) it is reported the excitation apparatus: in red it is shown the rectangular excitation lumped port, while in blue it is reported the PEC cylinder and the PE connecting boundary, which close the circuit by shorting the internal pad and the lumped port.

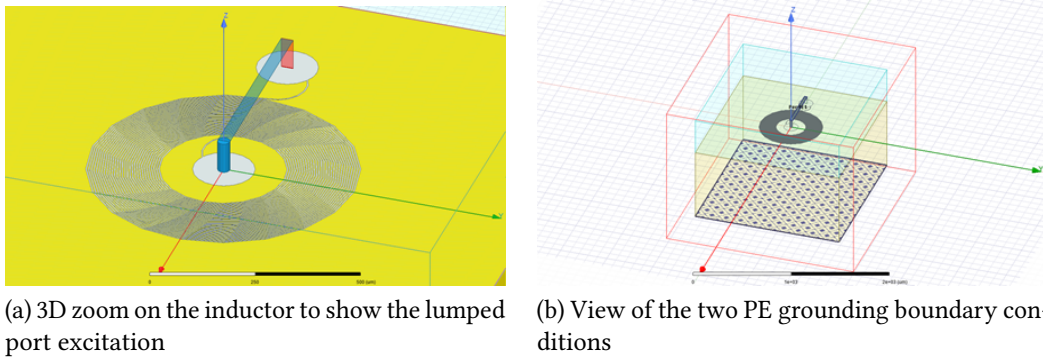


Figure C.2: HFSS<sup>®</sup> 3D view, showing excitation and boundaries

On the other hand, also three boundary conditions are applied to the system under analysis. As a matter of fact, Figure C.2(b) shows two PE boundaries: the first one is the aforementioned shorting condition for correctly connecting the excitation, while a second PE is applied at the bottom of the substrate in order to simulate the presence of a ground reference plane. Finally, also a radiation box is put all around the structure, in order to provide a correct propagation condition for the fields all over the free external space: this latter boundary is shown as the red-edges box surrounding the whole system.

## C.2 Lumped Port Dimensions

In order to provide an accurate calculation of the fields propagating inside the system and the lumped parameters characterizing the Nb inductor, for the benchmark 2-turns case, a preliminary sweep analysis is performed on the height of the lumped port  $h_L$  (see Figure C.3), in order to take into account the influence of the PE shorting boundary.

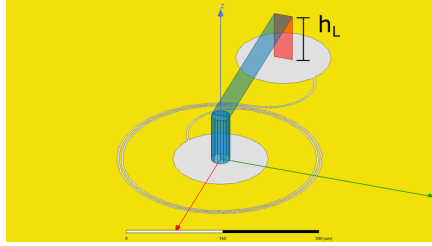


Figure C.3: Zoom on the lumped port excitation for the 2-turns inductor

In particular, the sweep is carried out on a  $10 \mu\text{m}$  to  $100 \mu\text{m}$  range and the following quantities are taken into account for the convergence criteria:

$$R_S = \Re\{Z_{11}\} \quad L_S = \frac{\Im\{Z_{11}\}}{2\pi f} \quad Q = \frac{2\pi f L_S}{R_S}$$

being  $R_S$  and  $L_S$  the series lumped elements describing the inductor, calculated by means of the structure impedance  $Z_{11} = R_S + j\omega L_S$ . On the other hand,  $Q$  is the quality factor of such a series component: it is important for the evaluation of the correct port sizing because it considers both the series resistance and the series inductance of the structure. In this way, it is found a convergence condition on  $Q$  for the port height value of  $h_L = 80 \mu\text{m}$  (see Figure C.4).

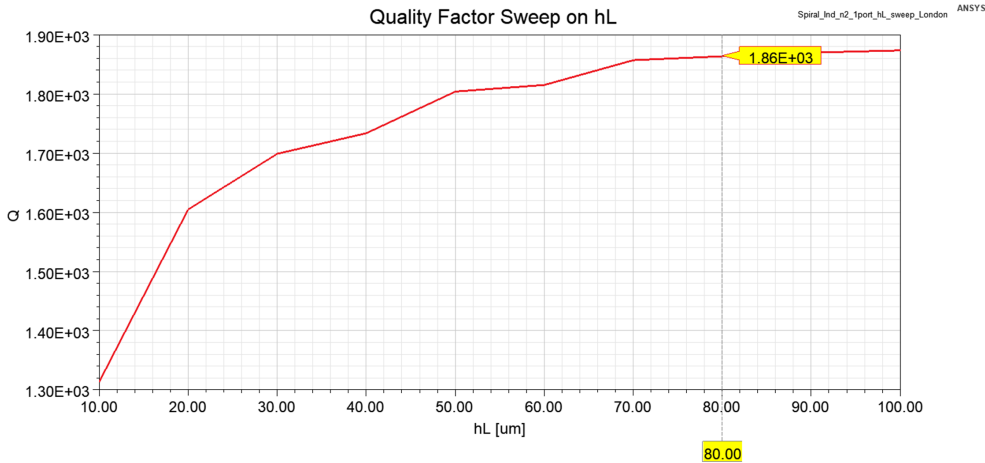


Figure C.4: Convergence criteria on  $h_L$  sweep for inductor  $Q$  at  $10 \text{ GHz}$





# Bibliography

- [1] Hobsbawm Eric J. E. *The Age of Extremes: The Short Twentieth Century, 1914–1991*. Ed. by Penguin Books. Michael Joseph Ltd, Oct. 1994. URL: <https://www.penguinrandomhouse.com/books/80963/the-age-of-extremes-by-eric-hobsbawm/>.
- [2] Moore Gordon E. “Cramming more components onto integrated circuits, Reprinted from Electronics, volume 38, number 8, April 19, 1965, pp.114 ff.” In: *IEEE Solid-State Circuits Society Newsletter* 11.3 (Sept. 2006). URL: <https://ieeexplore.ieee.org/document/4785860>.
- [3] Feynman Richard P. “Simulating Physics with Computers.” In: *International Journal of Theoretical Physics* 21 (June 1982), pp. 467–488. URL: <https://link.springer.com/article/10.1007%2FBF02650179>.
- [4] Deutsch David. “Quantum theory, the Church–Turing principle and the universal quantum computer.” In: *Proceedings of the Royal Society of London* 400 (July 1985), pp. 97–117. URL: <https://royalsocietypublishing.org/doi/10.1098/rspa.1985.0070>.
- [5] Shor Peter W. “Polynomial-Time Algorithms for Prime Factorization and Discrete Logarithms on a Quantum Computer.” In: *SIAM Journal on Computing* 26 (Oct. 1997), pp. 1484–1509. URL: <https://epubs.siam.org/doi/10.1137/S0097539795293172>.
- [6] DiVincenzo David P. “The Physical Implementation of Quantum Computation.” In: *Fortschritte der Physik* 48 (Sept. 2000), pp. 771–783. URL: <https://onlinelibrary.wiley.com/doi/abs/10.1002/1521-3978%28200009%2948%3A9%11%3C771%3A%3AAID-PROP771%3E3.0.CO%3B2-E>.
- [7] Jazaeri F. et al. “A Review on Quantum Computing: From Qubits to Front-end Electronics and Cryogenic MOSFET Physics.” In: *2019 MIXDES - 26th International Conference “Mixed Design of Integrated Circuits and Systems”*. Rzeszów, Poland: IEEE, 2019, pp. 15–25. URL: <https://ieeexplore.ieee.org/abstract/document/8787164>.
- [8] Langione M. et al. *Where Will Quantum Computers Create Value—and When?* Ed. by BCG. 2019. URL: <https://www.bcg.com/publications/2019/quantum-computers-create-value-when.aspx>.
- [9] Mermin N. David. *Quantum Computer Science: An Introduction*. Ed. by Cambridge University Press. Aug. 2007. URL: <https://www.cambridge.org/core/books/quantum-computer-science/66462590D10C8010017CF1D7C45708D7>.
- [10] Meunier T. et al. “Towards scalable quantum computing based on silicon spin.” In: *2019 Symposium on VLSI Technology*. Kyoto, Japan: IEEE, 2019, T30–T31. URL: <https://ieeexplore.ieee.org/document/8776562>.
- [11] Krantz P. et al. “A quantum engineer’s guide to superconducting qubits.” In: *Applied Physics Reviews* 6.2 (June 2019). URL: <https://aip.scitation.org/doi/10.1063/1.5089550>.

- 
- [12] Bruzewicz Colin D. et al. “Trapped-ion quantum computing: Progress and challenges.” In: *Applied Physics Reviews* 6.2 (May 2019). URL: <https://aip.scitation.org/doi/abs/10.1063/1.5088164?journalCode=are>.
- [13] Pieter Kok et al. “Linear optical quantum computing with photonic qubits.” In: *Reviews of Modern Physics* 79 (Jan. 2007), pp. 135–174. URL: <https://journals.aps.org/rmp/abstract/10.1103/RevModPhys.79.135>.
- [14] Loss Daniel and DiVincenzo David P. “Quantum computation with quantum dots.” In: *Physical Review A* 57.1 (Jan. 1998). URL: <https://journals.aps.org/pr/abstract/10.1103/PhysRevA.57.120>.
- [15] Pla Jarryd J. et al. “A single-atom electron spin qubit in silicon.” In: *Nature* 489 (Sept. 2012), pp. 541–545. URL: <https://www.nature.com/articles/nature11449>.
- [16] Maurand R. et al. “A CMOS silicon spin qubit.” In: *Nature Communications* 7.13575 (Nov. 2016). URL: <https://www.nature.com/articles/ncomms13575>.
- [17] Kobayashi T. et al. “Engineering long spin coherence times of spin–orbit qubits in silicon.” In: *Nature Materials* (July 2020). URL: <https://www.nature.com/articles/s41563-020-0743-3>.
- [18] Corna Andrea et al. “Electrically driven electron spin resonance mediated by spin–valley–orbit coupling in a silicon quantum dot.” In: *npj Quantum Information* 4.6 (Feb. 2018). URL: <https://www.nature.com/articles/s41534-018-0059-1>.
- [19] Zwanenburg Floris A. et al. “Silicon quantum electronics.” In: *Reviews of Modern Physics* 85 (July 2013), pp. 961–1019. URL: <https://journals.aps.org/rmp/abstract/10.1103/RevModPhys.85.961>.
- [20] He Y. et al. “A two-qubit gate between phosphorus donor electrons in silicon.” In: *Nature* 571 (July 2019), pp. 371–375. URL: <https://www.nature.com/articles/s41586-019-1381-2>.
- [21] Veldhorst M. et al. “Silicon CMOS architecture for a spin-based quantum computer.” In: *Nature Communications* 8.1766 (Dec. 2017). URL: <https://www.nature.com/articles/s41467-017-01905-6>.
- [22] Li R. et al. “A crossbar network for silicon quantum dot qubits.” In: *Science Advances* 7.8 (July 2018). URL: <https://advances.sciencemag.org/content/4/7/eaar3960>.
- [23] Vinet M. et al. “Towards scalable silicon quantum computing.” In: *2018 IEEE International Electron Devices Meeting (IEDM)*. San Francisco, CA, USA: IEEE, 2018, pp. 6.5.1–6.5.4. URL: <https://ieeexplore.ieee.org/document/8614675>.
- [24] Pozar David M. *Microwave Engineering*. Ed. by John Wiley & Sons. Nov. 2011. URL: <https://www.wiley.com/en-us/Microwave+Engineering%2C+4th+Edition-p-9780470631553>.
- [25] Simons Rainee N. *Coplanar Waveguide Circuits, Components, and Systems*. Ed. by John Wiley & Sons. Mar. 2004. URL: <https://www.wiley.com/en-fr/Coplanar+Waveguide+Circuits%2C+Components%2C+and+Systems-p-9780471463931>.
- [26] Heinrich W. “Quasi-TEM Description of MMIC Coplanar Lines Including Conductor-Loss Effects.” In: *IEEE Transactions on Microwave Theory and Techniques* 41.1 (Jan. 1993). URL: <https://ieeexplore.ieee.org/document/210228>.
- [27] Ghione G. and Naldi C. U. “Coplanar Waveguides for MMIC Applications: Effect of Upper Shielding, Conductor Backing, Finite-Extent Ground Planes, and Line-to-Line Coupling.” In: *IEEE Transactions on Microwave Theory and Techniques* 35 (Mar. 1987), pp. 260–267. URL: <https://ieeexplore.ieee.org/document/1133637>.

- [28] Heinrich W. "Conductor loss on transmission lines in monolithic microwave and millimeter-wave integrated circuits." In: *International Journal of Microwave and Millimeter-Wave Computer-Aided Engineering* 2 (Jan. 1992), pp. 155–167. URL: <https://onlinelibrary.wiley.com/doi/abs/10.1002/mmce.4570020304>.
- [29] Eisenstadt W. R. and Eo Y. "S-parameter-based IC interconnect transmission line characterization." In: *IEEE Transactions on Components Hybrids and Manufacturing Technology* 15 (Aug. 1992), pp. 483–490. URL: <https://ieeexplore.ieee.org/document/159877>.
- [30] Blampey B. et al. "Experimental characterization of dummies impact on interconnects propagation performance. Optimization of dummy sizes for the CMOS 22 nm technology node." In: *2008 12th IEEE Workshop on Signal Propagation on Interconnects*. Avignon, France: IEEE, 2008, pp. 1–4. URL: <https://ieeexplore.ieee.org/document/4558373>.
- [31] Hutin L. et al. "Si MOS technology for spin-based quantum computing." In: *48th European Solid-State Device Research Conference (ESSDERC 2018)*. Dresden, Germany: IEEE, 2018, pp. 12–17. URL: <https://ieeexplore.ieee.org/document/8486863>.
- [32] Fuchs G. D. et al. "Gigahertz Dynamics of a Strongly Driven Single Quantum Spin." In: *Science* 326 (Dec. 2009), pp. 1520–1522. URL: <https://science.sciencemag.org/content/326/5959/1520>.
- [33] Cohen-Tannoudji Claude, Dupont-Roc Jacques, and Grynberg Gilbert. *Photons and Atoms: Introduction to Quantum Electrodynamics*. Ed. by John Wiley & Sons. Mar. 1997. URL: <https://www.wiley.com/en-us/Photons+and+Atoms%3A+Introduction+to+Quantum+Electrodynamics-p-9780471184331>.
- [34] Feynman Richard P. *Quantum Electrodynamics*. Ed. by Perseus Publishing. Mar. 1998. URL: <https://www.hachettebookgroup.com/titles/richard-p-feynman/quantum-electrodynamics/9780813346380/>.
- [35] Bertrand Patrick. *Electron Paramagnetic Resonance Spectroscopy*. Ed. by Springer International Publishing. Feb. 2020. URL: <https://www.springer.com/gp/book/9783030396626>.
- [36] Cohen-Tannoudji Claude, Diu Bernard, and Laloë Franck. *Quantum Mechanics, Volume 2*. Ed. by John Wiley & Sons. June 1977. URL: <https://www.wiley.com/en-fr/Quantum+Mechanics%2C+Volume+2-p-9780471164357>.
- [37] Laucht Arne et al. "Electrically controlling single-spin qubits in a continuous microwave field." In: *Science Advances* 1.3 (Apr. 2015). URL: <https://advances.sciencemag.org/content/1/3/e1500022>.
- [38] Takeda K. et al. "Optimized electrical control of a Si/SiGe spin qubit in the presence of an induced frequency shift." In: *npj Quantum Information* 4.54 (Oct. 2018). URL: <https://www.nature.com/articles/s41534-018-0105-z>.
- [39] Pla Jarryd J. et al. "High-fidelity readout and control of a nuclear spin qubit in silicon." In: *Nature* 496 (Apr. 2013), pp. 334–338. URL: <https://www.nature.com/articles/nature12011>.
- [40] Hanson Ronald and Burkard Guido. "Universal Set of Quantum Gates for Double-Dot Spin Qubits with Fixed Interdot Coupling." In: *Physical Review Letters* 98.5 (Jan. 2007). URL: <https://journals.aps.org/prl/abstract/10.1103/PhysRevLett.98.050502>.
- [41] Ashcroft Neil W., Mermin N. David, and Wei Dan. *Solid State Physics: Revised Edition*. Ed. by CENGAGE Learning Asia. June 2016. URL: <https://www.cengageasia.com/TitleDetails/isbn/9789814369893>.
- [42] Koppens F. H. L. et al. "Driven coherent oscillations of a single electron spin in a quantum dot." In: *Nature* 4442 (Aug. 2006), pp. 766–771. URL: <https://www.nature.com/articles/nature05065>.

- [43] Dehollain J. P. et al. “Nanoscale broadband transmission lines for spin qubit control.” In: *Nanotechnology* 24.1 (Dec. 2012). URL: <https://iopscience.iop.org/article/10.1088/0957-4484/24/1/015202>.
- [44] Asaad S. et al. “Coherent electrical control of a single high-spin nucleus in silicon.” In: *Nature* 579 (Mar. 2020), pp. 205–209. URL: <https://www.nature.com/articles/s41586-020-2057-7>.
- [45] Pioro-Ladrière M. et al. “Electrically driven single-electron spin resonance in a slanting Zeeman field.” In: *Nature Physics* 4 (Aug. 2008), pp. 776–779. URL: <https://www.nature.com/articles/nphys1053>.
- [46] Hanson R. et al. “Spins in few-electron quantum dots.” In: *Reviews of Modern Physics* 79 (Oct. 2007), pp. 1217–1265. URL: <https://journals.aps.org/rmp/abstract/10.1103/RevModPhys.79.1217>.
- [47] Gonzalez-Zalba M. F. et al. “Probing the limits of gate-based charge sensing.” In: *Nature Communications* 6.6084 (Jan. 2015). URL: <https://www.nature.com/articles/ncomms7084>.
- [48] Zheng G. et al. “Rapid gate-based spin read-out in silicon using an on-chip resonator.” In: *Nature Nanotechnology* 14 (July 2019). URL: <https://www.nature.com/articles/s41565-019-0488-9>.
- [49] Crippa A. et al. “Level Spectrum and Charge Relaxation in a Silicon Double Quantum Dot Probed by Dual-Gate Reflectometry.” In: *Nano Letters* 17 (Jan. 2017). URL: <https://pubs.acs.org/doi/10.1021/acs.nanolett.6b04354>.
- [50] Hutin L. et al. “Gate reflectometry for probing charge and spin states in linear Si MOS split-gate arrays.” In: *2019 IEEE International Electron Devices Meeting (IEDM)*. San Francisco, CA, USA: IEEE, 2019, pp. 37.7.1–37.7.4. URL: <https://ieeexplore.ieee.org/document/8993580>.
- [51] Crippa A. et al. “Gate-reflectometry dispersive readout and coherent control of a spin qubit in silicon.” In: *Nature Communications* 10.2776 (July 2019). URL: <https://www.nature.com/articles/s41467-019-10848-z>.
- [52] Mansour Raafat R. “Microwave Superconductivity.” In: *IEEE Transactions on Microwave Theory and Techniques* 50 (Aug. 2002), pp. 750–759. URL: <https://ieeexplore.ieee.org/document/989959>.
- [53] Vadim Vasil’evich Schmidt. *The Physics of Superconductors: Introduction to Fundamentals and Applications*. Ed. by Springer Science & Business Media. 1997. URL: <https://www.springer.com/gp/book/9783540612438>.
- [54] Sheen D. M. et al. “Current distribution, resistance, and inductance for superconducting strip transmission lines.” In: *IEEE Transactions on Applied Superconductivity* 1 (June 1991), pp. 108–115. URL: <https://ieeexplore.ieee.org/document/84617>.
- [55] Antsos D. et al. “Modeling of Planar Quasi-Tem Superconducting Transmission Lines.” In: *IEEE Transactions on Microwave Theory and Techniques* 40 (June 1992), pp. 1128–1132. URL: <https://ieeexplore.ieee.org/document/141344>.
- [56] Rafique M. R. et al. “Optimization of superconducting microstrip interconnects for rapid single-flux-quantum circuits.” In: *Superconductor Science and Technology* 18.8 (June 2005). URL: <https://iopscience.iop.org/article/10.1088/0953-2048/18/8/007>.
- [57] Urdampilleta M. et al. “Gate-based high fidelity spin readout in a CMOS device.” In: *Nature Nanotechnology* 14 (May 2019), pp. 737–741. URL: <https://www.nature.com/articles/s41565-019-0443-9>.

BIBLIOGRAPHY

---

- [58] Mohan S. S. et al. "Simple Accurate Expressions for Planar Spiral Inductances." In: *IEEE Journal of Solid-State Circuits* 34 (Oct. 1999), pp. 1419–1424. URL: <https://ieeexplore.ieee.org/document/792620>.
- [59] Linden D. S., Orlando T. P., and Lyons W. G. "Modified two-fluid model for superconductor surface impedance calculation." In: *IEEE Transactions on Applied Superconductivity* 4 (Sept. 1994), pp. 136–142. URL: <https://ieeexplore.ieee.org/document/317828>.